EFFECTS OF EXCIMER LASER ON THE SURFACE MORPHOLOGY AND MICROSTRUCTURE OF IRON-BASED METALLIC GLASSES, AND EVALUATION OF ITS WEAR AND CORROSION CHARACTERISTICS

By

VAMSI KARTHIK KOMMINENI

Bachelor of Technology in Mechanical Engineering

Jawaharlal Nehru Technological University

Anantapur, Andhra Pradesh, India

2004-2008

Submitted to the Faculty of the
Graduate College of the
Oklahoma State University
in partial fulfillment of
the requirements for
the Degree of
MASTER OF SCIENCE
May, 2011

EFFECTS OF EXCIMER LASER ON THE SURFACE MORPHOLOGY AND MICROSTRUCTURE OF IRON-BASED METALLIC GLASSES, AND EVALUATION OF ITS WEAR AND CORROSION CHARACTERISTICS

Thesis Approved:

Dr. Sandip P. Harimkar

Thesis Adviser

Dr. Ranga Komanduri (Co-Adviser)

Dr. Satish T.S. Bukkapatnam

Dr. Mark E. Payton

Dean of the Graduate College

.

ACKNOWLEDGMENTS

I would like to extend my sincere gratitude and appreciation to many people who made this thesis possible. First of all, I am deeply indebted to Dr. Ranga Komanduri for giving the opportunity to work under his group. I would like to extend my deepest gratitude to my advisor Dr. Sandip Harimkar for his advice, guidance, inspiration, and support in completing this project. His optimism and enthusiasm provided me with endless source of knowledge and energy. Without his support this work would be impossible. I would like to acknowledge my thesis committee member Dr. Satish Bukkapatnam for his moral support in these 2 years to build confidence and mould me according to research interests. I appreciate his patience and concern in guiding me all these years.

I am always grateful to my dearest buddy Ashish anna who has been my strength throughout my Master's degree. I would like to thank him for his affectionate help in XRD analysis and guiding me like brother during my all difficult times. I would like to thank Karthik, Praneeth anna, Sudheer anna, Vineet, Deshpande, Chakri, Pilla, Sudharshan, Sai Kiran anna, Tushar for being as good friends and well-wishers. I extend my thanks to Mrinalini for her support and enthusiasm. I thank Sagar, Nandu, Balayya, Pavan, Venki, Jyothi anna, Sirish anna, Puli anna, Gandhi, Satish, Hari, Arun, Krishnapriya, Maddy, Anusha, Jayakrishna for being my energy throughout my journey. I also thank several of my friends who have helped me throughout my life.

I would like to express my deepest gratitude to my parents and grandparents for their love, encouragement, and confidence on me. They have always been a source of inspiration for me. I should thank my grandma for love from bottom of her heart, I miss you a lot.

Finally, I would like to thank the Department of Mechanical and Aerospace Engineering for providing me with the opportunity to pursue M.S. at Oklahoma State University.

TABLE OF CONTENTS

Chapter **Page**

Chapter **Page**

LIST OF TABLES

LIST OF FIGURES

CHAPTER 1

INTRODUCTION

1.1 Metallic Glasses:

Metallic glasses or amorphous alloys are a relatively young class of materials, which exhibit superior properties, such as hardness, elastic modulus, and corrosion/wear resistance. These alloys were first reported in 1960 by Duwez and his colleagues at the California Institute of Technology [1]. They performed rapid-quenching tests on an $Au_{75}Si_{25}$ alloy composition by chilling metallic liquids at very high cooling rates on the order of ~10^5-10^6 K/s [1]. Their experiments led to an important conclusion that the process of crystal nucleation and growth could be kinetically bypassed in some alloy melts by freezing it to a vitreous solid without crystallization. A great number of amorphous alloys have been produced in the last three decades by exploring different elemental compositions with very low critical cooling rates in order to retain the amorphous structure [2].

1.2 Different types of Metallic Glasses:

Different multi-component alloy systems, such as Zr-, Mg-, and La- based metallic glasses were synthesized in the 1990's by stabilization of super cooled liquid [2-5]. Iron-based amorphous alloys of composition Fe-Al-Ga-P-C-B was successfully developed in 1995 by Inoue and his colleagues [6-7]. In order to stabilize the super-cooled metallic liquid in metal-metal alloy systems and to promote the glass forming ability, three empirical component rules were proposed [8], namely:

- There should be three or more elements in the multi-component systems
- Atomic sizes of the main constituent elements should differ by significant percentage (> ~12%)
- The elements should have strong affinity towards each other [8].

Alloys satisfying these conditions can have highly dense, randomly packed liquid structures with high interfacial energy and low diffusivity which leads to the suppression of nucleation and growth. A variety of Fe-based, Co-based, Ni-based and Cu-based metallic glasses have been synthesized in accordance with these rules. Amorphous alloy systems can be classified into two groups: metal-metalloid and metal-metal systems [9]. The metal-metalloid group systems are primarily composed of Fe-, Co-, Ni-, Pd-, and Pt-based alloys, and metal-metal group systems are primarily Ni- and Cu- based alloys.

1.3 Properties of Metallic Glasses:

Metallic glasses with an amorphous structure exhibit unique properties that are not common for polycrystalline materials. These alloys do not contain any crystalline defects, such as grain boundaries, dislocations, and stacking faults. They are homogenous both structurally and chemically.

1.3.1 Mechanical and Tribological Properties:

Mechanical properties, such as strength and ductility are determined by the microstructure and dislocation motion in the crystalline materials. In contrast, for amorphous materials, mechanical properties depend on atomic and electronic structure due to its disordered atomic arrangement. Structural homogeneity (absence of grains and grain boundaries) does not permit the crystal deformation mechanism by dislocation slip. The plastic flow is restricted only to the regions within the shear bands. These materials experience little yielding prior to failure; exhibiting brittle behavior. From Fig. 1.1, it can be observed that glassy alloys exhibit a combination of higher strength and elastic limit.

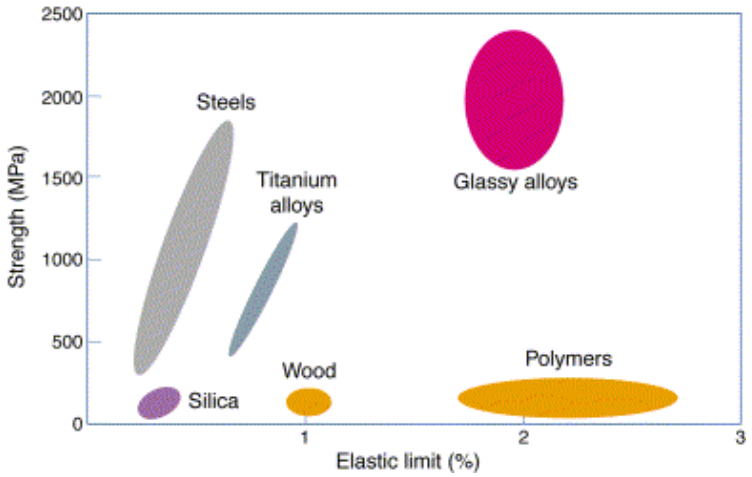

Fig. 1.1 Metallic glasses combine higher strength than crystalline materials with the elasticity comparable to polymers [10].

Metallic glasses exhibit very high fracture strength which exceeds the strength exhibited by the crystalline metal alloys due to its amorphous structure. Due to the random atomic arrangement, atoms are gridlocked into the glassy structure, making their movement very difficult, and consequently making amorphous metals very hard [11]. Table 1.1 gives an overview of the mechanical properties of some metallic glasses in comparison with crystalline materials.

Table 1.1: Mechanical properties of metallic glasses in comparison with crystalline materials [10].

Properties	**Amorphous alloys**	**Al alloys**	**Ti alloys**	**Steel alloys**
Density (g/cm^{-3})	6.1	2.6-2.9	4.3-5.1	7.8
Tensile Yield Strength (GPa)	1.9	0.10-0.63	0.18-1.32	0.50-1.60
Elastic Strain Limit (%)	2%	-0.5%	-0.5%	-0.5%
Fracture Toughness ($MPa\ m^{1/2}$)	2-14	23-45	55-115	50-154
Specific Strength ($GPa\ g^{-1}cm^{-3}$)	0.32	< 0.24	< 0.31	< 0.21

Another unique property of metallic glasses is higher elastic limit i.e., the ability to retain its original shape after undergoing elastic deformation at very high loads. The ability of amorphous alloys to store a high amount of elastic energy has made it a potential material in sporting applications. This desirable combination of high hardness and elasticity properties have led to its potential applications in the leads of golf clubs [10, 11].

Amorphous alloys have excellent wear and abrasion resistance. Amorphous alloys exhibit two distinct deformation mechanisms during wear which is quite different to the crystalline alloys due to long range atomic order in the crystalline counterparts [12]. The first one, plastic deformation occurs through homogeneous (viscous) flow at high temperatures and low stresses. The other one is that, at lower temperatures and higher stresses, deformation is quite inhomogeneous and concentrated in the localized shear bands. Plasticity (which is controlled by free volume) at contact plays an important role in wear behavior of alloys because of the extensive material flow taking place under the sliding conditions. Plasticity (change in free

volume) primarily depends on the structural relaxation and crystallization. Free volume reduction results in severe embrittlement due to reduced propensity towards the shear band formation and propagation which are the carriers of plasticity in amorphous metals. Thus, the structural relaxation results in reduction of material's ability to accommodate plastic deformation (i.e., shear banding propensity). There will be a transition in the flow behavior from homogeneous to heterogeneous mode depending on the crystallinity, which primarily determines the wear behavior. There were conflicting arguments in the literature on the role of amorphous structure on the wear performance [13].

Amorphous alloys have lower fracture toughness than the crystalline alloys because of the unavailability of microstructural mechanism to arrest the propagation of shear bands before generating cracks. However, fracture toughness can be improved by reinforcing amorphous alloys with crystalline particles [14].

1.3.2 Corrosive Properties:

The absence of defects (grain boundaries, and dislocations) and their chemical homogeneity results in higher corrosion resistance in these alloys. Particularly higher corrosion resistance is because of the formation of passivation layer which protects the underlying alloy. Formation of the passive layer depends on the chemical homogeneity and the atomic composition. Addition of elements such as Cr, Mo, and P enhances the corrosion resistance. Addition of alloying elements not only increases the corrosion resistance but also increases the glass forming ability of a material. Change in chemical composition and environment plays an important role in corrosive behavior [15].

1.4 Applications of Metallic Glasses:

Amorphous alloys have applications in various fields owing to its unique and unconventional characteristics. It has a particular advantage in sporting goods because of its important properties, such as, higher strength to weight ratio, and lower elastic modulus. They are used to make heads of golf clubs and tennis racket frames. More energy is transferred to the ball during impact by absorbing lesser energy in the golf heads made of amorphous alloys [16].

These are used to produce advanced sensors with higher sensitivity and better high-pressure properties. These alloys are used in production of micro-gears for various engineering applications. These alloys may find potential applications in aircraft and automotive industries due to their greater durability, performance, reduced maintenance and high wear and corrosion resistance.

Amorphous alloys find potential applications in the medical field because of their biocompatibility, higher strength to weight ratio (compared with titanium and stainless steel), and excellent wear resistance [16].

Fe-based metallic glasses find applications as soft magnetic material for common mode choke coils. These alloys find potential applications in electronic appliances market such as, in MP3s, cell phones, thumb drive cases, digital cameras etc., as these can be produced in thin sections while retaining the mechanical strength [16]. These metallic glasses are promising as new metallic engineering materials.

1.5 Basics of Lasers and its Applications in Micromachining:

Before going into detail of the laser micromachining process, it is necessary to understand the fundamentals of the laser system. In this section, a brief review on the history, types of lasers, and properties of laser is presented.

1.5.1 Introduction to Lasers:

The word LASER is an acronym for Light Amplification by Stimulated Emission of Radiation. It is essentially a coherent, convergent, and monochromatic beam of electromagnetic radiation with wavelength ranging from ultraviolet to infrared. All lasers share a crucial element called gain medium, which is capable of amplifying radiation. Fig. 1.2 illustrates on the history of lasers.

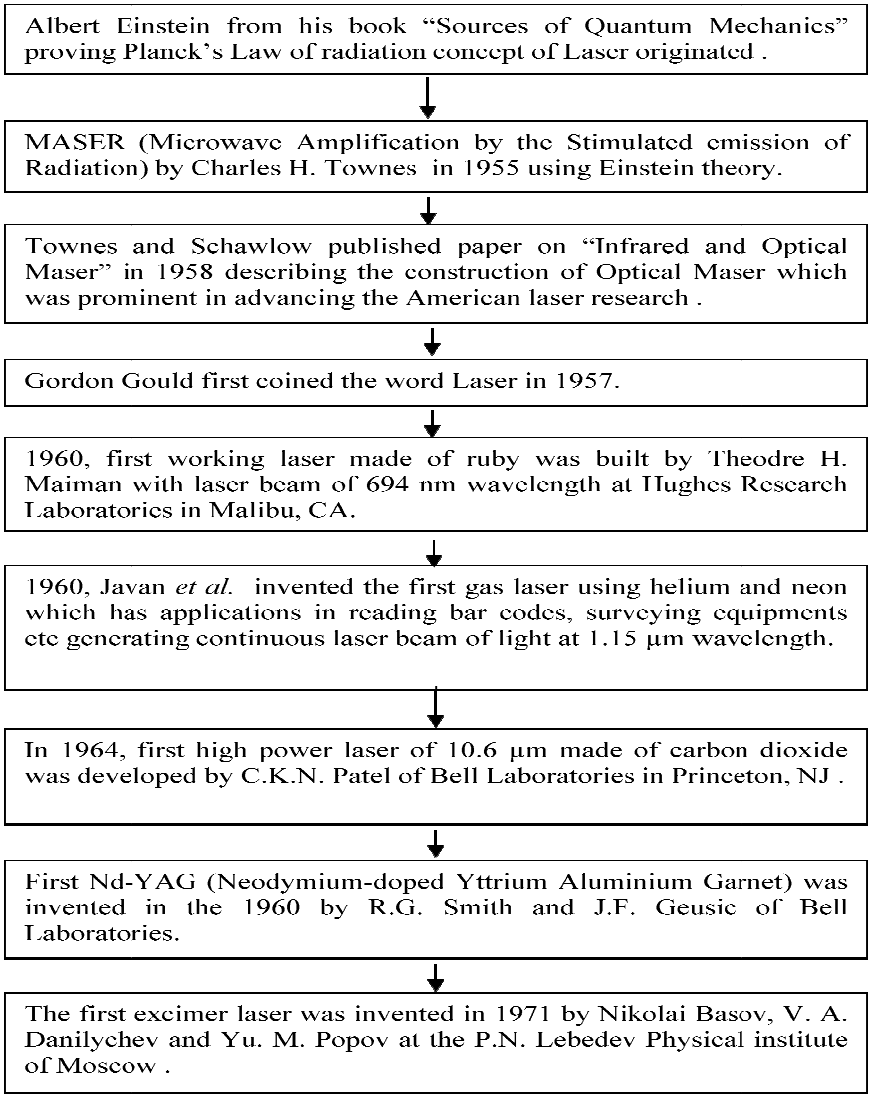

Fig. 1.2 Flow chart giving brief history of Laser [17-21].

1.5.1.1 Working Principle of Laser:

An energy transfer phenomenon in atoms or molecules involves spontaneous emission, stimulated emission/absorption, and nonradioactive decay. According to quantum mechanics, electrons of atoms take different energy states, say E_1, E_2, E_3…etc., where $E_1<E_2<E_3<\ldots$. As the lower energy level is more stable than the higher energy level, electrons at higher energy level tend to decay into lower energy levels [22]. This energy difference between the two levels can be given out as electromagnetic radiation [22]. This process is called spontaneous radiation.

The energy difference between two levels is given by [22]

$$E_2-E_1= h\upsilon_o \quad \text{——————} (1)$$

where E_2 is the higher energy level, E_1 is the lower energy level, h is Planck's constant and υ_o is the frequency of the electromagnetic wave.

Generally, electromagnetic (EM) radiation is described by Wave Theory or Quantum Theory. The strength of laser beam is given by the intensity of radiation according to wave theory. In Quantum Theory, radiation is considered as a stream of particles called Photons. The photon energy is given by $E = h\upsilon_o$. When external EM waves of frequency υ_o near the transition frequency between E_2 and E_1 are incident on electrons in material, it forces the electrons to undergo transition from E_2 to E_1 which gives rise to an external EM wave (a photon), while incident photon still exists [22]. This transition process caused by the external excitation is called stimulated radiation. In spontaneous emission, the radiation is in all directions and in random phases. In stimulated radiation, the emitted waves of any atoms are in the same direction and in the same phase with the incident wave [22].

Usually lower energy level has more number of electrons than higher energy level. EM wave cannot be amplified because of the domination of stimulated absorption over stimulated

radiation. Amplification of incident wave is possible only when the number of upper level electrons is greater than that of lower level electrons. This case is called population inversion. In order to get more electrons into upper level we need to raise electrons from lower energy level to higher energy level [22]. This process is called pumping. Population inversion is achieved by pumping process in which excitation of electrons to higher energy states is achieved. By population inversion emission of laser radiation is achieved. Different methods of pumping are Optical Pumping (used in ruby, Nd:YAG, and diode lasers) and Electrical Pumping (used in gas lasers). There is minimum population inversion like threshold condition required for lasing action [22].

1.5.2 Properties of Laser Beam:

Laser beam is characterized by various combinations of interesting properties. The important properties are beam coherence, monochromatism, collimation, brightness or radiance, focal spot size, temporal Mode, normal pulsing, Q-switching, modelocking, frequency multiplication, output power, and duration of emission [23].

1.5.3 Types of Lasers:

Lasers are divided into different types on the basis of physical nature of the active laser medium. The laser medium can be a solid, gas, liquid, and semiconductor. All the different types of laser are commonly designated by the type of lasing material employed. They are solid state laser, semiconductor lasers, gas lasers, chemical lasers, liquid lasers, free electron lasers, and other laser types [23].

1.5.3.1 Liquid Lasers:

These lasers typically use large organic dye molecules as lasing media. Due to the physical nature (low density, and homogeneity, etc.) of the liquid media, the liquid dye lasers are

relatively easy to fabricate. Because of the above properties it has advantages like ease of cooling and replenishment in the laser cavity. These lasers are designed such that the frequency at which they emit a beam can be varied and is tunable. These lasers are not typically used for laser machining [23].

1.5.3.2 Solid State Lasers:

Solid state lasers use ions suspended in a crystalline matrix to produce laser light. The ions or dopants provide the electrons for excitation while the crystalline matrix propagates the energy between ions [23]. Large number of lasers, such as Nd:YAG, Nd: Glass, Alexandrite, and Ti:Sapphire in this class are available in these days. The major type of solid state laser used in laser machining is Nd:YAG which stands for a Neodymium-Yttrium Aluminum Garnet laser. Nd:YAG laser consists of crystalline YAG with a chemical formula $Y_3Al_5O_{12}$ as a host material. These lasers are typically used for cutting and drilling applications. They operate at different wavelengths ranging from 266 nm to 1064 nm [23]. Nd:YAG laser is also available in frequency-doubled mode in which the output of the laser is in the green portion of the visible spectrum at 532 nm. In addition to frequency doubled operation, the laser is also available in frequency-tripled (355 nm) and frequency-quadrupled (266 nm) modes [23]. The output of the laser can be continuous, pulsed or Q-switched. External light source is needed for pumping. Light source for pumping depends on the absorption characteristics of the crystal. Light from the external source flash lamp enters the laser rod and excites the light emitting atoms. The beam is propagated by the reflection of photons generated by stimulated emission travelling normal to mirrors [23].

1.5.3.3 Gas Lasers:

These lasers use gaseous lasing medium. In this type of lasers, electrical current is discharged through a gas to produce light energy. The gaseous lasing materials have many advantages over solid material [23], such as

1. Gases acts as a homogeneous laser medium,

2. Gases can be easily transported for cooling and replenishment, and

3. Gases are relatively inexpensive.

Even though gas has lower density than all the other media these require a large volume of gas to achieve significant population inversion for laser action [23]. Hence, usually gas lasers are relatively larger in setup volume than the solid-state lasers. These can be subdivided on the basis of the compilation of the gas like neutral atom, ion, or molecular depending on whether the laser transitions are taking place between the energy levels of atoms, ions and molecules. Molecular gas lasers such as CO_2 laser are more widely used for machining. Neutral atom and ion lasers, such as helium neon laser, ion laser (Argon or Krypton) are important for many scientific applications but not for laser machining.

In molecular gas lasers, excitation of molecules in lasing medium takes place. The lasing medium of a CO_2 laser is made up of a number of different gases, namely, nitrogen, helium, and carbon dioxide. CO_2 lasers operate in the infrared region. The most basic form of a CO_2 laser consists of gas discharge with a total reflector at one end and an output coupler (usually a semi-reflective coated zinc selenide mirror) at the output end [23]. Energy input for the excitation of lasing medium is acquired by the collision of CO_2 molecules rather than the external input [24]. CO_2 lasers have a theoretical maximum energy output of 15 mW at 10% energy efficiency depending on the lasing medium (sealed discharge, axial, traverse or cross flow). Traverse flow lasers are the best lasers among all the other lasers exhibiting high power output.

1.5.3.4 Excimer Lasers:

Excimer Lasers are notable for their ability to produce high power laser radiation in the ultraviolet portion of the spectrum. Operation in ultraviolet region means that the diffraction limited focal spot can be very small, even smaller than with high power lasers. In addition,

shorter wavelength generally means that there will be good coupling of energy with the workpiece [24].

The term *excimer* is derived from the word dimer, which means a diatomic molecule formed by the union of two atoms. If the molecule is in the excited state, it is referred to as an excited dimer or excimer [24]. In these type of lasers, light is emitted by short lived molecule made up of one rare gas atom (e.g., argon, krypton, or xenon) and one halogen atom (e.g., fluorine, chlorine, bromine). The excimer laser utilizes the molecules containing the noble gases, which do not form chemical compounds under normal circumstances. However, the noble gases may form compounds that have no stable ground state but may have excited states which are temporary. The important gas molecules are rare gas halides including argon fluoride (ArF), krypton fluoride (KrF) and xenon chloride (XeCl) [24].

These diatomic molecules have very short lifetimes and dissociate releasing the excitation energy through UV photons. Very few dimer molecules remain in ground state, as ground state is unstable. So, direct excitation from ground state is not possible. However, various indirect excitations by the electrical discharge result in laser radiation. Although excimer lasers are of the gas type, special attention is given to them because they can also be considered as chemical lasers, as it is composed of a mixture of rare gas and a halogen in a cavity into which energy is deposited by an electron beam or an electrical discharge to cause an electrically excited molecule which can exist only in the excited state [24]. In the present investigation, an excimer laser with krypton fluoride (KrF) is used. This gas under lasing conditions emits photons (either spontaneously or by stimulated emission) to produce a laser beam at 248 nm in the ultraviolet region of the spectrum. In this gas mixture of krypton and fluorine, excitation takes place by pulsed electrical discharge producing metastable excited state (KrF)* [24]. The excited state is bound for a short time and dissociates according to the equation

$$(KrF)^* \text{ ----------> } Kr + F + \text{Photon (248 nm)} \quad (2)$$

The emission of photon causes the KrF* molecule to fall to its lowest energy state, in which two atoms repel each other, so that molecule breaks up. These lasers have pulse durations in the nanosecond range. As the ground state is inherently unstable, population in the ground state is low, giving easier population inversion. Average power is available in the range of 50 W and pulse energy up to 2 J per pulse. Common available excimer lasers and their respective wavelength are noted below in Table 1.2.

Table 1.2: Types of Excimer Laser and their corresponding wavelength [24].

Type	**Wavelength (nm)**
F_2*	157
ArF	193
KrCl	222
KrF	248
XeCl	308
XeF	350

*Not a rare –gas halide, but usually grouped with excimer.

1.5.4 Laser Micromachining:

Currently, manufacturers are looking for a process to produce small or micro circular holes in a single workpiece at very shallow angles to the surface. All these modern requirements and the limitations of the conventional machining processes resulted in search for non-traditional processes for machining applications. Several nontraditional processes used in machining are Electrical Discharge Machining (EDM), Electrochemical Machining (ECM), Laser-Beam

Machining (LBM), Electron-Beam Machining (EBM), Photochemical Machining (PCM), Abrasive Water Jet Machining (AWJ), and Ultrasonic Machining (USM) [25].

Laser machining is a material removal process which can be achieved by interactions between the laser and the target material. Industrial lasers used for material removal purposes are Nd:YAG (Neodymium:Yttrium Aluminum Garnet), ruby, excimer laser, and carbon dioxide (CO_2) laser. Excitation of atoms in laser cavity results in energy which is released at a characteristic constant frequency. The monochromatic light produced is amplified during successive reflections from the mirrors [26]. The thoroughly collimated light exits through the partially reflecting mirrors to the lens which focuses it just below the surface of the workpiece. The workpiece surface reflectivity, absorption coefficient, thermal conductivity, specific heat, thermal diffusivity, heat of fusion, and heat of vaporization are the important parameters in laser machining. Sharp, short, Gaussian-mode repetitive pulses are best for cutting because they have high energy densities. Laser beam machining is not a bulk material removal process [26].

In general, laser machining can be divided into one-, two-, and three-dimensional process. Fig. 1.3 shows the schematic of the one, two and three dimensional laser machining [26]. In case of a one dimensional process (drilling), the laser beam is stationary relative to the workpiece. The erosion front, located at the bottom of the drilled hole, propagates in the direction of the line source in order to remove the material. In the case of two-dimensional process (cutting), the laser beam is in relative motion with respect to the workpiece. Material removal occurs by moving the line source in a direction perpendicular to the line direction and forms a two-dimensional surface. The erosion front is located at the leading edge of the line source. For three-dimensional machining, two or more laser beams are used and each beam forms a surface through relative motion with a workpiece. The erosion front for each surface is found at the leading edge of each laser beam. When the surfaces intersect, the three-dimensional volume bounded by the surfaces is removed [26].

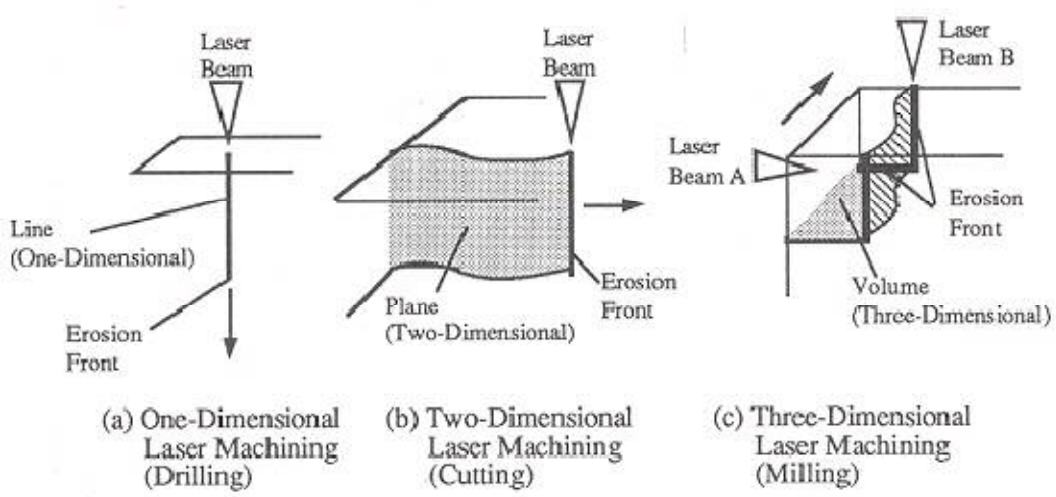

Fig. 1.3 Schematic of one-, two-, and three-dimensional laser machining [26].

The effectiveness of laser machining depends upon thermal and optical properties rather than mechanical properties of the material to be machined. Therefore, materials which exhibit a high degree of brittleness or hardness and have good thermal properties, namely, thermal diffusivity and conductivity are well suited for laser machining [26].

Excimer lasers are long pulse lasers with pulse durations in the range of few nanoseconds. Fig. 1.4 is an illustration on the effects on the workmaterial when machining with long pulses (millisecond to nanosecond) and ultra short pulses (picoseconds to femtosecond). When machining with long pulses effects observed on the workpiece are microcracks, removal of material over dimensions larger than work spot, contamination of surrounding area due to melting and sputter evaporation was observed. Other adverse effects are damage to adjacent structures, delamination, formation of recast material, and poor shot-to-shot reproducibility. Basically laser pulse duration is longer than the heat diffusion time which primarily affects the efficiency and accuracy of micromachining process [27].

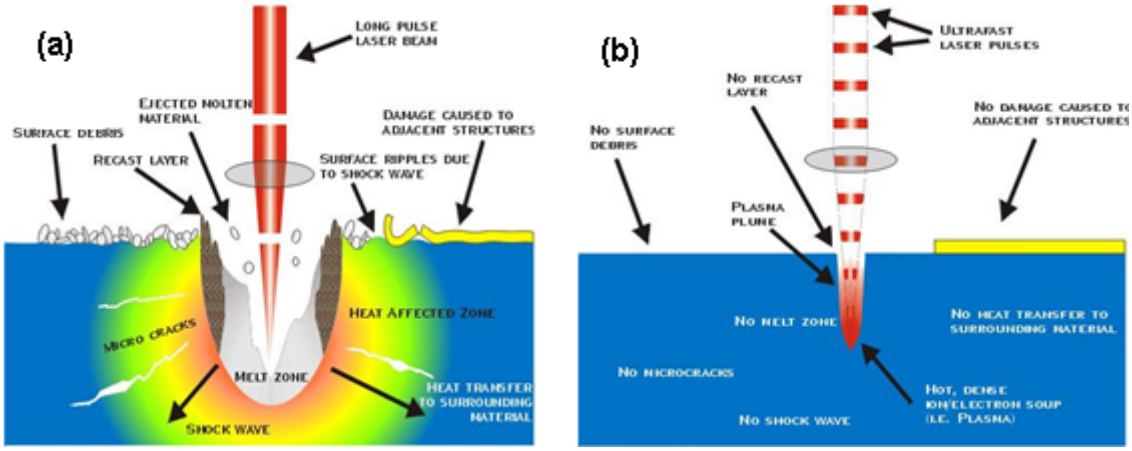

Fig. 1.4 (a) Machining with longer pulses, and (b) machining with shorter pulses [27].

Heat affected zones (HAZ) are formed in larger area around the machined spot due to heat diffusion. Apart from all the disadvantages mentioned above, long pulse lasers are associated with higher removal rates. Ultra short pulse machining is associated with lesser defects compared with long pulse as shown in Fig. 1.4 (b), but it has very low removal rates. This is mainly due to shorter interaction time by pulses in ultrashort range.

1.5.5 Advantages of Laser beam machining:

Advantages of the laser beam machining [23-28] are:

- It is a non-contact process.
- It is a flexible process.
- High production volumes associated with fully automated or semi-automated tooling applications.
- Ease of automation for complex hole patterns.
- Absence of tool wear and breakage as no tool is used.
- Large number of holes per work piece or assembly.

- Burr less machining.
- Capability to machine very small holes with very large depth to diameter ratios.
- Operability in various environments including air, inert gas, vacuum, and certain liquids.
- Ability to machine wide range of materials, such as ceramics, composites, metals, and polymers.
- Clean cuts can be obtained.
- Eliminates the replacement costs associated with tool wear and breakage.

Limitations:

- Possible defects, such as heat affected zones (HAZ), taper, recast layer, cracking, striations, and geometrical irregularities.

1.5.6 Laser-Material Interactions:

In order to investigate the machining process using a laser, it is useful to understand the physical processes that occur during the interaction of laser radiation with materials. Laser parameters that influence the interaction process are intensity, wavelength, spatial and temporal coherence, angle of incidence, polarization, irradiation time etc., and the material parameters are absorptivity, thermal conductivity, specific heat, density, latent heats etc. When a laser beam interacts with the workpiece, several effects which influence are reflection, refraction, absorption, scattering and transmission of light [28]. The amount of light reflected depends on the wavelength of the laser radiation, angle of incidence of laser beam, conductivity of the material, surface conditions of the materials, such as surface roughness, the amount to which it is oxidized, and its temperature. Longer the wavelength of laser radiation, material exhibits higher reflectivity. Rough surfaces absorb more light than finished surfaces; as the laser beam interacts with the surface it undergoes two or more reflections off the local peaks and valleys. Increase in the absorption of laser beam by the material surface results in increase of material removal.

Absorption of radiation in a material is given by Beer-Lambert Law [28]:

$$I(z) = I_o e^{-uz} \quad \text{——————————} \quad (3)$$

Where I_o and I(z) are the intensities before and after transmission through the material of thickness z and absorption coefficient u.

The incident beam energy has a spatial intensity distribution which is usually a Gaussian distribution produced by a laser operating in the TEM_{00} (lowest order or fundamental transverse electromagnetic mode of the laser resonator) mode. The focused beam radius is usually specified as the distance between the beam center and a point where the intensity is reduced from its maximum value at the beam center by a factor of e^{-2} (e = 2.7182); the average diameter of the drilled hole may be less than the beam diameter due to various heat loss effects. As shown in Fig. 1.5, d is the diameter of the laser beam. These heat losses are primarily due to conduction into the interior of the workpiece and losses to the environment which divert the beam energy away from the actual hole drilling process [28].

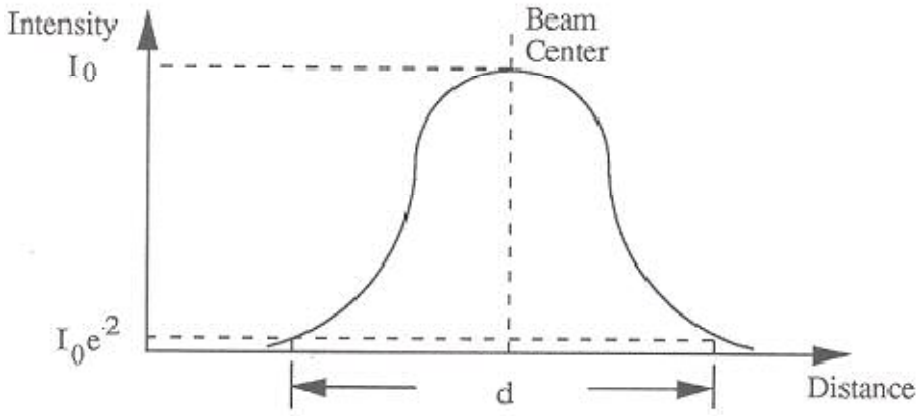

Fig. 1.5 Spatial intensity distribution for TEM_{00} laser beam [28].

Laser beam absorbed by the material is converted into heat. Depending on the temperature rise, various physical effects, such as heating, melting and vaporization of the material occur. Ionization of vapor during laser irradiation causes plasma generation [28]. Once the plasma is generated, it doesn't allow the laser beam to reach the workpiece which is called plasma shielding [28]. The absorption of laser energy not only shields the workpiece from the laser beam, but also produces mechanical effects such as shock waves [28]. In addition to the above thermal and mechanical effects, photochemical processes, such as photo ablation occur. If the incident laser intensity is sufficiently high, absorption of laser can result in phase, thermal, mechanical changes which propagate into material. Melting and evaporation are efficient parameters in the machining process.

Material removal mechanism in excimer lasers is different from the CO_2, and Nd-YAG lasers. In CO_2, and Nd-YAG lasers, material removal takes place by heating it from solid to liquid or to gaseous state [28]. Excimer lasers remove material from the workpiece either by photo thermal (vaporization) or photochemical process or by combination of both. In excimer laser, material removal takes place through ablation by directly breaking the chemical bonds of the material until it dissociates into chemical components instead of melting or vaporization [28]. The most important parameters which influence the ablation mechanism are laser wavelength, energy on the target, pulse length, repetition rates, and the target material properties.

CHAPTER 2

REVIEW OF LITERATURE

2.1 Micromachining Response of Metallic Glasses:

In the recent years, amorphous alloys gained attraction due to their unique properties in various industrial applications. Investigating the micromachining response of the metallic glasses to different kinds of traditional and nontraditional methods would be of significant interest if amorphous alloys are to be used for the production of components incorporating micro- and nano-features for applications in MEMS, micro-sensor systems, minimum size die and tool components [29, 30]. In the literature, micromachining response of amorphous alloys to conventional methods, microsecond-, picosecond-, femtosecond-lasers, and other micromachining techniques, such as Focused Ion Beam (FIB) milling have been studied.

2.1.1 Traditional Mechanical Machining Methods-Review:

Bakkal *et al*. [31-36] investigated on the cutting mechanics in machining of zirconium based bulk metallic glasses having composition, $Zr_{52.5}Ti_5Cu1_{7:9}Ni_{14:6}Al_{10}$, and observed that the material is subjected to severe deformation during machining operation. When machining bulk metallic glass on a CNC lathe ductile chips were reported to be formed above the threshold cutting speed.

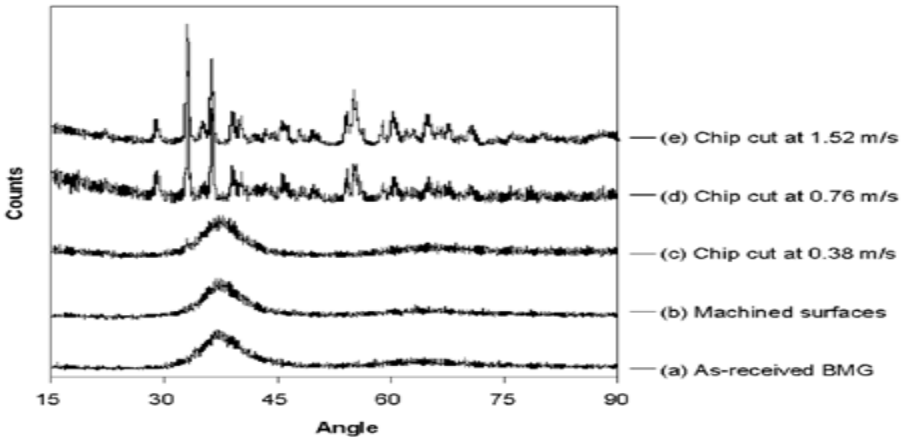

Fig. 2.1 Relative x-ray intensity vs. diffraction angle for the cases indicated [31].

Crystallization within the chips was also observed which is shown in Fig. 2.1. Finally, viscous flow and occurrence of crystallization during the machining of bulk metallic glass was observed with high strain rates.

Significant reduction of cutting forces at higher cutting speed was observed due to thermal softening. Investigations on the effect of cutting speed, tool rake angle, tool coating, and tool thermal conductivity on the Zirconium based BMG ($Zr_{52:5}Ti_5Cu1_{7:9}Ni_{14:6}Al_{10}$) were conducted [33, 34]. Tool wear was observed because of welding of tool chip and chipping of tool edges. Studies on chip formation morphology and effects of spindle speed, feed rate, and tool-material on the light emission, chip, and burr formation in drilling BMG were conducted [34]. Formation of burrs during the machining was observed [34]. It was observed that WC-Co tool-material, due to its high thermal conductivity and hardness performs better in machining BMG than the high speed steel tool [34]. Fig. 2.2 shows the microstructure of chips cross-section at amorphous and crystalline regions. Since, the traditional machining methods are associated with undesirable features such as, burrs, tool wear, spatter and crystallisation of chips, efforts are focused on conducting the micromachining by using the non-traditional methods like lasers etc.,.

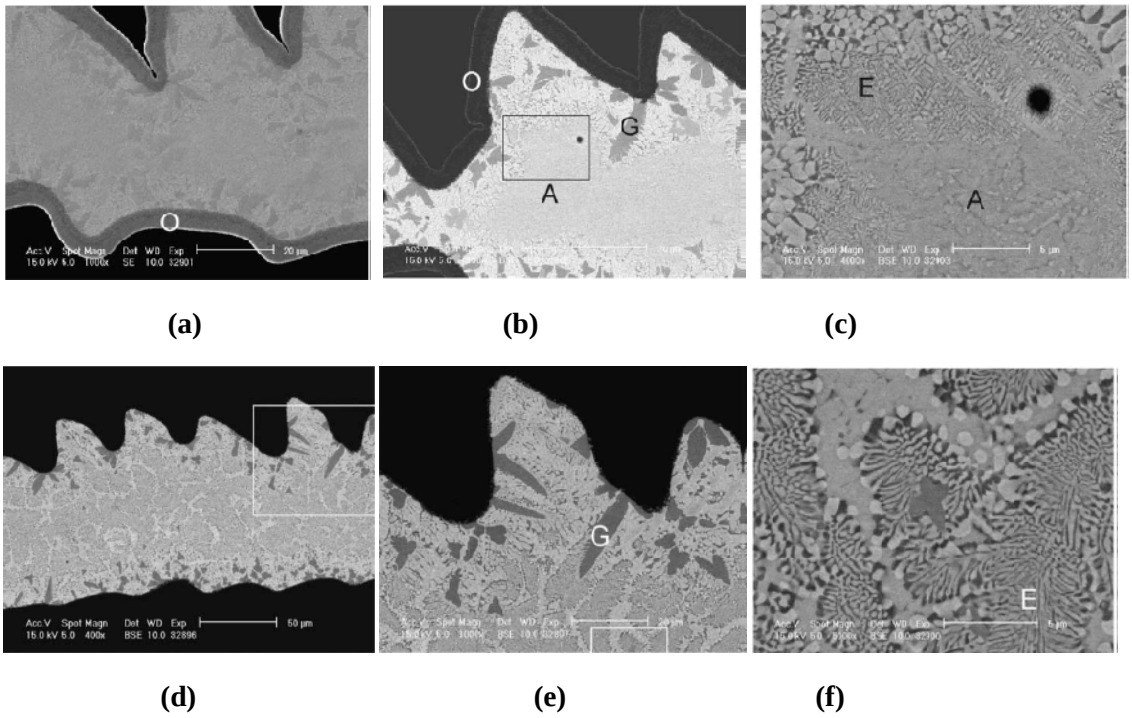

Fig. 2.2 SEM micrographs of the chips cross-section with both eutectic and amorphous regions, (a) oxide layer surrounding the chips (O), (b) shows the inside crystalline and amorphous regions, (G) represents the gray leaf-shape crystalline region, (c) close-up view of the box in (b) with the amorphous (A) to eutectic (E) crystalline transition, (d) SEM micrographs of the fully crystalline chip cross-section, (e) crystallized chips close-up view of the box in (d), and (f) close-up view of the eutectic crystalline region [box in (e)] [34].

2.1.2 Non-Traditional Machining Methods-Review:

In this section review of the machining of metallic glasses with non-traditional methods like microsecond, nanosecond, and femtosecond lasers is presented. In the group of nanosecond lasers, excimer lasers are high power lasers which emit short pulse (few nanoseconds) radiation in the ultraviolet range of the electromagnetic radiation. These are mainly used in micromachining applications where high removal rates are required. These types of lasers are usually used for the material removal in organic materials and polymers by non-thermal photochemical ablation

through high photon energies and single photon or multi photon interactions. In micromachining amorphous alloys with excimer laser material removal takes place by photothermal ablation in which absorbed energy gets converted into thermal energy in the material. The subsequent temperature facilitates material removal by rapid melting, vaporization and plasma formation.

Buetje *et al.* studied on excimer machining of amorphous metals [37]. It was observed that, as amorphous metals have excellent mechanical properties and thermal sensitivity, conventional mechanical and thermal tools (infrared emitted lasers) leads to difficulties with tool wear and recrystallization in the heat affected area which destroys the work piece quality [37]. It was identified that if pulses of extremely shortest durations (in the range of nanoseconds) with higher intensities are used in removal process, thermal input could be minimized inspite of its thermal interactions with metals [37]. Thus, recrystallisation processes inside the work piece can be minimized. It was observed that amorphous metals can be machined thermally by excimer laser without having thermal damage to work piece and is best suited for straight-line cuts, drilling or bended line cuts with mass production.

Sorescu *et al.* investigated on the machining response of $Fe_{81}B_{13.5}Si_{3.5}C_2$ metallic glass with pulsed excimer laser radiation of wavelength 308 nm [38]. It was observed that the effects of pulsed excimer laser irradiation on the magnetic anisotropy of iron-rich metallic glasses depend on the values of the irradiation parameters, such as pulse energy, pulse repetition rate, and material properties like magnetostriction constants [38]. Laser induced phase transformation with onset of partial crystallization and surface oxidation was observed. Relationship between magnetic parameters and structural characteristics of alloy phases are used to address the phase evolution and microstructure development during various laser irradiations treatments [38, 39, and 40]. Main focus was on the magnetic and structural characteristics of the metallic glasses irradiated with metallic pulsed laser beam and analyzed the surface characteristics by using transmission and conversion electron Mossbauer spectroscopy to show the onset of crystallization

in the irradiated area [41]. Revitrification of partially crystallized $Fe_{81}B_{13.5}Si_{3.5}C_2$ metallic glass was observed.

Sypien *et al.* has done TEM studies on the nanocrystallisation of $Fe_{80}Si_{11}B_9$ alloy by Nd:YAG pulsed laser heating and observed the nanocrystallization of amorphous material and nucleation of nanocrystals regularly distributed in the amorphous matrix [42]. Microstructural changes observed on the surface depend on the temperatures obtained during laser heating. Preheating of the amorphous material caused by heating rates of 10^6 Ks^{-1} during laser treatment results in uniform nucleation of nanocrystals throughout the matrix and formation of grain boundaries between the nanocrystallites was observed.

Quintana *et al*. investigated the micromachining of amorphous and crystalline $Ni_{78}B_{14}Si_8$ alloys with micro-second and pico-second lasers by using Nd:YAG laser with a wavelength of 1064 nm, pulse duration of 10 μs for μs laser processing and mode-locked Nd:YVO_4 laser source with a wavelength of 532 nm, pulse duration of 10 ps for ps laser ablation [43]. Shape and topography of craters created by the single pulses by varying laser energy in both materials were studied [43]. By analyzing the craters, he observed that micro-second and pico-second lasers do not lead to materials crystallization and hence short-range atomic ordering of metallic glasses can be retained. It was observed that, when processing the amorphous materials with laser, it resulted in significant ejection of the molten material from bulk, followed by its partial redeposition around the craters due to surface tension forces [43]. Higher surface integrity has been observed with no signs of crack formation. It was observed that processing with ps laser resulted in reduction in amount of molten material deposited around the holes due to photothermal and photochemical effects characteristics of laser ablation with ultra short durations [43]. Fig. 2.3 shows the microstructure of the single pulse craters produced by μs laser and ps laser. Better stress accommodation and uniform dissipation of laser energy in metallic glass was observed.

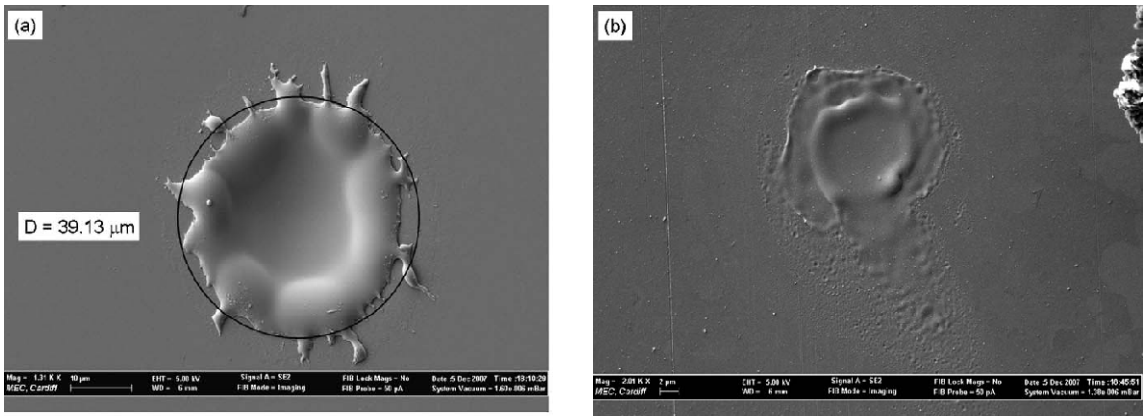

(a) (b)

Fig. 2.3 (a) SEM images of single pulse craters produced by ms laser ablation of amorphous Ni alloys with an average power: 3W, and (b) SEM images of ps laser ablation of amorphous foil with an average power 150 mW [43].

In the recent years, the use of femtosecond laser pulses has drawn tremendous interests due its precision micromachining applications. As the pulse duration is ultrashort (shorter than the thermalization time from electron to lattice of several picoseconds), intensity of laser is high which results in direct creation of plasma with ultrafast electric processes, without recast material and negligible heat effected zone. Advantages of fs laser pulses over longer pulses are high peak powers, absence of heat effected zone local to micromachined feature, minimized structural changes, contour sharpness improvement, thermal sensitivity, three dimensional micromachining, material independent, high process efficiency, structure size in nanometer range, higher repeatability, and precise ablation threshold [44-48] .

Wang *et al.* investigated on the fs laser ablation of Zr based amorphous alloy by performing analysis on the material having composition $Zr_{65}Cu_{17.5}Ni_{10}Al_{7.5}$ [49]. It was observed that there will be no heat effects on the material such as, those observed with the longer pulses

(above picoseconds), high temperature, and high strain rate conditions as in conventional machining [49]. By femtosecond laser, machining without defects like crystallization, burr and spatter are observed. Circular crater with up-heaved circular edges is observed in the single pulse ablation region. Periodic ripples and fin like morphology is observed in multi pulse ablation region. Slight oxidation in nanometer scale was identified. Micron-size scale holes and trenches were machined without crystallization around the ablated region [49]. Wang *et al.* discussed on the optimum fluence at which machining without crystallization can be observed [50]. It was observed that fs laser could result in either nonthermal or thermal ablation depending on the incident laser fluence.

Wang *et al.* investigated on the effects of femtosecond laser ablation on the surface morphology and microstructure of a bulk $Ti_{40}Cu_{36}Pd_{14}Zr_{10}$ glass alloy [51]. Ripple like patterns with porous surface were observed at various laser energies on the glass alloy surface as shown in Fig. 2.4 (a). The loss in mass content of Ti, Zr and Pd elements along with an increase in Cu content was observed with increasing energy. Crystallization of the amorphous alloy surface was observed during femtosecond laser ablation process. Fig. 2.4 shows the surface microstructure having ripples after treatment with laser and the X-ray patterns shows the crystallization of material with formations of the various crystalline phases.

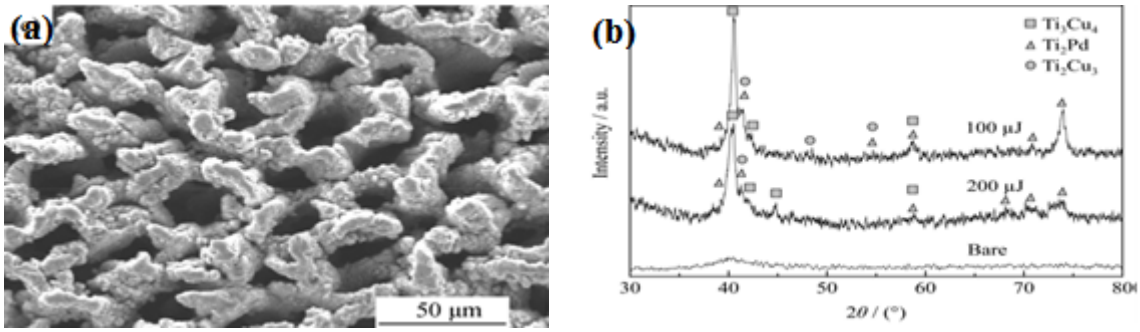

Fig. 2.4 (a) Surface microstructures of the specimen after laser treatment with the laser energy 200 µJ, and (b) XRD patterns of $Ti_{40}Cu_{36}Pd_{14}Zr_{10}$ bulk glassy alloys specimens ablated with a fs laser [51].

Jia *et al.* studied on change in surface morphology and grain structure of amorphous $Fe_{73.5}Cu_1Nb_3Si_{13.5}B_9$ alloy ablated with femtosecond laser pulses [52, 53]. Heat effects were observed during machining with fs pulses. Presence of crystallization was observed at the rim of the laser ablated holes. Ripple like patterns are observed in the ablated region. Fig. 2.5 shows the microstructure of the ablated regions with ripple like patterns at different laser fluence. Results obtained in this study indicate the formation of liquid phase, thus showing that femtosecond laser ablation process is not limited to a direct solid-vapor transition but also involves less substrate heating and structural transformations in the surrounding material.

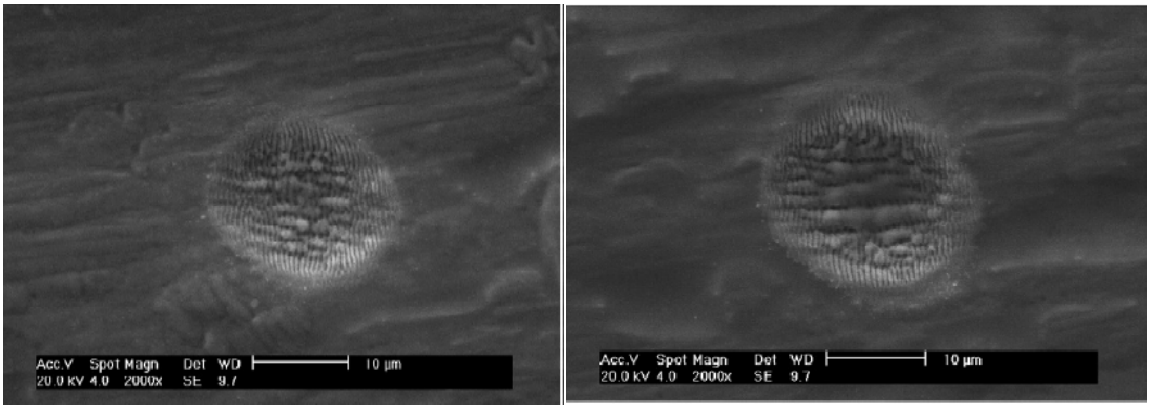

(a) (b)

Fig. 2.5 SEM images of craters produced in amorphous FeCuNbSiB alloy ribbon at 50 shots (a) 3.18 J/cm^2, and (b) 6.36 J/cm^2 [52].

2.2 Corrosion Behavior of Metallic Glass Ribbons- Review:

The importance for the corrosion resistance of metallic glasses in various industries led to the investigations on the electrochemical behavior of various amorphous alloy ribbons. All the available reports in literature focused on studying the corrosion resistance in different test environments and by changing the chemical compositions.

Asami *et al*. studied on the corrosive behavior of Fe-10at.%Cr-13at.%P-7at.%C alloy (20 µm thickness) in 1 N HCl and series of iron-chromium amorphous alloys by increasing the content of chromium in de-aerated 1M H_2SO_4 [54, 55]. Hashimoto *et al.* studied the corrosion resistance and passivity of chromium containing amorphous alloys [56, 57]. Their group observed the structural, compositional changes after corrosion, and observed that high corrosion resistance of amorphous alloy is attributed to the formation of passive film which consists mainly of hydrated chromiumoxyhydroxide.

Naka *et al.* investigated on the corrosion resistance and electrochemical behavior of amorphous iron-chromium alloys by adding different sets of glass forming metalloid elements like boron, carbon, silicon and phosphorus and conducted experiments in two different test environment of 0.1N H_2SO_4 and 3% NaCl [58]. With 0.1N H_2SO_4 [58] it was observed that corrosion resistance increases in the order of alloys containing silicon, boron, carbon and phosphorus; whereas with 3% NaCl, corrosion resistance increases in the order of alloys containing boron, silicon or carbon, and phosphorus. The difference in resistance levels is attributed to the formation of chromium-enriched protective surface film on the alloys. Basically metalloid elements accelerate active alloy dissolution causing rapid formation of passive film.

Hanham *et al.* studied the corrosive behavior of amorphous iron alloys $Fe_{70}Cr_{10}P_{13}C_{7,}$ $Fe_{60}Cr_{10}Ni_{10}P_{13}C_{7,}$ $Fe_{20}Ni_{60}B_{20}$ in 2N H_2SO_4 and observed the importance of elemental compositions in controlling the corrosive behavior [59]. Potentiodynamic polarization behavior of the $Fe_{70}Cr_{10}P_{13}C_{7,}$ $Fe_{60}Cr_{10}Ni_{10}P_{13}C_7$ are shown in Fig 2.6. It shows that active region is almost non-existent and follows directly into passive region indicating that highly uniform protective passive film in presence of chromium as described earlier. $Fe_{20}Ni_{60}B_{20}$ metallic glass actively corroded without anodic passivation.

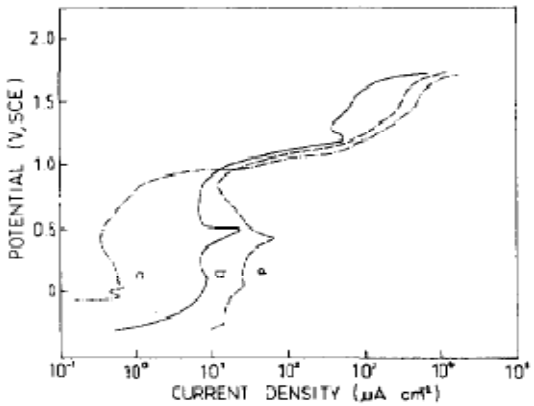

Fig. 2.6 Potentiodynamic polarization curve in 2N H_2SO_4 for the $Fe_{70}Cr_{10}P_{13}C_7$ (curve a), $Fe_{60}Cr_{10}Ni_{10}P_{13}C_7$ (curve b), and $Fe_{60}Cr_{10}Ni_{10}P_{13}C_7$ (curve c) [59].

Rife *et al.* further extended his study on corrosive behavior of various iron-, nickel- and cobalt-base glasses containing boron and silicon, with and without the addition of chromium by analyzing the potentiodynamic anodic polarization data in H_2SO_4 [60]. Rife *et al.* conducted experiments with potential scan rates of 0.6 Vh^{-1}, 3.0 Vh^{-1}, and 6.0 Vh^{-1} until a maximum potential of 1.75 V is achieved and reported the influence of alloying elements molybdenum, niobium and tantalum in iron based amorphous alloys [60]. It reports the similar conclusion like the previous authors [54, 55, and 59] i.e., chromium concentration is a primary factor in determining the corrosion resistance.

Magrini *et al.* studied on the electrochemical behavior of the Fe-Ni-Mo-B amorphous alloys in various environments such as acidic, alkaline and neutral solutions and reported potentiodynamic anodic and cathodic polarization curves for the amorphous alloys by varying Nickel and Molybdenum content in alloy [61]. It was observed that increasing the Nickel content enhanced corrosion resistance in all the environments, whereas increasing the molybdenum content enhances resistance to corrosion in only alkaline solutions [61].

Chattoraj *et al.* reported the corrosive behavior of amorphous $Fe_{77.5}Si_{7.5}B_{15}$ fibers by annealing in air [62-64]. It reported the corrosion properties of different annealed fibers by studying polarization in 1N sulphuric acid and in 3.5% NaCl solutions. First, he reports the magnetic properties of the alloys after corrosion. Then, he reports the affect of crystallization on the corrosive behavior of these alloys by annealing at crystallization temperature (~540^{o}C).

Alvarez *et al.* investigated on the corrosive behavior of $Fe_{73.5}Si_{13.5-x}Al_xB_9Nb_3Cu_1$ (x = 0–2) (FINEMET alloy [66]) amorphous alloy in 1M NaCl solution [65]. Surface layer enriched with silicon is observed after corrosion. This paper tried to give good correlation between the microstructural changes and electrochemical response of alloys studied [65]. Cremaschi *et al.* conducted electrochemical studies on the various amorphous, nanocrystalline, crystalline FeSiB alloys in 1M NaCl with potential scan rate of 0.2 mV/s by studying the influence of pH and addition of Sn, Cu, Nb, and Al elements in the alloy [67].

Marzo *et al.* studied on similar FINEMET alloy by adding chromium in the place of Aluminium [68]. He came to the similar conclusion i.e., increase in corrosion resistance with increased chromium content as usual. Altube *et al.* studied on the electrochemical response of FINEMET alloy by adding cobalt [69]. Marzo *et al.* studied on the effect of Cu- cluster size and electrochemical response of FINEMET alloy in KOH solutions [70]. Vara *et al.* investigated on the influence of adding Nickel content in the electrochemical behavior of FINEMET type amorphous and crystalline alloy and observed an improvement in the electrochemical response of the alloy with change in Nickel content [71].

Shivaee *et al.* reported the influence of annealing temperatures on the electrochemical behavior of FINEMET alloy [72]. After annealing the samples near to crystallization temperature amorphous and nanocrystalline phases are formed and observed the structural relaxation and nanocrystallization in the samples annealed at 600 ^{o}C. It reports the improved corrosive behavior

of the heat treated samples at 650 ^{o}C [72]. The enhanced corrosion resistance is because of FeSi nanoparticles nucleated in the amorphous matrix. It. concluded that nanocrystallisation is more effective in improving the corrosion resistance than the structural relaxation [72]. Fig 2.7 shows the Tafel plots corresponding samples annealed at various temperatures.

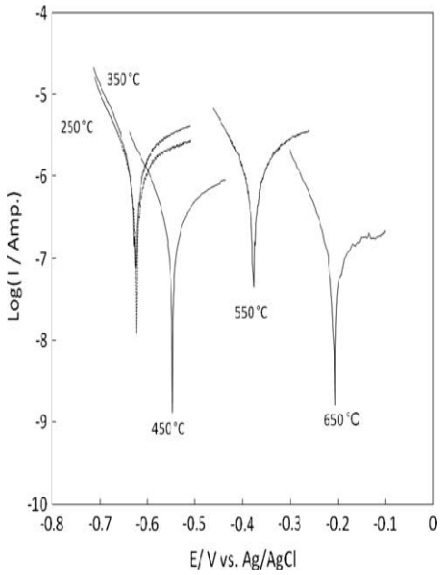

Fig. 2.7 Comparison of Tafel plots data recorded using linear sweep voltammetry at the scan rate of 1 mV s^{-1} after 1 h remaining in 0.10 M NaOH solution [72].

2.3 Wear Behavior of Metallic Glass Ribbons- Review:

Study on the tribological properties of the amorphous alloys is of significant scientific and practical interest due to its potential of having wide range of engineering and structural applications. These are associated with higher strength, higher microhardness, higher yield strength, and higher fracture toughness. Amorphous alloys are expected to show higher resistance to different types of wear due to high hardness and absence of grain boundaries.

Klinger *et al.* studied on the tribological behavior of amorphous alloy $Fe_{40}Ni_{40}B_{20}$ (ribbon of 27 µm thickness) under different sliding conditions by means of a cylinder-pin apparatus [73]. It was observed that under the normal force of up to 5 N the metallic glass $Fe_{40}Ni_{40}B_{20}$ exhibited higher wear resistance and relatively higher friction coefficient (µ=0.4-0.9) [73]. This paper reported that higher coefficient of friction is due to formation of oxides [73] and reported that coefficient of friction can be lowered substantially by lubricating with graphite and MoS_2.

Lee *et al.* studied on the coefficient of sliding friction for three different metallic glasses $Fe_{40}Ni_{40}B_{20}$, $Fe_{40}Ni_{40}P_{14}B_6$, and $Fe_{40}Ni_{38}Mo_{14}B_8$ (ribbons of thickness 50 µm and 60 µm) in helium and oxygen atmospheres [74]. The relatively low coefficients of friction (µ< 0.35) were observed due to absence of strain hardening, thin low density coating of inhomogeneously sheared metallic glass, high strength, and hardness of these materials. Increase in friction coefficient with sliding distance is observed due to accumulation of more debris and surface deterioration. Crystallinity in wear debris and friction coefficient reduction with increase in sliding speed due to its lesser time for structural relaxation was observed.

Nishi *et al.* investigated on the wear resistance of the Fe-Co-Si-B amorphous alloy (average thickness is ~40 µm) during wet wear test by conducting studies on the wear resistance of alloy depending on the cooling rate and metal composition [75]. With increasing the cooling rate, higher wear resistance was observed and also reported that the composition difference doesn't effect much in wear resistance like the faster cooling rates but slightly changes with sample thickness [75].

Kishore *et al.* studied the tribological behavior of amorphous alloys with nominal composition $Ni_{78}Si_8B_{14}$, $Fe_{81}B_{13.5}Si_{3.5}C_2$, $Fe_{67}Co_{18}B_{14}Si_1$ (average thickness is ~40 µm) during sliding wear in order to understand the wear mechanism [76]. Considerable plastic flow at the contact surface of the glasses is observed and the alloys predominantly remain glassy in the dry

sliding conditions. Dynamic recrystallisation process of the wear debris was observed at high strain rates due to local frictional heating of the surface of amorphous alloys. Crystallization of $Ni_{78}Si_8B_{14}$ amorphous alloy is observed during the wear. A fine grained nanocrystalline textured layer generated during process of friction proved detrimental in process of wear in amorphous alloys. In addition to the frictional heating (at very small sliding velocities) nanocrystalline structure is formed as a result of severe plastic deformation of the surface layer due to joint action of high shear and compressive contact stresses [77].

Prakash *et al.* investigated on the sliding wear behavior of different Fe, Co and Ni based metallic glass ribbons ($Fe_{81}B_{13:5}Si_{3:5}C_2$, $Co_{66}Fe_4Ni_1B_{14}Si_{15}$, $Ni_{72:5}Cr_{18:5}Si_{7:5}B_{1:5}$, $Ni_{91}Si_7B_2$, $Fe_{78}B_{13}Si_9$, $Fe_{40}Ni_{38}Mo_4B_{18}$, $Fe_{77}Cr_2B_{16}Si_5$, and $Fe_{66}Co_{18}B_{15}Si_1$) with thickness in the range of ~30 µm under reciprocating sliding conditions and observed that the wear resistance of the metallic glasses depend on the material transfer phenomena and formation of oxide layer during sliding [78]. Chemical composition of the metallic glass, nature of mating material and surface chemical reactivity of metallic glass surface determines the material transfer phenomena and formation of oxide layer. Prakash *et al.* investigated on the abrasive wear behavior of same amorphous alloys under unidirectional and reciprocating sliding conditions to compare the wear characteristics [79]. Almost all the metallic glasses exhibited similar wear behavior in both the sliding conditions. Wear resistance exhibited by these alloys is not similar to the microhardness of these alloys which is due to occurrence of micro-cracking. Micro-cracking or cutting occurs due to its poor ductility in tension (since materials experience higher tensile stresses during wear) and enhanced brittleness.

Korshunov *et al.* investigated on the structural transformations and abrasive wear resistance of the $Fe_{64}Co_{30}Si_3B_3$, $Fe_{82.6}Nb_5Cu_3Si_8B_{1.4}$, $Co_{86.5}Cr_4Si_7B_{2.5}$, and $Fe_{81}Si_4B_{13}C_2$ amorphous alloys (ribbon 30 µm thick) upon sliding over fixed abrasives (corundum and silicon carbide) and observed that micro-cutting of the material occurs during the wear [80]. Ductile character of

fractured surface was observed which is connected with severe localized plastic deformation. It was reported that abrasive resistance of the amorphous alloys is low compared to their micro-hardness due to the softening behavior of the amorphous alloy surface during the process of wear which is attributed to the heterogeneous plastic flow due to combined action of higher shear and contact compressive stresses. It reports that deformation induced softening is responsible for the low level of abrasive resistance for amorphous alloys studied. It was observed that small amount of nanocrystalline phases on the surface due to high compressive contact stresses which doesn't affect wear and microhardness significantly. Major volume of the alloy surface deformed by the abrasive particles still remains amorphous with small amount of nanocrystalline phase.

Korshunov *et al.* has done the investigations on the similar alloys at different atmospheres like at room temperatures (in air, argon and liquid nitrogen) and cryogenic temperatures and extended their observation by carrying both adhesive and abrasive wear on sliding friction [81]. Upon abrasive wear all alloys exhibit the same behavior which is explained above. But during adhesive wear partial crystallization of surface layer is observed more intensely than upon abrasive wear, due to activation of the processes of plastic deformation and growth of compressive contact stresses. Decrease in effect of deformation softening due to partial crystallization is reported. No significant change in the wear behavior during both atmospheres is observed.

Korshunov *et al.* investigated the wear resistance and structural changes in the amorphous alloys $Fe_{64}Co_{30}Si_3B_3$ and $Fe_{73.5}Nb_3Cu_1Si_{13.5}B_9$ during wear by using a fixed abrasive (an emery paper) and observed wear properties by tempering the alloy [82]. Increase of micro hardness and wear resistance was observed by tempering $Fe_{73.5}Nb_3Cu_1Si_{13.5}B_9$ amorphous alloy at 500 °C due to formation of a nanocrystalline structure with the retention of a certain amount of the amorphous phase. When temperature increases to 540 °C complete crystallization of alloys

occurs which resulted in enhanced brittleness of the alloy which leads to sharp reduction in wear resistance was observed.

CHAPTER 3

PROBLEM STATEMENT

- The first objective was to investigate the morphological and microstructural changes caused by excimer laser micromachining on the 40 µm thick $Fe_{85\text{-}95\%}Si_{5\text{-}10\%}B_{1\text{-}5\%}$ metallic glass ribbon and 3.86 mm thick $Fe_{48}Cr_{15}Mo_{14}Y_2C_{15}B_6$ bulk metallic glass. It was studied by varying the operating conditions such as pulse width, number of pulses, and pulse energy. Series of experiments initially helped us in optimization of the process parameters for the conducting the study on initiation of craters. The surface quality, microstructure and change in chemical composition of the craters produced by laser were analyzed by optical microscope, MicroXAM laser interference microscope, SEM and EDS respectively. Change in phase on the craters was studied by X-ray diffraction patterns.
- The second objective was to study corrosive behavior of the as received and heat treated $Fe_{85\text{-}95\%}Si_{5\text{-}10\%}B_{1\text{-}5\%}$ metallic glass ribbon at various temperatures by comparing corrosion parameters and to study the wear performance of the $Fe_{85\text{-}95\%}Si_{5\text{-}10\%}B_{1\text{-}5\%}$ metallic glass ribbon at various operating conditions.

CHAPTER 4

EXPERIMENTAL PROCEDURE

4.1 Iron-Based Metallic Glasses:

The materials used in this study were iron-based metallic glass ribbon ($Fe_{85-95\%}Si_{5-10\%}B_{1-5\%}$), and iron-based bulk metallic glass ($Fe_{48}Cr_{15}Mo_{14}Y_2C_{15}B_6$). Iron based metallic glass ribbon with nominal composition of $Fe_{85-95\%}Si_{5-10\%}B_{1-5\%}$ (of thickness 40µm) supplied by Metglas® Inc with Product No.: 2605 SA1) was taken for our study. Table 4.1 shows the properties of ribbon.

Table 4.1: Physical properties of the $Fe_{85-95\%}Si_{5-10\%}B_{1-5\%}$ metallic glass ribbon [84].

Physical Properties			
Density (g/cm3) As Cast	**7.18**	Elastic Modulus (GPa)	**100-112**
Vicker's Hardness (50g load)	**900**	Crystallization Temperature (°C)	**508**
Tensil Strength (GPa)	**1-2**	Lamination Factor(%)	**>82**

Iron-based bulk metallic glasses with nominal composition of $Fe_{48}Cr_{15}Mo_{14}Y_2C_{15}B_6$ (of thickness 3.86 mm) are prepared by spark plasma sintering (SPS) technique. A mixture of pure elemental powders (particle size < ~ 25µm) of Fe, Cr, Mo, Y, C, and B (all with greater than 99.9% purity) with nominal chemical composition of (in at %) $Fe_{48}Cr_{15}Mo_{14}Y_2C_{15}B_6$ was melted under high purity argon gas and atomized using high purity inert gas. The sintering of the powder is conducted at a temperature of 550 ^oC and pressure of 80 MPa by maintaining a holding time of 20 min in order to obtain a bulk shape with relative density of 92.4 %.

4.2 Description of Excimer Laser Micromachining System

The excimer laser micromachining system used in this investigation comprises of three main components (1) excimer laser generator system, (2) stage and motion controller system, and (3) optical or laser beam delivery system. A computer station is used to interface the excimer laser generator system with the stage and motion controller.

4.2.1 Gas System:

Table 4.2 give the specifications of gas system used. All the gas cylinders have a ¼" Gyrolock pressure regulator and the gases are injected and stored in laser tube. When there is significant drop in laser energy, spent gases laser tube needs to purged and replaced with fresh gas. All the gas lines are connected from cylinders to the laser tube by stainless steel 316 L of diameter 6 mm. All the gas cylinders should be opened while filling with fresh gas and valves should be closed in all the other times. A vacuum pump is connected to the evacuation outlet for purging all the used gases from laser tube to a suitable exhaust.

Table 4.2: Purity of the gases to be used [85].

	Buffer	**Rare**	**Halogen**	**Inert**
Types of gas	Ne	Kr	5%Fluorine/ 95% He	He
Purity	99.99%	99.99%	99.99%	99.99%

4.2.2 Cooling System:

Air and water cooling system are used in order to cool the laser tube and maintain the temperature in the COMPex Laser. Air is constantly sucked in at a throughput of 300 m^3/hr. A temperature control valve is available inside the Laser which maintains the temperature below

35^{o}C by allowing the cooling water (2-3 l/min, 15-20^{o}C) to flow in. Diameter of hose line is ½''inch and permissible water pressure is 4 bar.

4.2.3 Excimer Laser Generator System:

The excimer laser beam generator used in this investigation is COMPex 205i laser manufactured by Lambda Physik generating a medium power of 25 W. It is short pulse (FWHM=25 ns) excimer laser connected to 115 V (10%), 25 A power supply. It is used for variety of micro processing operations such as in micro-drilling, micro-cutting, micro-marking and in surface treatment. This laser utilizes krypton fluoride (KrF) gas as the lasing medium to deliver a laser beam with wavelength of 248 nm. Table 4.3 gives the illustration on the specifications of compex excimer laser. The typical lifetime of gas of COMPex 205i excimer laser in order of 10^{6} laser pulses. Fig. 4.1 and Fig. 4.2 shows the photographs and the schematic of the experimental setup used for laser micromachining.

Table 4.3: Specifications of Lambda Physik Compex 205i excimer laser [85].

COMPEX 205i Excimer Laser	**KrF**
Wavelength	248 nm
Energy	650 mJ
Maximum average power	30 W
Maximum pulse repetition rate	50 Hz
Nominal pulse duration	25 ns
Orientation of the laser beam	horizantal
Beam Divergence	3 x 1 mrad
Beam Dimensions	24 x 6^{-12} mm^{2}

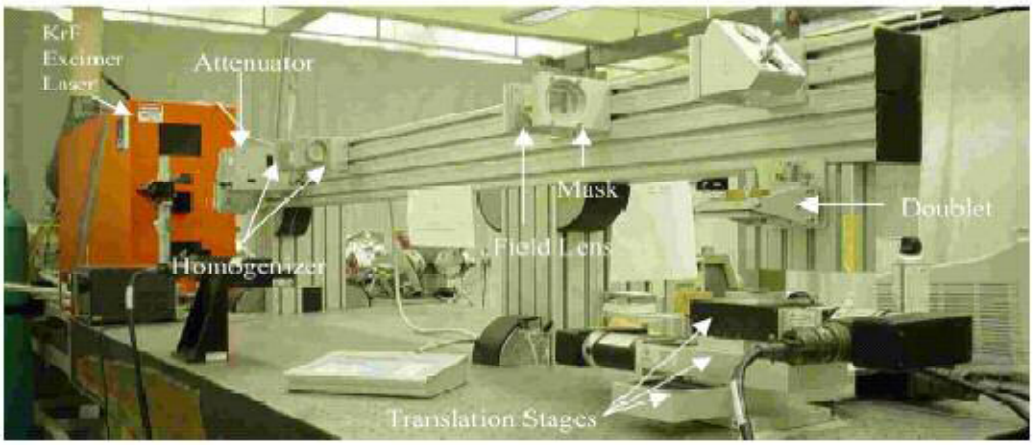

Fig. 4.1 Experimental setup of the excimer laser micromachining with associated optics [83].

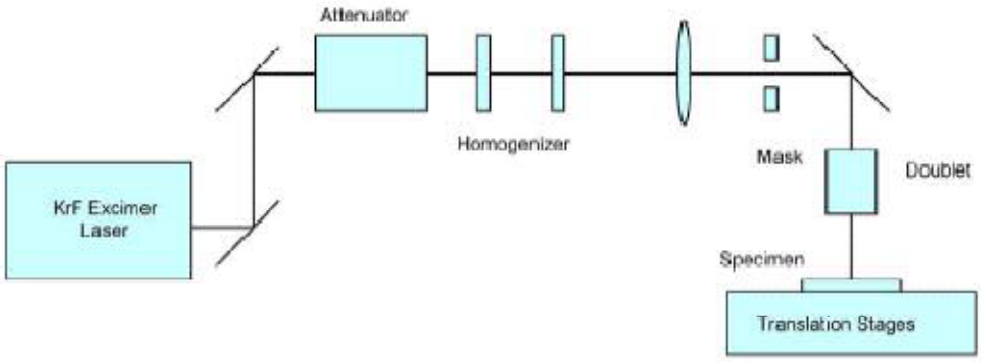

Fig. 4.2 Schematic of experimental setup used in laser micromachining [83].

4.2.3.1 Laser Tube:

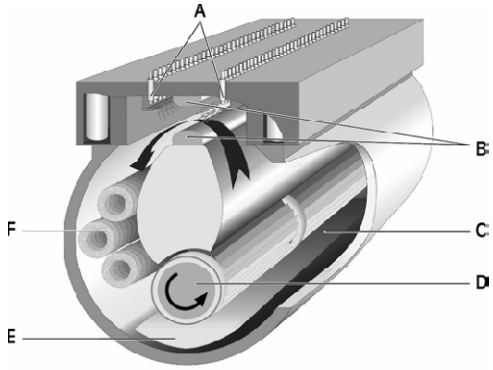

Fig. 4.3 Cross-section of laser tube [85].

All Lambda Physik COMPex 205i lasers use the NovaTube® technology which eliminates the effects of corrosion and contamination. Fig. 4.3 shows the cross-section of the laser tube in the excimer laser generator. The laser tube (C) is the reservoir for the laser gas. A high voltage discharge between the electrodes (B) transfers the energy to the excimer gas mixture (e. g. fluorine or krypton premix). In order to obtain a controlled, spark-free discharge, the laser gas has to be preionized i.e., a sufficiently high density of free charged molecules has to be created between the electrodes. This is achieved with preionization pins (A) arranged along the main electrodes which results in homogeneous preionization of laser gases. The switching of preionization and main discharge in series ensures perfect synchronization between preionization and main discharge. After the high-voltage discharge, thermal inhomogenities in the laser gas arise in the discharge area. Therefore, the gas volume in the discharge area has to be completely exchanged between two laser pulses. A transverse circulation fan (D) positioned within the laser tube causes the gas volume between the main electrodes to be completely replaced between two successive laser pulses. The gas, heated up by the discharge, reaches the heat exchangers (F) as a result of the flow in the laser tube and is cooled down to the correct operating temperature (approx. 30 °C or 86 °F). Each discharge pulse of the laser results in a load on the preionization

pins and main electrodes and causes a slight erosion of material. Precipitation of the created particles on the laser windows would results in diminishing beam intensity by scattering and absorption. Therefore, these particles must permanently be removed from the laser gas which is done by an electrostatic filter (E) integrated in the gas circulation. Due to the pressure conditions generated by the circulation fan, the laser gas continuously flows through this electrostatic filter. Table 4.4 gives the optimum gas mixtures used in laser tube.

Table 4.4: Optimum gas mixtures required in laser tube [85].

Gas Mixture (wavelength)	**Partial Pressure (mbar)**	**Gas**	**Pressure (%)**	**Gas port**	**Total Pressure (mbar)**
KrF (248nm)	80	F_2/He	0.12/2.30	Halogen	3200
	100	Kr	3.03	Rare	
	3120	Ne	94.55	Buffer	

4.2.3.2 Laser Controller:

The laser generator system is controlled by two triggering methods such as Internal Trigger and External Trigger.

Internal Trigger:

It has control panel which is connected to the trigger. The control panel is used to purge the gases, perform the new fill, change the output energy and power from the laser. It controls the repetition rate and firing of the laser pulses.

External Trigger:

The external trigger is connected to the computer station to which interfacing of the stage and motion controller is done. Pulse rate, pulse width and commands to fire the laser are sent through the cable connected to this trigger.

4.2.4 Stage and Motion Controller System:

Fig 4.4 shows a schematic of UNIDEX 500 control system. It is a combination of the U500 PC bus-based motion control card, the windows-based tool kit or MMI interface software, and any various optional accessories. The U500 system integrates with amplifiers and positioning stages to form a complete programmable, customized control system that is suitable for a wide range of motion control applications. The UNIDEX 500 control card is available in three models (Base, Plus and Ultra) to provide a level of motion control to match any application. The Base model contains the basic version of the UNIDEX 500 family whereas the ultra version consists of the most versatile version of the U500 family of controllers.

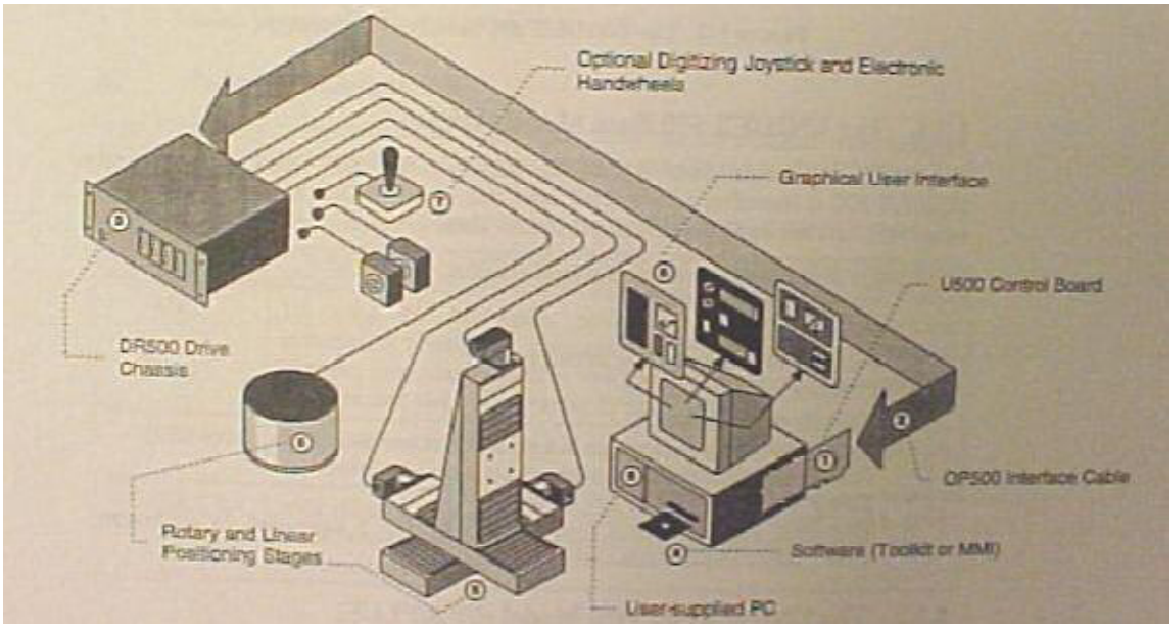

Fig. 4.4 UNIDEX 500 system diagram [86].

4.2.5 Optical or Laser Delivery sytem:

Fig. 4.5 shows the schematic of the optic delivery system. The optical delivery system consists of five main parts: (1) attenuator module, (2) homogenizer, (3) field Lens, (4) mask, and (5) doublet.

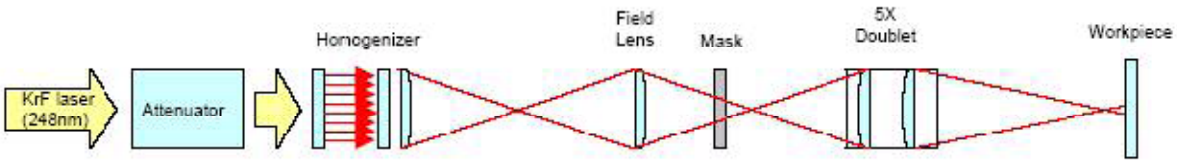

Fig. 4.5 Schematic of the optical delivery system for laser micromachining [87].

4.2.5.1 Attenuator Module:

It is mainly used to control the intensity of the laser beam. The optical attenuator uses a specially coated attenuating element and a counterrotating compensator plate. The compensator plate compensates the beam displacement. The elements are coated for a specific excimer laser wavelength. The angle of the elements can be varied using a hand –driven dial on the front panel of the attenuator housing. The optical transmission changes from 10% to 90% [87].

4.2.5.2 Homogenizer:

The main purpose of homogenizer is to cut the raw excimer laser beam (non-homogeneous intensity profile) into segments and overlay the segments at the object plane to create a homogeneous intensity profile. It consists of two arrays of cylindrical lens and a condenser lens. These arrays can be single axis arrays or crossed arrays. Homogenizer helps in illuminating a homogeneous beam at the location of the mask. In this investigation dual axis homogenizer is used [87].

4.2.5.3 Field Lens:

The function of the field lens is to gather the laser beam and converge it into a doublet. Thus this field lens facilitate in obtaining a clear and uniform intensity laser beam. Otherwise, it would be dark and shadowed along the edges [87].

4.2.5.4 Mask:

The main function of the mask is to control the shape of the structures formed on the substrate. Thus the final shape formed on the substrate can be controlled by the type of the mask used. There are three different kinds of masks used. They are 1) free standing metal mask, 2) metal film on quartz substrate, and 3) dielectric mask [87].

4.2.5.5 Doublet:

The imaging doublet is composed of 2 spherical lenses, each with a radius of curvature of r=50 mm. These lenses are mounted with a seperation of about 7 mm of the curved surfaces, The doublet is mounted with the curved sides of the lenses both pointing towards the object (mask). The main function of doublet is to demagnify the object. Table 4.5 gives the distance from the mask plane to the center of the doublet and from the center of the doublet to the image plane [87].

Table 4.5: Distance from the mask plane to the center of the doublet and from center of the doublet to the image plane [87].

Demagnification	**5x**
Object Distance	306 cm
Imgae Distance	61.2 cm
Track Length	367 cm

4.2.6 Alignment of the Excimer Laser Optical System:

In order to obtain the maximum output power from the laser system, it is necessary to align the optical rail assembly components. The alignment procedure is given in Lambda Physik Instruction Manual.

Optical delivery system consists of 5 parts as shown in section 4.2.5. All the alignment procedure for the optical elements have to be set in by maintaining the respective between the parts as shown in Fig. 4.6. The procedure is given in MicroLAS Excimer Laser Based Microamchining System [87].

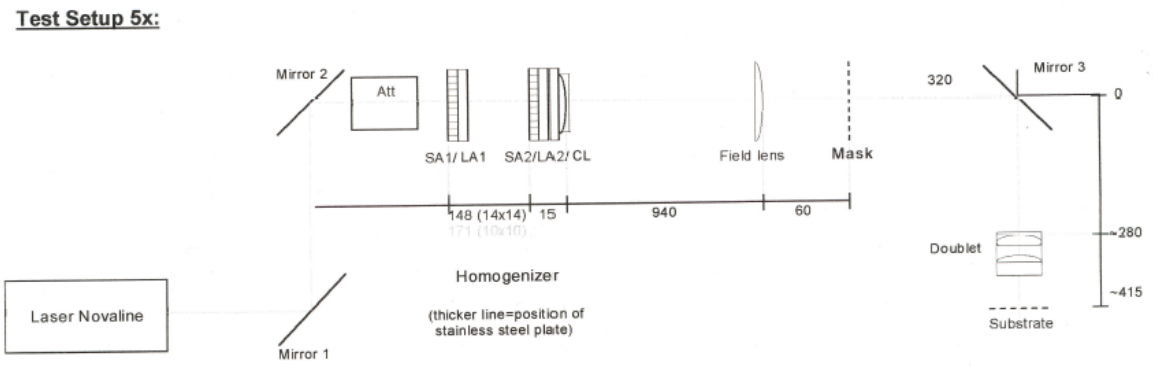

Fig. 4.6 Distance to be maintained in order to align the Laser beam [87].

4.2.7 System Operational Instruction:

The system operation instructions are given in Appendix and may be referred for details.

4.3 Sample Preparation:

First, sample has to be mechanically polised with different grade emery papers (400,800, and1200). Fine polishing has to be done with alumina powder solution until mirror finish is obtained. As the excimer laser micromachining process is very sensitive, care was taken in

removing any thin layer of dirt or oil on surface of sample which can influence the absorption of the UV light. In order to eliminate detrimental side effects, cleaner surface is needed. The following cleaning procedure will remove most of the surface contamination.

1. Place the sample in a beaker with acetone solution and beaker is kept in ultrasonic stirrer for 180 sec.
2. Rinse the sample with distilled water
3. Place the sample in beaker with distilled water and beaker is kept in an ultrasonic stirrer for 180 sec.
4. Use compressed air to dry the sample.

4.4 Input Energy:

The input energy was varied from the output laser beam by controlling it through the external panel terminal of the excimer laser. A Molectron M400 energy detector was used to measure the energy from the laser beam.

4.5 Determination of Focus length:

Before conducting the micromachining experiment, focus length has to be determined in order to have exact focus of the laser beam from the doublet to the substrate. Multiple experiments were performed to obtain the exact focal length in order to perform the micromachining experiment. Optimum focal length to be maintained between the doublet and the substrate was observed as 95.82-95.64 mm which is determined after series of experiments. Care was taken in maintaining this distance according to the thickness of the material to be machined by rotating the meter scale at the doublet.

4.6 Microstructural Change and Elemental Composition Analysis:

4.6.1 Optical Microscopy:

An optical microscope was used to observe the surface profiles of the machines areas. Diameter and width of the irradiated area are measured at different micromachining conditions.

4.6.2 Scanning Electron Microscopy (SEM):

A scanning electron microscope (SEM) (JSM-6360, JEOL) was used to observe the detailed features of the laser irradiated areas like thermal damage, cracking, heat affected zones, redeposition. Care was taken in throughly cleaning any foreign particles on the sample before placing it in the SEM for observation. Higher and lower magnification images were taken to compare the surface features.

4.6.3 Energy Dispersive Spectroscopy Analysis (EDS):

Elemental composition of the as received and laser irradiated sample areas were investigated by the SEM equipped with energy dispersive x-ray Spectroscopy (EDAX). FEI Quanta 600 field-emission gun Environmental Scanning Electron Microscope with an Evex EDS x-ray microanalysis system and HKL EBSD system is used for EDS analysis.

4.6.4 MicroXam Laser Interference Microscopy:

As diameter and width of the holes generated by the micromachining is in the range of micrometers, it is difficult to cut the sample into half to observe the cross sectional features without damaging the original profile of the irradiated area. Laser interference microscope is used to examine these surfaces. It uses different wavelengths of light to scan the irradiated area and generates 3-dimensional profile of the area.

4.7 X-ray Diffraction analysis:

In order to identify the structure of the as received and laser irradiated crater areas, x-ray diffractometer operating with Cu K_a (λ = 1.54178 Å) radiation at 45 kV and 40 mA was used. The diffraction angle was varied between 20° and 90° 2θ at a step increment of 0.02° 2θ with a count time of 1 s.

4.8 Ball-on-Disk Wear Testing:

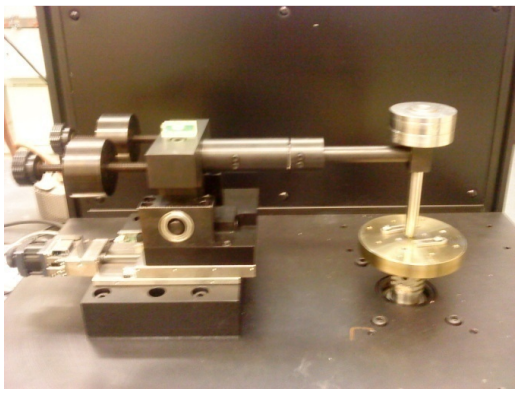

Fig. 4.7 Experimental Setup used in wear testing

The wear performance of the amorphous alloy ribbon was investigated by conducting sliding wear tests using Bal-on-Disk apparatus (Nanovea Tribometer). The standard test principle here is, a stationary ball with a defined normal force is pressed against the surface of test sample which is placed on the rotary disk. The normal force was applied over the ball by means of a set of dead weights. Fig. 4.7 shows experimental setup used in this study. First the sample was cleaned with acetone in the ultrasonic cleaner. The Alumina ball with a diameter of 6 mm was used as the counterface. Experiments were conducted under dry sliding conditions at the room temperature. Care had been taken in order to ensure flat contact between ball and test specimen. The frequency was 100 cycles per minute. Loads of 2 N, 4 N, 6 N, and 8 N were applied on the specimen. Tests were performed on the specimen for 2 min, 4 min, 6 min, 8 min, and 10 min

operation respectively with the loads mentioned above with a stationary ball and rotating wear cell. The average steady state coefficient of the friction was determined from the data collected during wear tests. The surface roughness of the as received sample and worn tracks is analyzed by Mahr's M1 Perthometer.

4.9 Characterization of Electrochemical Behavior:

The corrosion resistance of the amorphous alloy ribbon was studied by using VersaSTAT 4 (Princeton Applied Research) which has maximum current up to 1A. It has ±650mA / ±10V polarization range as standard which is ideal for the electrochemical applications like corrosion. In this study, we used Tafel technique to determine the corrosion potential (E_{corr}), corrosion current (I_{corr}). In this three electrode electrochemical cell was used, metallic glass ribbon sample was used as the working electrode, platinum was used as counter electrode and the reference electrode was a saturated calomel electrode (SCE). Area of the working electrode was 1 cm^2. Reference electrode used was Ag, AgCl / KCl (saturated) (0.197 volts). The corrosion properties of the coating were studied by polarization in 3.5% NaCl Solution with pH 7.0 held at room temperature [72]. As received and heat treated amorphous alloy ribbon is subjected to initial and final potential of -0.9 V and -0.3 V respectively. A constant potential scan rate of 0.167 V/sec is employed during the test. Tafel polarization curves were plotted during the whole test with the scan rate mentioned. The surface morphology and elemental composition of the corrosion tested and as received samples were investigated.

CHAPTER 5

RESULTS AND DISCUSSION

5.1 Excimer Laser Micromachining of Iron-Based Metallic Glasses:

5.1.1 Micromachining Response of Fe-Si-B Metallic Glass Ribbon:

Fig. 5.1 (a) shows the surface microstructure of the as received $Fe_{85\text{-}95\%}Si_{5\text{-}10\%}B_{1\text{-}5\%}$ metallic glass ribbon. The featureless region represents structurally homogeneous microstructure without any grains or grain boundaries. It has disordered atomic structure without any crystalline particles. Fig. 5.1 (b) shows the EDS pattern for the area shown in Fig. 5.1 (a). Fig. 5.1 (b) shows the presence of iron as major constituent, whereas presence of boron cannot be seen with this instrument due to its lower atomic number.

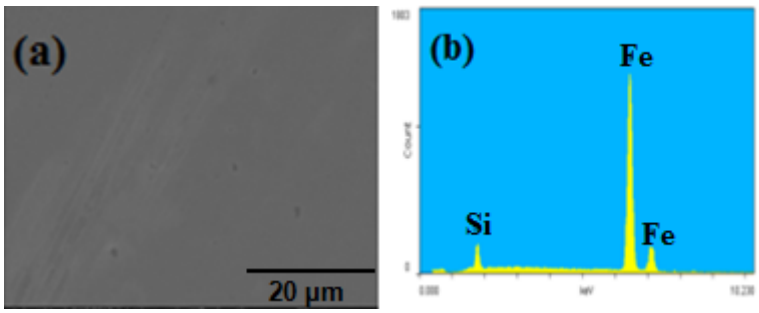

Fig. 5.1 (a) SEM image showing surface microstructure of as-received ribbon, and (b) EDS pattern for the SEM image in (a).

5.1.1.1 Parametric Analysis of Craters formed by Excimer Laser:

As-received $Fe_{85\text{-}95\%}Si_{5\text{-}10\%}B_{1\text{-}5\%}$ metallic glass ribbon is used as work material. The laser energies in the range of 100 mJ, 200 mJ, 300 mJ, 400 mJ, and 500 mJ were used. The surface of ribbon is irradiated with 1-5000 short laser pulses at a constant frequency of 10 Hz in order to observe the response of work material to excimer laser. Care was taken in clamping the sample perfectly flat on the substrate surface by using double sided tape.

Fig. 5.2, 5.3, 5.4, 5.5, and 5.6 shows the optical micrographs of the top views of the amorphous alloy ribbon work pieces micromachined at pulse energies of 100 mJ, 200 mJ, 300 mJ, 400 mJ, and 500 mJ respectively by using a circular mask of 1162 µm diameter at a constant frequency of 10 Hz.

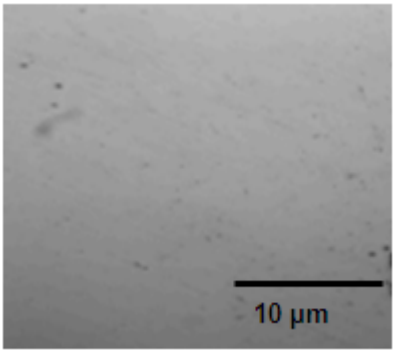

Fig. 5.2 Micromachining with 100 mJ pulse energy and 10 Hz frequency at 5000 pulses.

Fig. 5.2 shows the top view of the ribbon treated with laser energy of 100 mJ, 10 Hz pulse frequency, and 5000 pulses. Initiation of craters was not seen until 5000 pulses for the 100 mJ of laser energy.

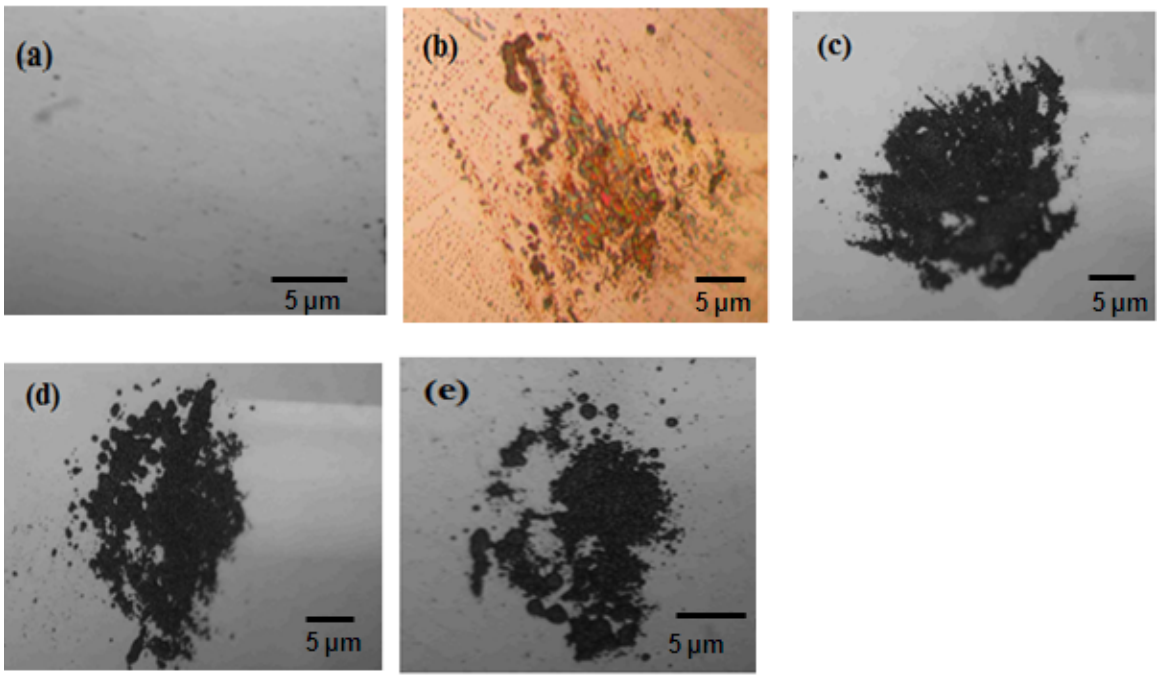

Fig. 5.3 Micromachining with 200 mJ pulse energy and 10 Hz frequency at (a) 500 pulses, (b) 1000 pulses, (c) 2000 pulses, (d) 4000 pulses, and (e) 5000 pulses.

Fig. 5.3 shows the top view of the ribbons treated with laser energy of 200 mJ and number of pulses in the order of 500, 100, 2000, 3000, and 4000 pulses. No effect of laser radiation on ribbon was observed for 500 pulses with 200 mJ pulse energy. But, at 1000 pulses and 200 mJ energy, laser induced crater is observed on the work material. Thus, it can be concluded that at 200 mJ pulse energy, 1000 pulses were the minimum threshold parameters to micromachine the material where the craters formed due to effect of laser on the work material was observed.

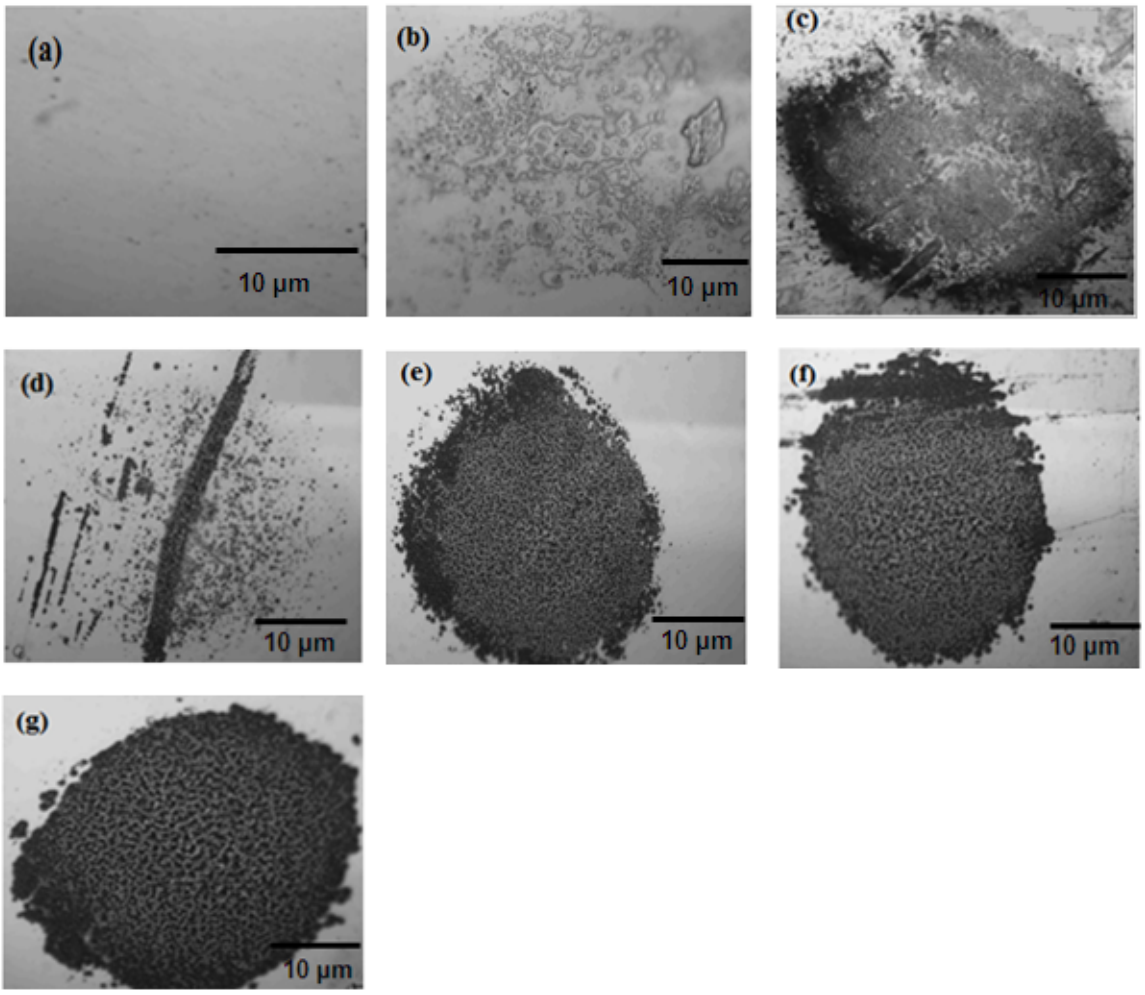

Fig. 5.4 Micromachining with 300 mJ pulse energy and 10 Hz frequency for (a) 400 pulses, (b) 500 pulses, (c) 1000 pulses, (d) 2000 pulses, (e) 3000 pulses, (f) 4000 pulses, and (g) 5000 pulses.

Fig. 5.4 shows the optical micrographs of the ribbon treated with 300 mJ pulse energy and 10 Hz pulse frequency at various numbers of pulses. At this particular energy, minimum number of pulses at which formation of craters takes place was observed at 500 pulses, since no laser induced crater was observed at 400 pulses. With increasing the number of pulses significant change in the microstructural features were observed. The diameter of crater produced with 300 mJ is larger than compared with the laser energy of 200 mJ. With increasing the number of pulses more pronounced craters was observed.

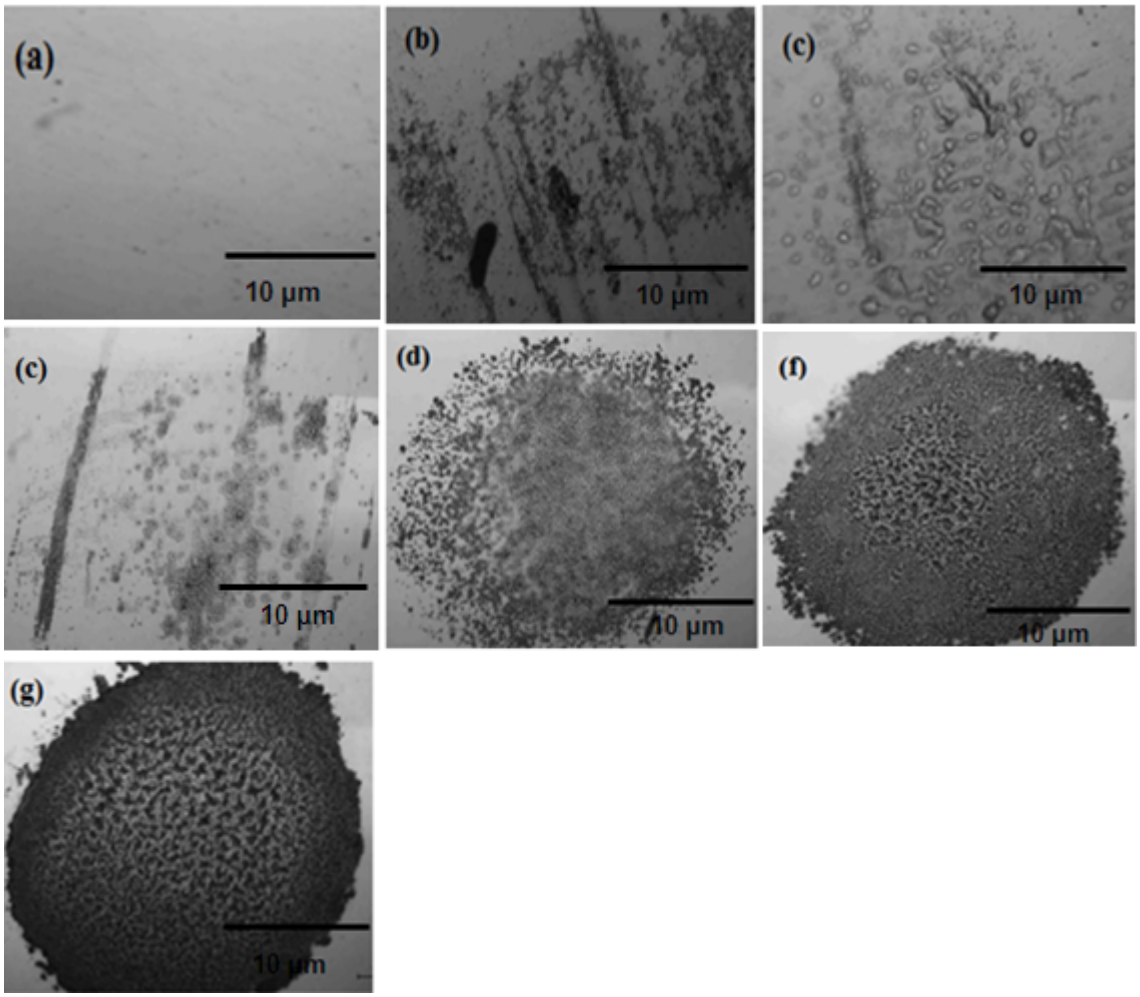

Fig. 5.5 Micromachining with 400 mJ pulse energy and 10 Hz frequency for (a) 300 pulses, (b) 400 pulses, (c) 500 pulses (d) 1000 pulses, (e) 2000 pulses, (f) 3000 pulses, and (g) 5000 pulses.

From Fig. 5.5 it was observed that crater formation starts at 400 pulses for the laser energy of 400 mJ. It was observed that, if pulse energy is increased from 200 mJ to 400 mJ, number of pulses required to create a crater reduces. Formation of craters was not observed at 300 pulses with 400 mJ pulse energy. With increasing the number of pulses more pronounced craters was observed. At 5000 pulses ring like pattern was observed at the edge of the crater. With increasing the laser energy significant increase in the diameter of crater was observed.

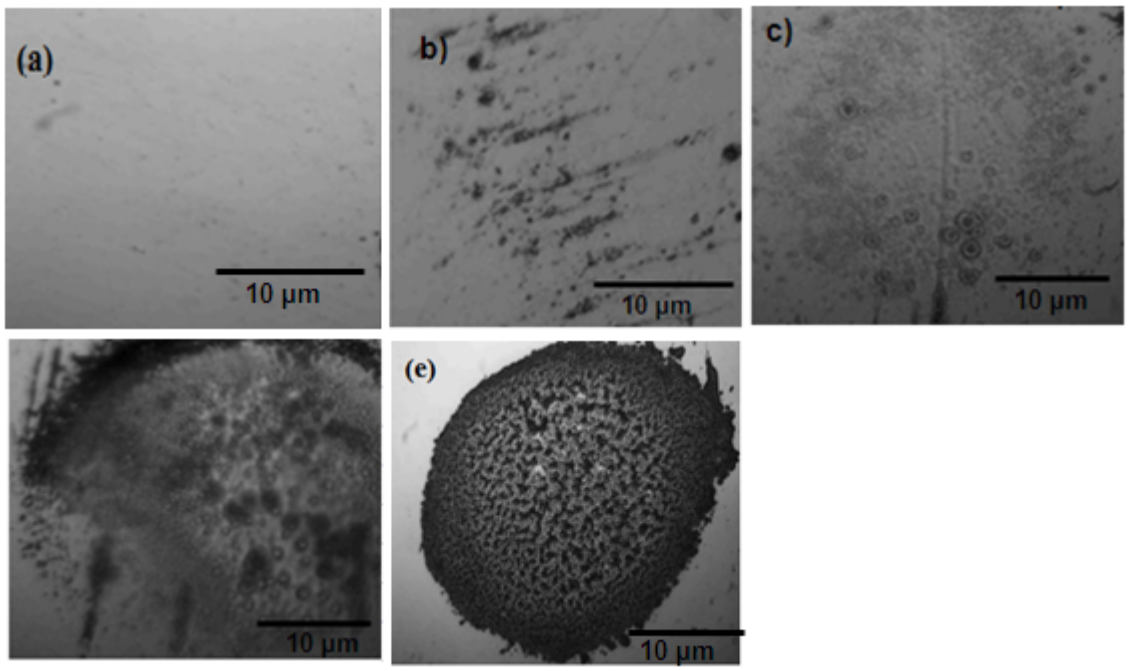

Fig. 5.6 Micromachining with 500 mJ pulse energy and 10 Hz frequency for (a) 200 pulses, (b) 300 pulses, (c) 1000 pulses (d) 2000 pulses, and (e) 5000 pulses.

From Fig. 5.6 it was observed that crater formation starts at 300 pulses for the laser energy of 500 mJ. Formation of craters was not observed at 200 pulses with 500 mJ pulse energy. It was finally observed that origin of crater formation starts for 1000 pulses at 200 mJ, for 500 pulses at 300 mJ, for 400 pulses at 400 mJ, and for 300 pulses at 500 mJ of laser energy.

Fig. 5.7 shows the variation of the laser affected diameter with pulse energy at constant number of pulses. With 2000 pulses and 5000 pulses significant increase in the laser affected diameter is observed with the increase of laser energy from 100 mJ to 500 mJ. Increase in Laser affected diameter with number of pulses was also observed at constant pulse energy. The laser afected diameter cannnot be calculated at other pulses because craters formed were not in circular shape as in 2000 and 5000 pulses.

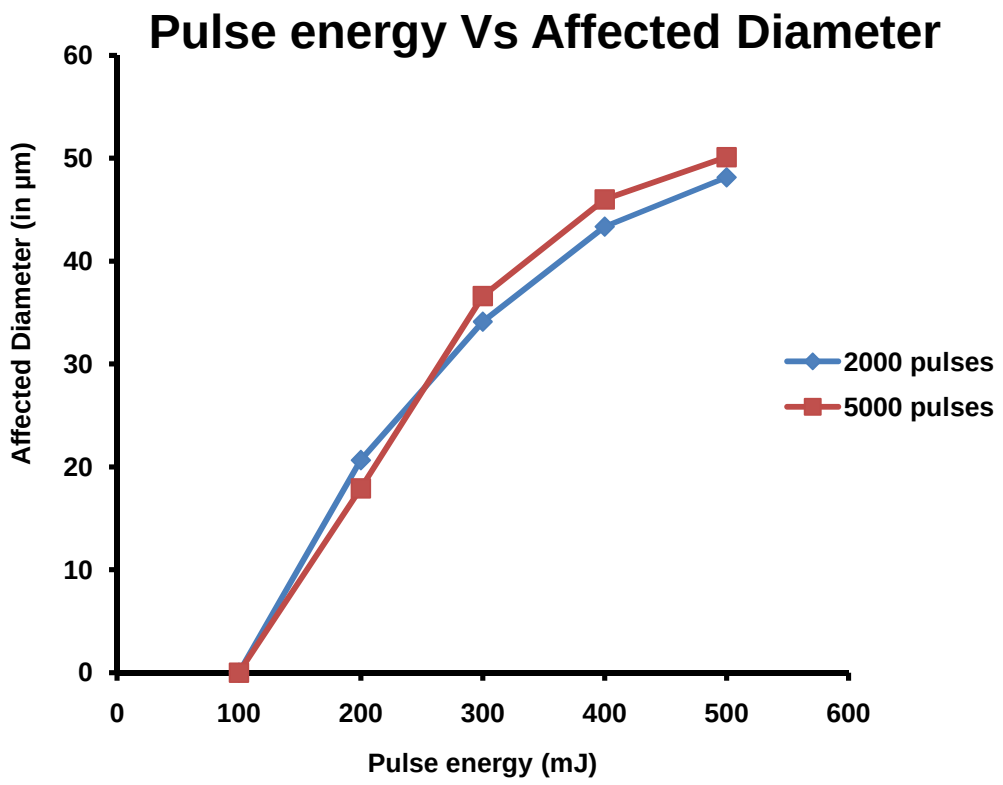

Fig. 5.7 Variation of Crater diameter with laser pulse energy for constant number of pulses.

5.1.1.2 Microstructural Change and Elemental Composition:

In order to investigate the surface features on the laser induced craters, scanning electron microscopy (SEM) was conducted. The elemental composition of constituents in SEM image was investigated by using energy dispersive spectroscopy (EDS).

5.1.1.2.1 SEM and EDS of Laser Induced Craters:

The shape, topography, and elemental composition of the craters created by the laser pulses are investigated as the function of laser energy. For the analysis, samples which are micromachined for 5000 pulses with 300 mJ pulse energy, 400 mJ pulse energy, and 500 mJ pulse energy respectively are taken into consideration.

Fig. 5.8, 5.9, and 5.10 shows the surface morphology of the craters formed by the excimer laser radition on the ribbon. The images depicts that the material was partially ejected by the vapor and plasma pressure and then re-deposited on the substrate. These types of features are visible in laser micromachining of amorphous material due to their disordered atomic scale structure, low thermal conductivity, and thermal ablation. In thermal ablation, the excitation energy is rapidly converted into heat resulting in temperature rise which causes for ablation of materials by surface vaporization [24]. Due to lower thermal diffusivity, thermal conductivity, and short pulses (25 ns), the less heat generated by the absorbed pulse energy is dissipated into the bulk of the material. Then, due to this more concentrated heating partial ejection of molten material from the craters by the vapor and plasma pressure was observed. Change in the concentration of the networks formed by the laser radiation on craters was also observed.

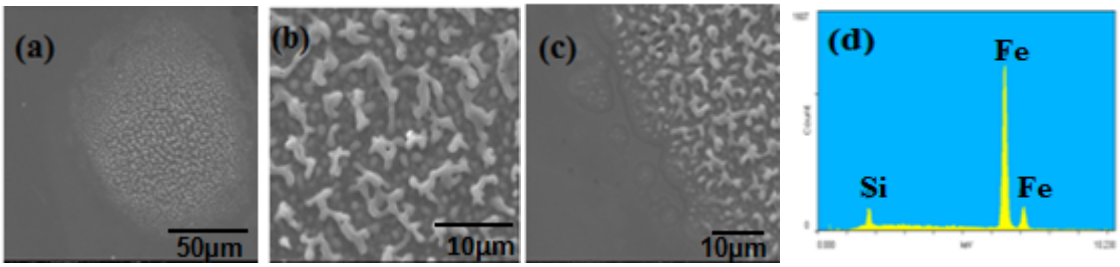

Fig. 5.8 SEM image and EDS pattern of laser induced craters formed at 300 mJ, 10 Hz, and 5000 pulses; (a) top view of crater, (b) central region, (c) edge of crater, and (d) EDS pattern.

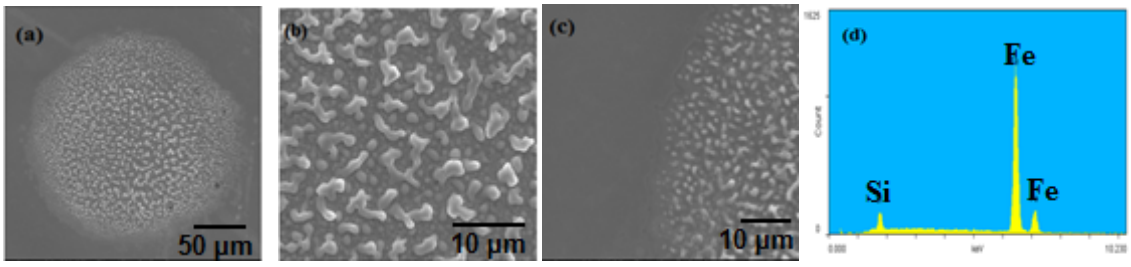

Fig. 5.9 SEM image and EDS pattern of laser induced craters formed at 400 mJ, 10 Hz, and 5000 pulses; (a) top view of crater, (b) central region, (c) edge of crater, and (d) EDS pattern.

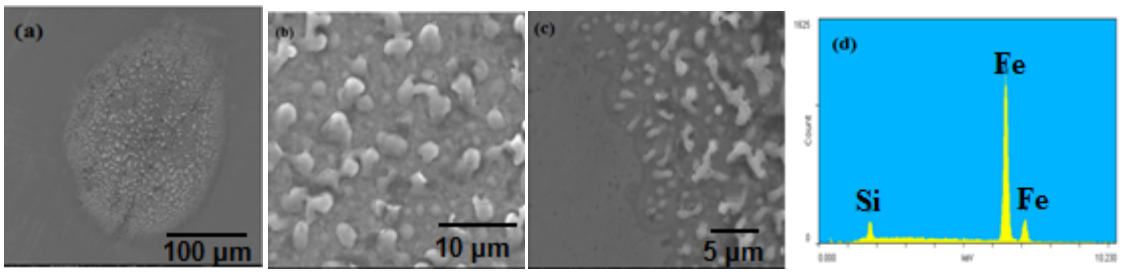

Fig. 5.10 SEM image and EDS pattern of laser induced craters formed at 400 mJ, 10 Hz, and 5000 pulses; a) top view of crater, (b) central region, (c) edge of crater, and (d) EDS pattern.

Fig. 5.8 (a), 5.9 (a), and 5.10 (a) shows the surface of the craters at 300 mJ, 400 mJ, and 500 mJ pulse energy respectively. It can the observed from the Fig. 5.8 (b), 5.9 (b), and 5.10 (b) that the network structure is more pronounced at the central region of the crater than at the edges of the craters. This is due to the Gaussian energy distribution of laser beam on the substrate which accounts for focusing of more energy in central region than at the edges. Concentration of networks was calculated by ImageJ software. From Fig. 5.8 (b), 5.9 (b), and 5.10 (b) it was observed that there is significant variation in the concentration of the networks at central region. Concentration of networks decreases due to the coalescing of the individual networks into larger networks with increasing energy. Due to this more networks concentration with smaller diameter were observed at 300 mJ pulse energy compared to the lesser networks with larger diameter were observed at 500 mJ pulse energy for the same number of 5000 laser pulses. Fig. 5.11 shows the variation in the networks concentration with laser energy at constant number of pulses calculated by ImageJ software.

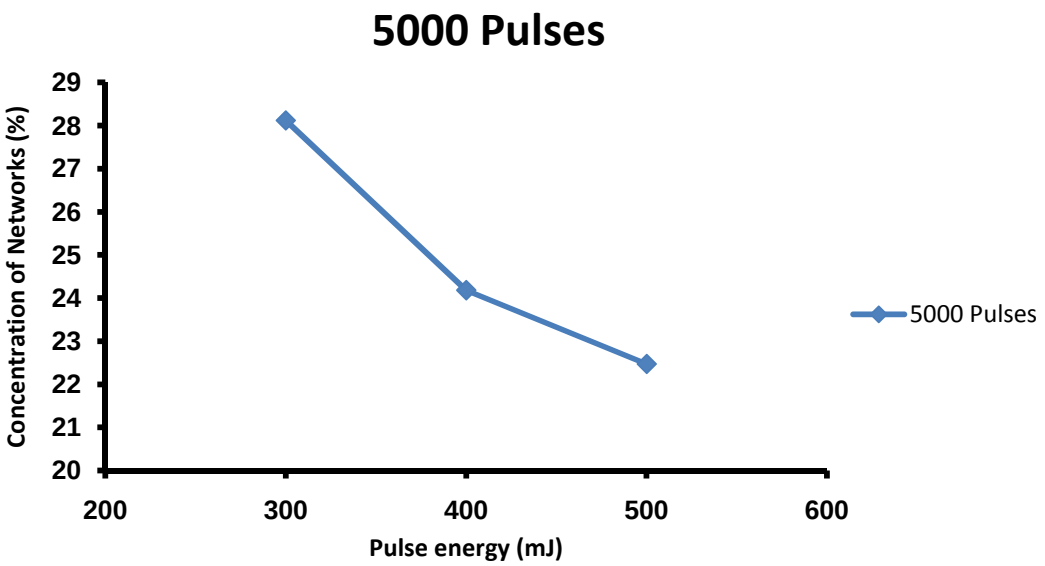

Fig. 5.11 Variation of networks concentration with pulse energy at constant number of pulses

The elemental composition in the craters still remains same as the composition of the as received ribbon which was observed from the 5.8 (d), 5.9 (d), 5.10 (d) shows iron and silicon in major proportions.

5.1.1.2.2 Multipoint EDS Analysis:

In order to have careful understanding of the change in elemental composition of the laser induced craters on the ribbon multipoint EDS analysis has been performed at different locations the specimen. Fig. 5.12 shows the EDS analysis on the crater at points 1, 2, 3, 4 and 5. At all the locations investigated show no change in elemental composition (by the presence of iron and silicon in major proportion).

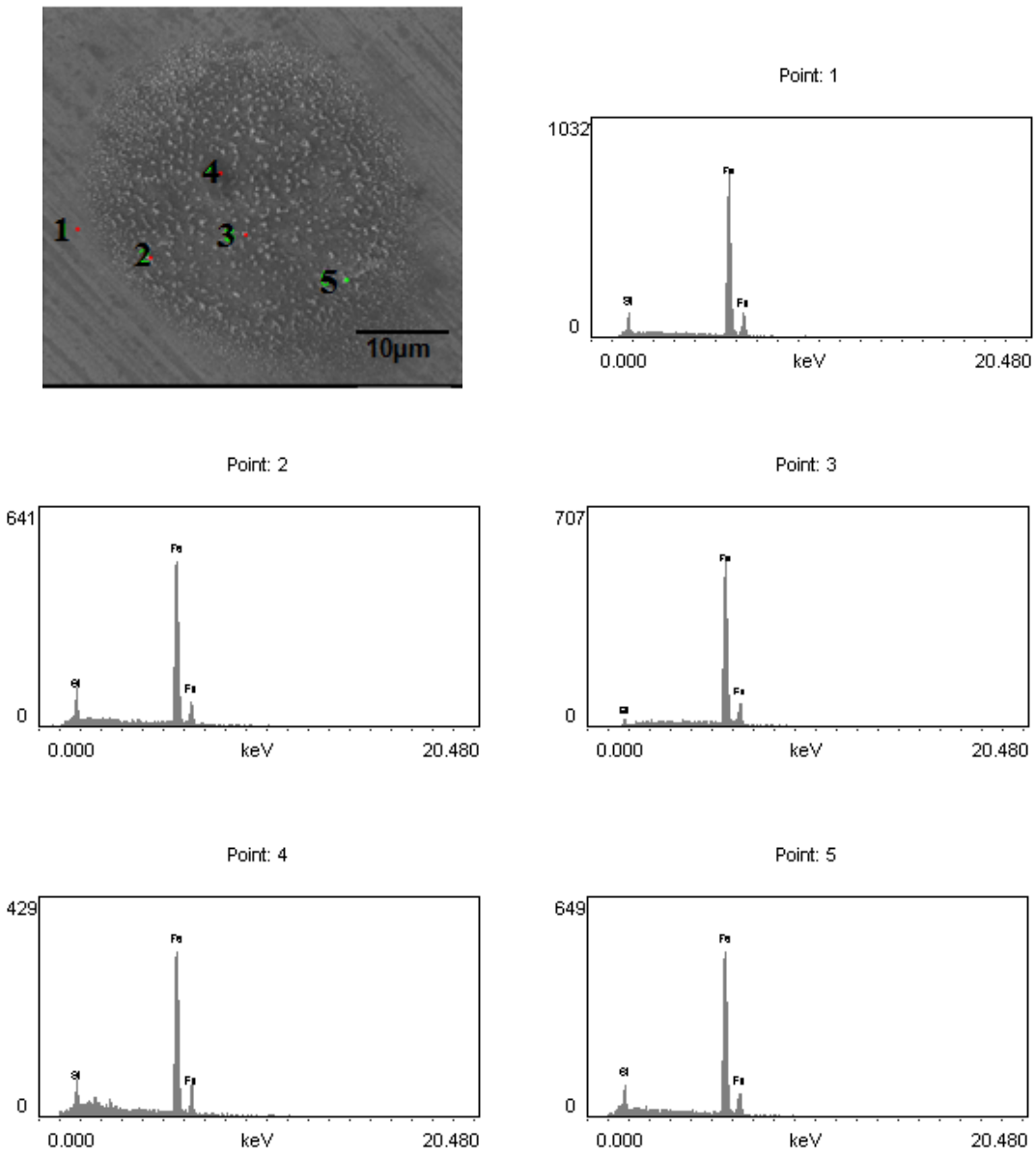

Fig. 5.12 Multi point EDS analysis at locations 1, 2, 3, 4 and 5 in the SEM image

5.1.1.3 Phase Analysis:

Fig. 5.13 shows X-ray diffraction pattern of the as received amorphous ribbon and laser induced craters. The as-received amorphous ribbon exhibits a characteristic broad halo with diffused intensity indicating fully amorphous structure. The phase observed by XRD analysis of the ribbon corresponds to the microstructural configuration observed earlier.

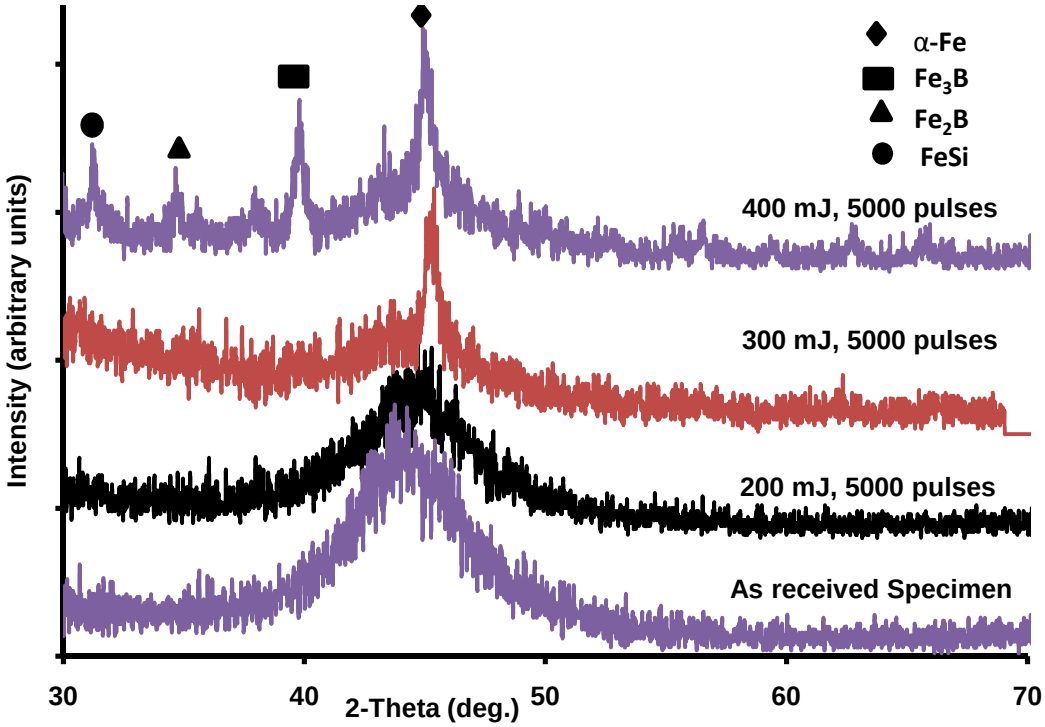

Fig. 5.13 XRD pattern for the as-received ribbon and laser treated ribbons with pulse energy of 200 mJ, 300 mJ and 400 mJ at constant number of 5000 pulses.

In order to understand whether crystallization of the laser induced craters occurs or not, ribbons were irradiated with excimer laser by removing the mask, so that we get larger area for XRD analysis (since laser induced craters shown in Fig. 5.1, 5.2, 5.3, 5.4, and 5.5) have smaller diameter than the beam diameter of XRD system which was 0.2 mm. Fig. 5.13 shows the XRD pattern of the laser treated areas produced at different pulse energies for the constant number of pulses by removing the mask. For the sample treated with 200 mJ of pulse energy and 5000 pulses characteristic broad halo peak with diffused intensity was observed, indicating fully amorphous structure, similar to untreated ribbons. For the sample treated with 300 mJ pulse energy and 5000 pulses sharp crystalline peaks superimposed with predominantly amorphous background was observed. These sharp crystalline peaks correspond to α-Fe indicating formation

of amorphous matrix embedded with crystalline phases. This suggests that irradiation of the amorphous ribbons at higher laser pulse energies resulted in the formation of crystalline phases embedded within the amorphous matrix. As the energy is increased to 400 mJ, sample further crystallizes and formation of more crystalline phases Fe_3B, Fe_2B, FeSi and α-Fe was observed from the phase analysis software.

In order to study type of crystallites nucleated in the matrix when crystallization of amorphous ribbon occurs, annealing of the amorphous ribbon was done at 520 ^oC for 5 min, 20 min, and 30 min duration respectively. Fig. 5.14 shows the XRD profile of the ribbons annealed for same temperature at different durations. Instead of retaining the amorphous structure at 520 ^oC for 20 min duration, the material undergoes crystallization and evolution of two crystalline phases α-Fe and Fe_3B was observed from the sharp crystalline peaks superimposed on amorphous background. When we increase the duration of the annealing time to 30 min, relative volume fractions of these phases varied (as is evident from the difference in peak intensities).

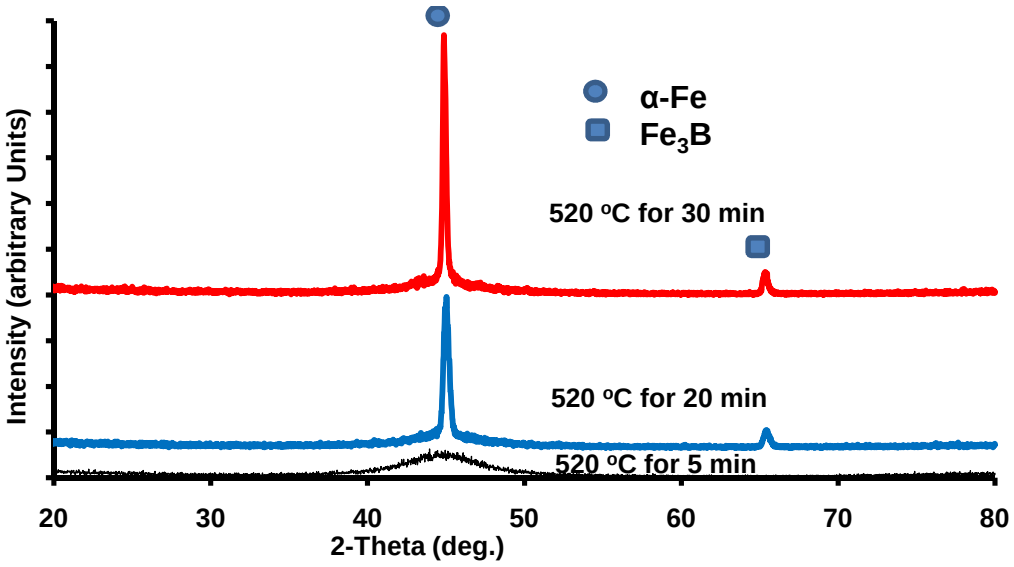

Fig. 5.14 XRD pattern of the ribbon annealed at 520 ^oC for duration of 5 min, 20 min, and 30 min.

Formation of crystalline phases in amorphous material at higher pulse energy may be due to (a) melting of the surface layer followed by rapid resolidification, (b) thermal ablation, and (c) laser heating above crystallization temperature. As explained above thermal ablation of these lesser thermal conductive materials results in more confinement of laser energy in the smaller area with lesser heat dissipation into bulk of material. It was generally accepted that laser melted amorphous material will solidify into glassy structure without crystallization due to higher cooling rates in the order of 10^5 K/s during solidification of laser melted materials. But, most of the alloys don't exhibit this behavior due to complex solidification process. Notwithstanding the high cooling rates, the underlying solid material provides the nucleation sites for the growth of crystalline phase during solidification of laser surface melted material. The crystallization of many amorphous materials upon laser melting is reported in the literature [89-91]. Hence, thermal effects during surface ablation, laser melting, laser heating above crystallization temperature and rapid resolidification may be the possible reasons for the crystallization which can be observed from the SEM image from Fig. 5.15.

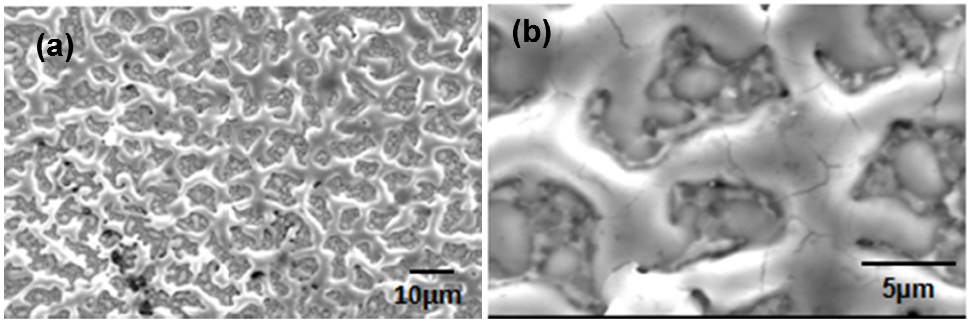

Fig. 5.15 SEM image showing the laser melted regions on the surface of ribbon treated with 300 mJ of pulse energy and 5000 pulses.

The crystallization of Fe-B-Si amorphous alloy with similar compositions often occurs in following sequence [92].

Amorphous [T<500 °C] → Amorphous + α-Fe(Si) [510 °C<T<550 °C] → Fe_2B [T>550 °C]

As shown earlier in Fig. 5.14, formation of only α-Fe crystalline phase during annealing at 520 ^{o}C which confirms the results obtained are in good agreement with literature [92]. Formation of α-Fe (intermediate crystalline product since it is embedded in amorphous matrix) during treatment with 300 mJ pulse energy indicates the partial crystallization. Such intermediate products can be formed during partial crystallization in the range of 500-550 ^{o}C which is observed from XRD pattern of annealed samples and also suggest that only surface heating occurs at 300 mJ pulse energy without any surface melting. But, during laser treatment with 400 mJ resulted in nucleation of Fe_3B, Fe_2B, FeSi, and α-Fe crystalline phases which might be because of laser surface melting. Hence at 400 mJ of pulse energy material is fully crystallized which may be due to both surface melting and surface heating as it forms final crystallization products like Fe_3B, Fe_2B. The inference is again supported by the microscopic observation of surface indicating the surface heating in the Fig. 5.16.

5.1.2. Micromachining response of $Fe_{48}Cr_{15}Mo_{14}Y_2C_{15}B_6$bulk Metallic Glass:

Fe-based bulk metallic glass of composition $Fe_{48}Cr_{15}Mo_{14}Y_2C_{15}B_6$ having thickness of 3.86 mm is used in these studies. The substrate is mounted on the translation stage. The amorphous material is exposed to different number of pulses with a constant frequency of 40 Hz and pulse energy of 400 mJ. Fig. 5.16, Fig. 5.17 shows the 3D- top view, 3D- front view of the circular crater in the sample obtained by using the MicroXam laser interference microscope respectively. The onset of crater formation takes place at 300 pulses for 400 mJ of pulse energy. The laser pulses in the number of 300 pulses is the threshold value observed; below which there is not any effect of laser on the material was observed. As we increase the number of pulses the more material removal takes place from the crater. It can be observed from the 3D profile that the surface is quite uneven due to its porosity. The depressions and the raised portions at the centre corresponds the crater formation at different number of pulses. As the crater depth exceeds the limit of the instrument, it is impossible to get the depth of the crater which is observed in the 3D

profile where we see the clear circular crater feature with black areas. More black spots are seen on the untreated surface due to porosity of the sample where depth is out of range for the microcope to capture it. It was observed from the raised projections in the 3D profiles that the material is redeposited back into the molten pool. As the number of pulses is increased the concentration of the projections decreased due to more material removal at these parameters in comparison to the laser redeposited material. Starting from 3200 pulses more material removal takes place and it increases significantly upto 24000 pulses where we see complete hole with out any raised portions in the centre of the crater.

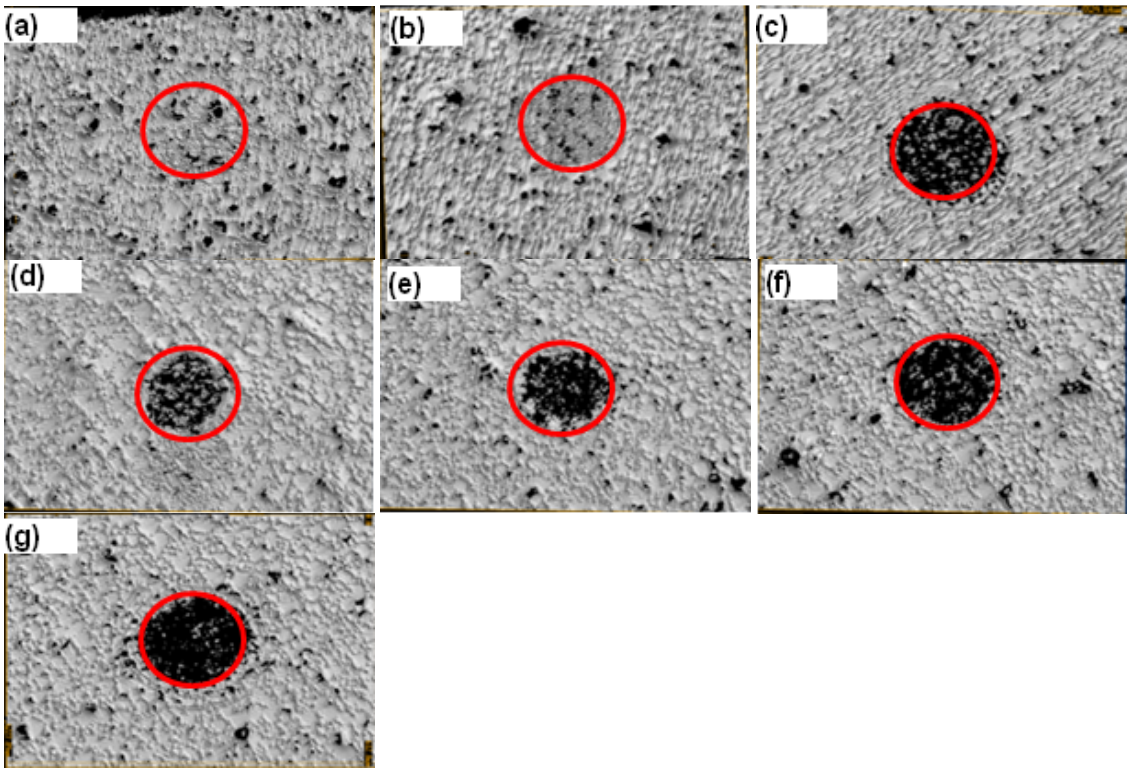

Fig. 5.16 3D-Mapping showing the top view of crater for 400 mJ energy and 40 Hz frequency (a) 300 pulses, (b) 400 pulses, (c) 1000 pulses, (d) 3200 pulses, (e) 6000 pulses, (f) 12000 pulses, and (g) 24000 pulses.

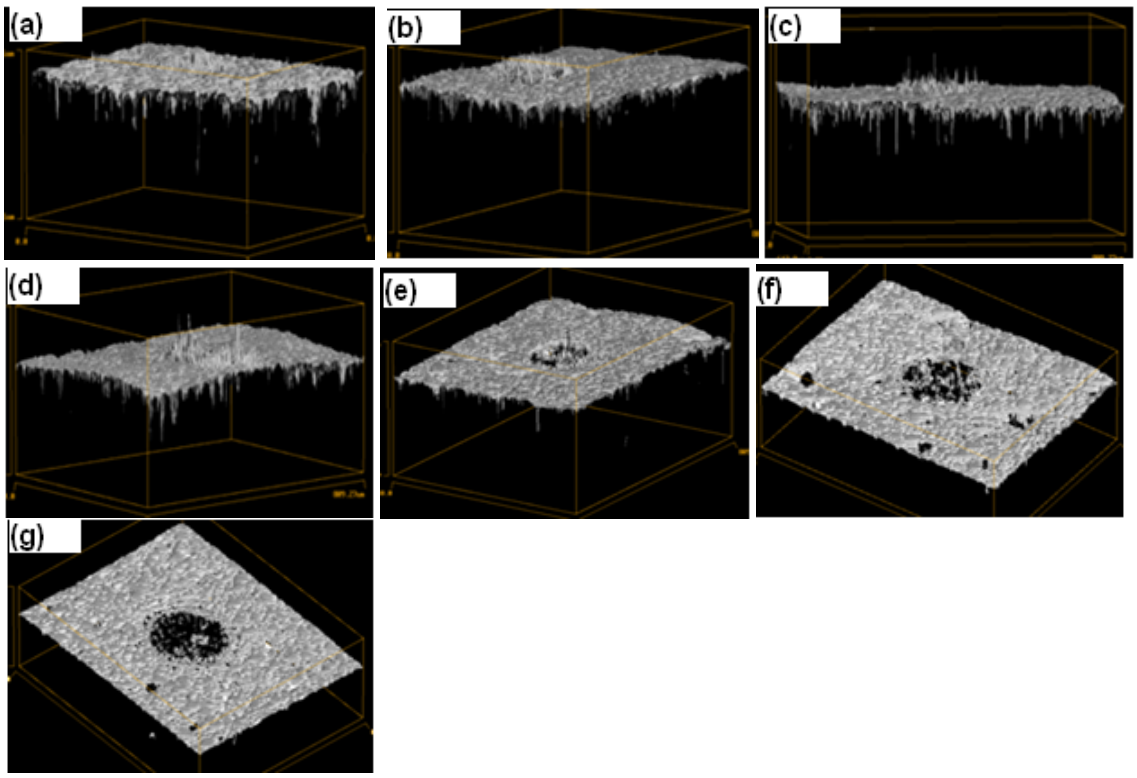

Fig. 5.17 3D Mapping showing the front view of crater for 400 mJ energy and 40 Hz frequency (a) 300 pulses, (b) 400 pulses, (c) 1000 pulses, (d) 3200 pulses, (e) 6000 pulses, (f) 12000 pulses, and (g) 24000 pulses.

At higher number of pulses it is impossible to measure the depth of the crater because it is out of range for the MicroXAM microscope. Ring like structure is observed on the periphery of the crater for all the samples treated with various number of pulses due to redeposited material and the lower energy distribution at the edge of the crater than at the center.

5.1.2.1 Microstructural Change and Phase Analysis of the Laser treated areas:

Fig. 5.18 shows the microstructure of the $Fe_{48}Cr_{15}Mo_{14}Y_2C_{15}B_6$ bulk metallic glass as received sample. It is featureless surface resembling amorphous nature of the sample alloy.

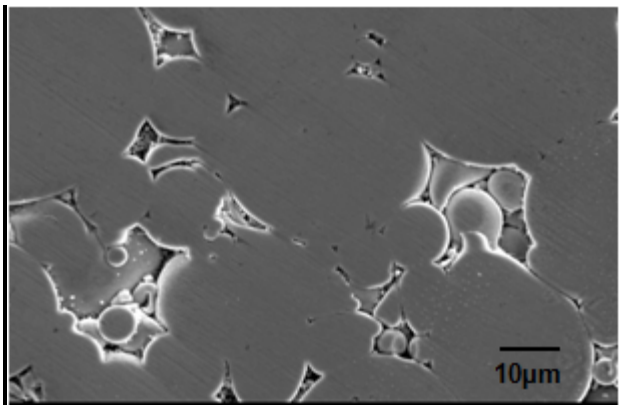

Fig. 5.18 SEM image showing the microstructure of the as received bulk metallic glass specimen.

It was observed from the microstructure that the material is porous which is in good agreement with the calculated relative density of 92.4%. The surface microstructure is composed of bigger particles without any grains or grain boundaries

Fig. 5.19 (a), (b), (c), and (d) represents the low magnification SEM images of the crater produced with 300 pulses, 400 pulses, 1000 pulses, 3200 pulses respectively. Ring like features are observed in the periphery which corresponds to the observation from the MicroXam microscope. As we increase the pulses above 300 breakage of the bond between the particles in the amorphous matrix occurs and partition of particles results with increasing pulses. With 1000 pulses and 3200 pulses, redeposition of the particles occurs from the molten pool is seen.

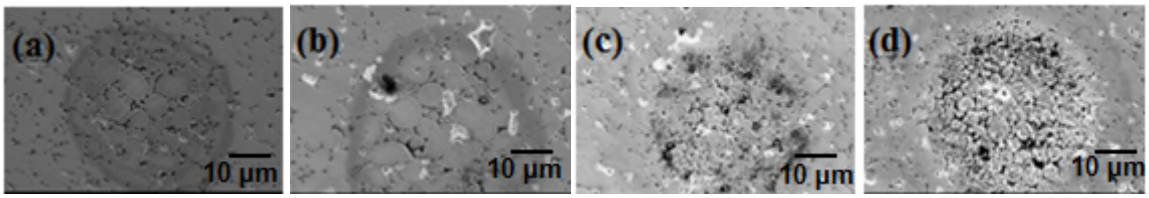

Fig. 5.19 SEM image showing the top view of the crater at 400 mJ energy and 40 Hz frequency (a) 300 pulses, (b) 400 pulses, (c) 1000 pulses, and (d) 3200 pulses.

Microstructure of the material having significant porosity is shown in Fig 5.20 (a). Fig 5.20 (b) gives the higher magnification image of as received sample in Fig 5.20 (a) showing the individual particle and further analysis is focused on the microstructural changes in the single particle after exposing the material to 2500 pulses, 5000 pulses, 12000 pulses, and 24000 pulses at a pulse energy of 400 mJ and frequency of 40 Hz.

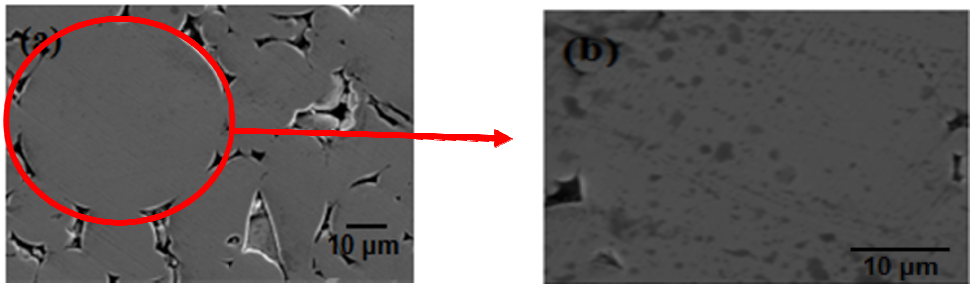

Fig. 5.20 (a) SEM of as received bulk metallic glass specimen showing cluster of particles and (b) higher magnification of (a) showing individual particle.

As described earlier, in order to study the phase evolution in the amorphous materials, X-ray diffraction analysis is performed. As the beam diameter of the XRD machine is larger than the diameter of crater formed, XRD patterns shown from these craters would not be able to determine the phase in crater. In order to determine phase evolution, amorphous material is treated with laser by removing the mask so that we get larger area for the X-ray diffraction analysis. When the mask is removed square type pattern is observed on the substrate due to the square beam profile of the laser beam.

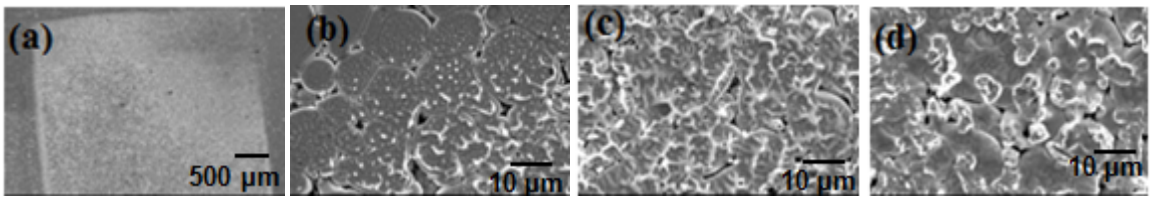

Fig. 5.21 (a) Square pattern (crater) on substrate, (b) edge of the crater, (c) network structure in the crater, and (d) broken networks in the crater.

Fig. 5.21 (a) shows the square pattern on the substrate as it is treated without mask since the beam coming out of the laser beam is composed of square profile. Fig. 5.21 (b) shows the surface at the edge of the square, where networks were seen in the treated area than at the untreated area. Fig. 5.21 (c) shows the higher magnification image of the square pattern. It was observed network like structure is composed on the each particle due to laser treatment. Fig. 5.21 (d) shows the microstructure of the sample at different locations after wiping the laser treated area with cloth. It was observed from these figures that these networks are broken and are randomly oriented unlikely with the images shown above.

Fig. 5.22, 5.23, 5.24, and 5.25 shows the higher magnification images of the particles which shows that networks are oriented radially outwards to the circular particles. The concentration of networks is lower at 2500 pulses whereas the concentration of networks increases with increase in number to 5000 pulses. Material removal takes place at the centre of the particles and this material which was removed is radially oriented as network structure on the periphery of the circular particles. Initiation of cracks in the particle was seen at 5000 pulses. It was observed that there is less material removal, as the material which is removed is redeposited back as network structure on the substrate material. In the Fig. 5.23 (b) it was observed that these networks are broken when we wipe the laser treated surface with cloth. This results in the significant surface roughness of the samples after laser treatment. At 12000 pulses cracks propagate significantly in the particle and roughness of the sample significantly increases which is seen in Fig. 5.24. At 24000 pulses these propagated cracks results in significant partition of particle which can be seen in Fig. 5.25 (a). Fig. 5.25 (b) shows the breakage of individual particle into large number of small particles.

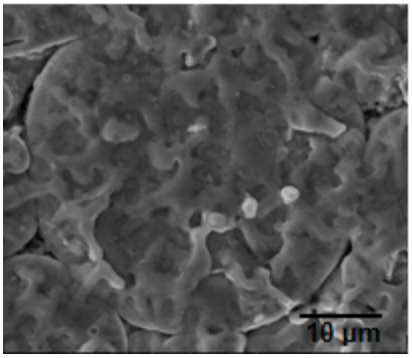

Fig. 5.22 SEM image of bulk metallic glass specimen treated with 2500 pulses and 400 mJ showing individual particle.

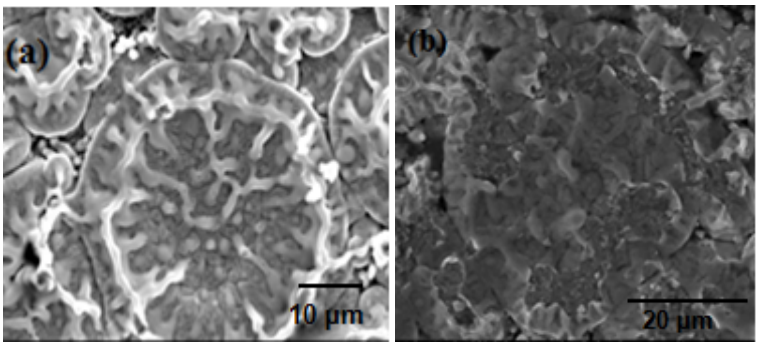

Fig. 5.23 SEM image of bulk metallic glass specimen treated with 5000 pulses and 400 mJ showing individual particle with (a) with network structure (b) without network structure.

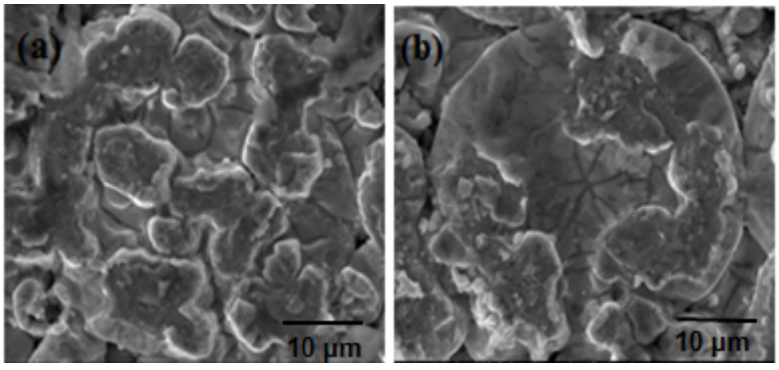

Fig. 5.24 SEM image of as bulk metallic glass specimen treated with 12000 pulses and 400 mJ showing individual particle at different locations.

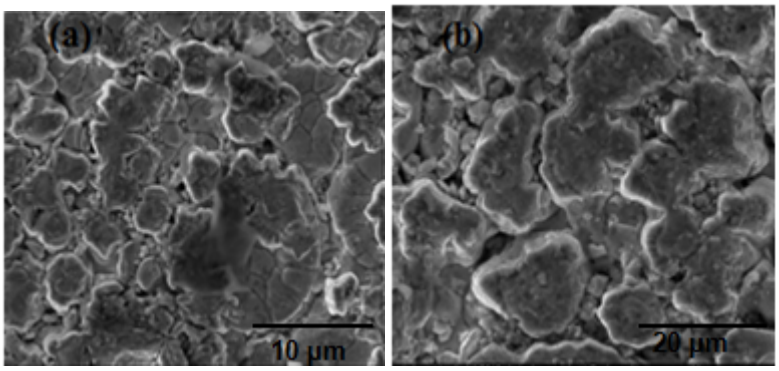

Fig. 5.25 SEM image of bulk metallic glass specimen treated with 24000 pulses and 400 mJ showing individual particle.

Fig. 5.26 shows the surface roughness of these laser treated areas measured with MicroXam microscope. It is observed that roughness of the specimen surface significantly increases at 12000 pulses correlating with the microstructural image showing significant propagation of the initiated cracks at 5000 pulses. More pronounced networks are also the reason for higher surface roughness. At 24000 pulses, surface roughness is lower than the previous case because of the disappearance of all the networks and as the microstructure is composed of individual small particles bonding together. All the surface roughness values obtained corresponds to the microstructural images shown above.

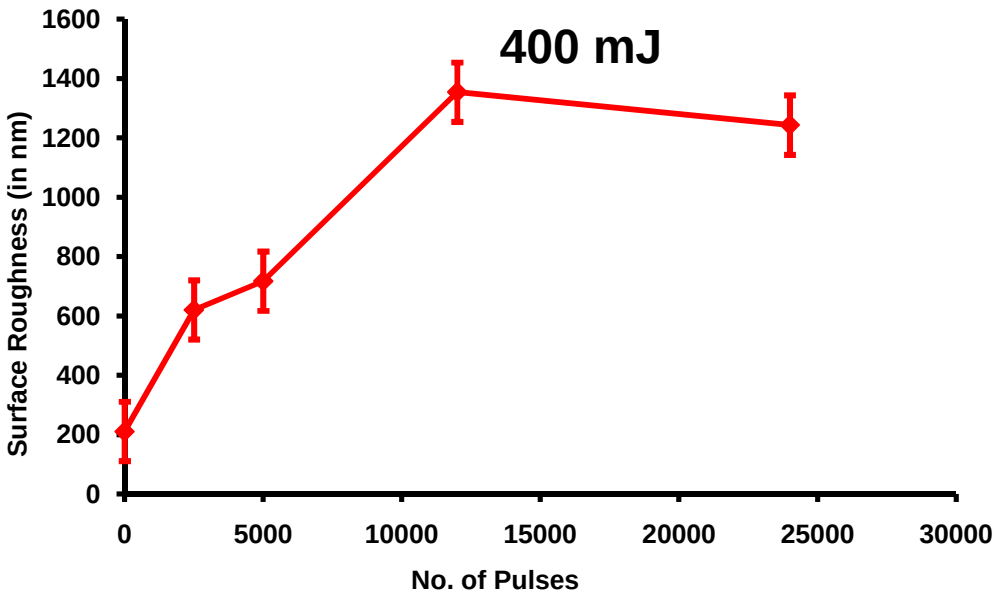

Fig. 5.26 Variation in surface roughness of the crater with number of pulses at constant energy of 400 mJ.

Fig. 5.27 shows the XRD pattern of the as received and laser treated area exposed to 400 mJ of pulse energy with increasing the pulses from 2500, 5000, 12000 and 24000 pulses respectively. The XRD pattern of the as received sample shows a broad diffuse peak, typical of the lack of long range order exhibited by metallic glass. Specimens exposed to 2500 pulses exhibited significant crystallization. The diffuse peak seen in as received sample was not discernable, and sharp crystalline peaks were present in XRD patterns. The crystalline peaks were observed as $(Fe,Cr)_{23}C_7$ from the phase analysis of the patterns. Hence it was observed that the material under goes crystallization with significant microstructural damage when the micromachining of the material is conducted with excimer laser.

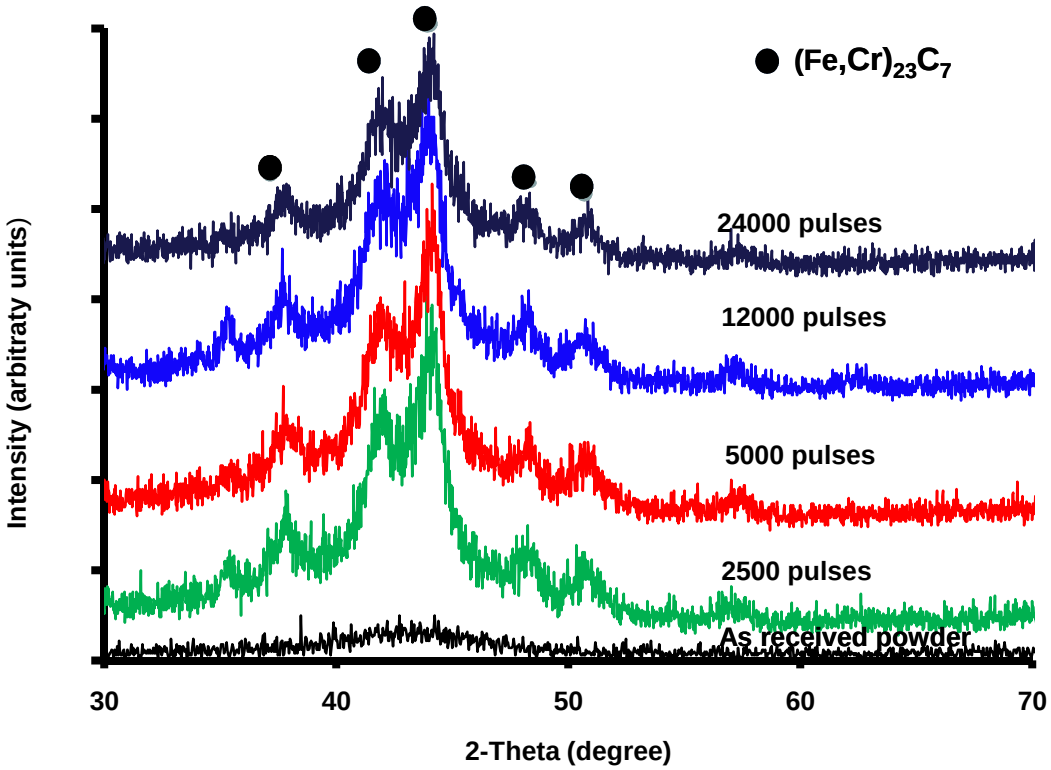

Fig. 5.27 XRD pattern of the as received and laser treated specimen.

5.1.2.2 EDS of the as received sample and laser treated area (with and without networks):

In order to study the change in chemical composition in the specimens, EDS was performed on the as received specimens and specimens treated with laser energy of 400 mJ and 5000 pulses. In order to perform the EDS, higher magnification SEM image of individual particle in as received specimen and areas treated with laser (with and without networks) were considered. Fig. 5.28, 5.29, and 5.30 shows the elemental dot mapping of the fully amorphous sample, laser treated areas with networks, and without networks respectively. These figures demonstrate the distribution of individual elements of Fe, Cr, and Mo in the materials. Brighter concentration depicts higher concentration of the element at the location.

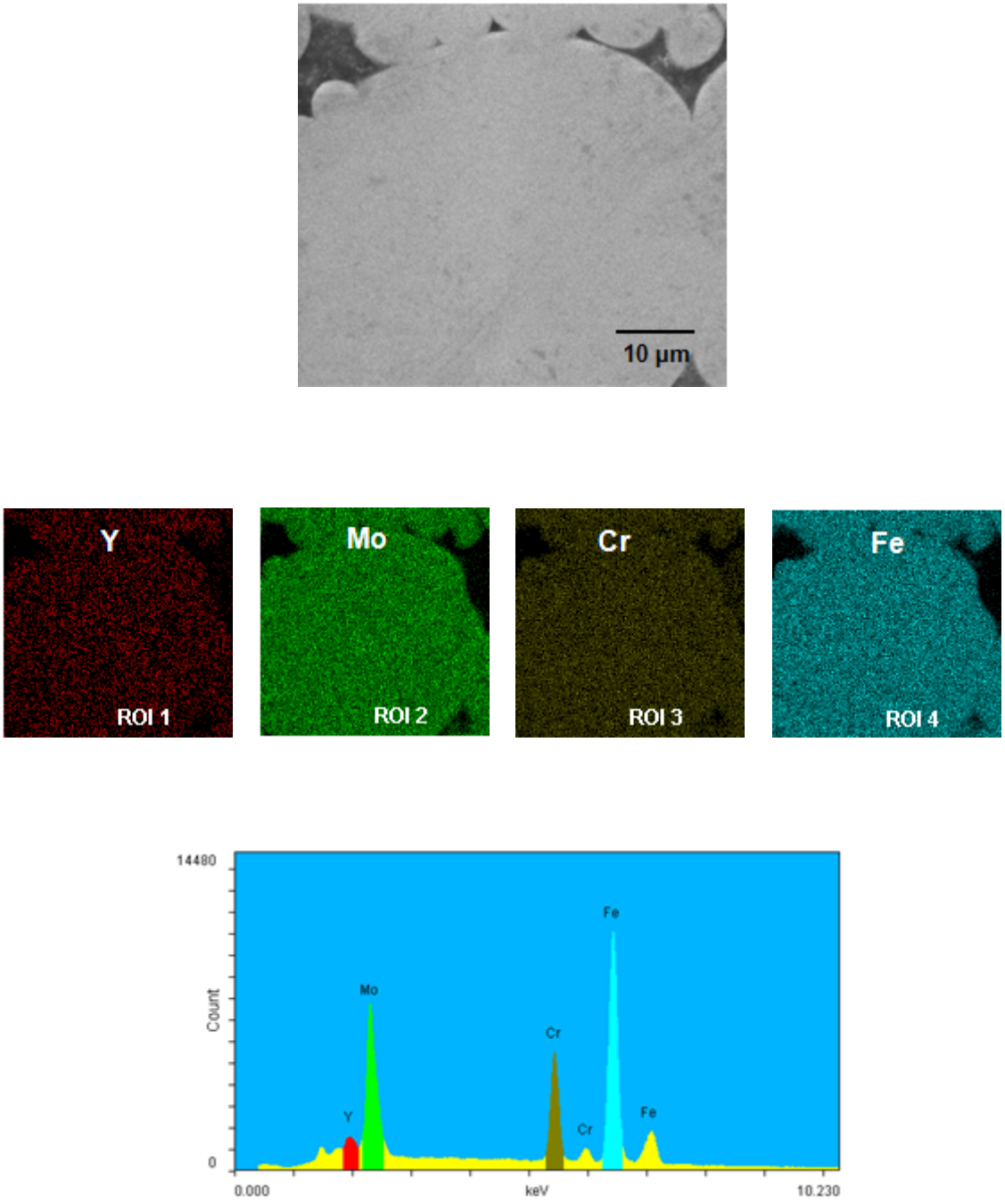

Fig. 5.28 EDS elemental dot mapping for the as-received bulk metallic glass specimen on individual particle.

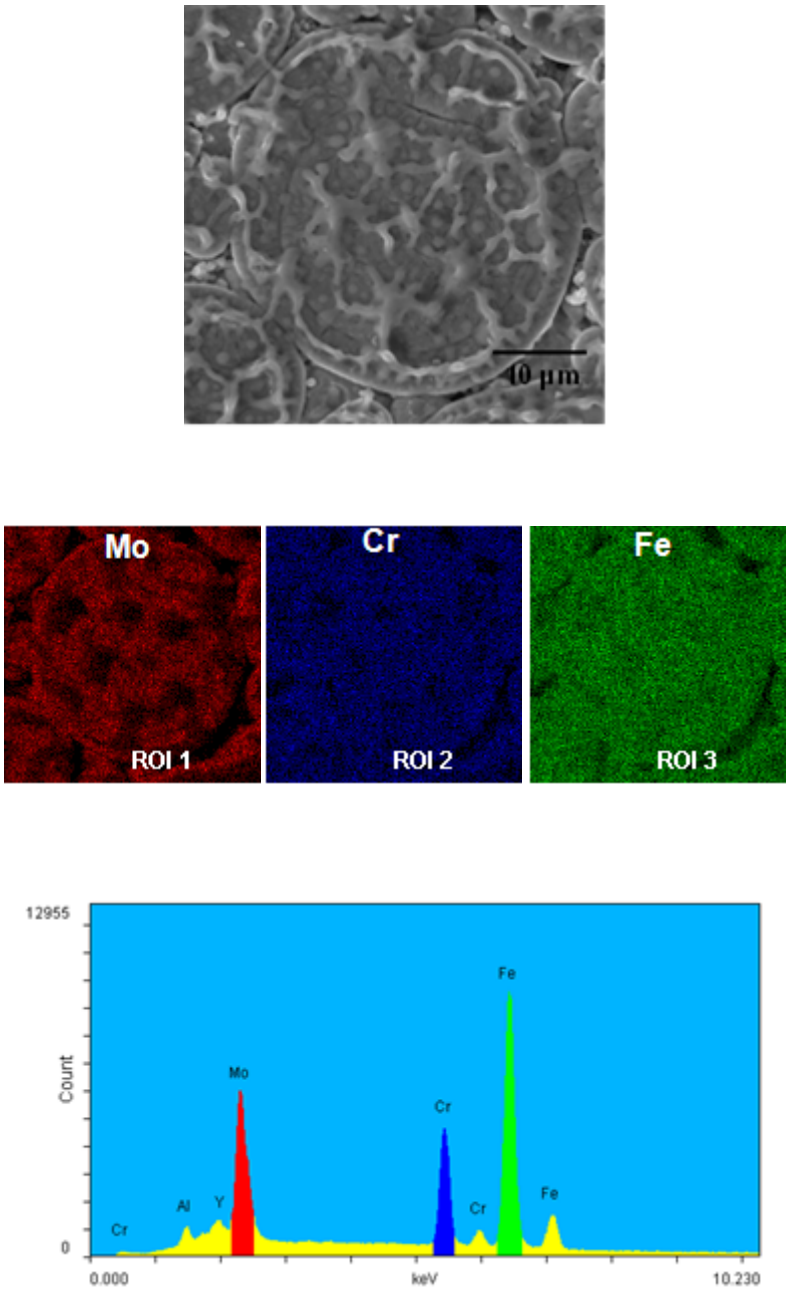

Fig. 5.29 EDS elemental dot mapping for the bulk metallic glass specimen with networks on individual particle.

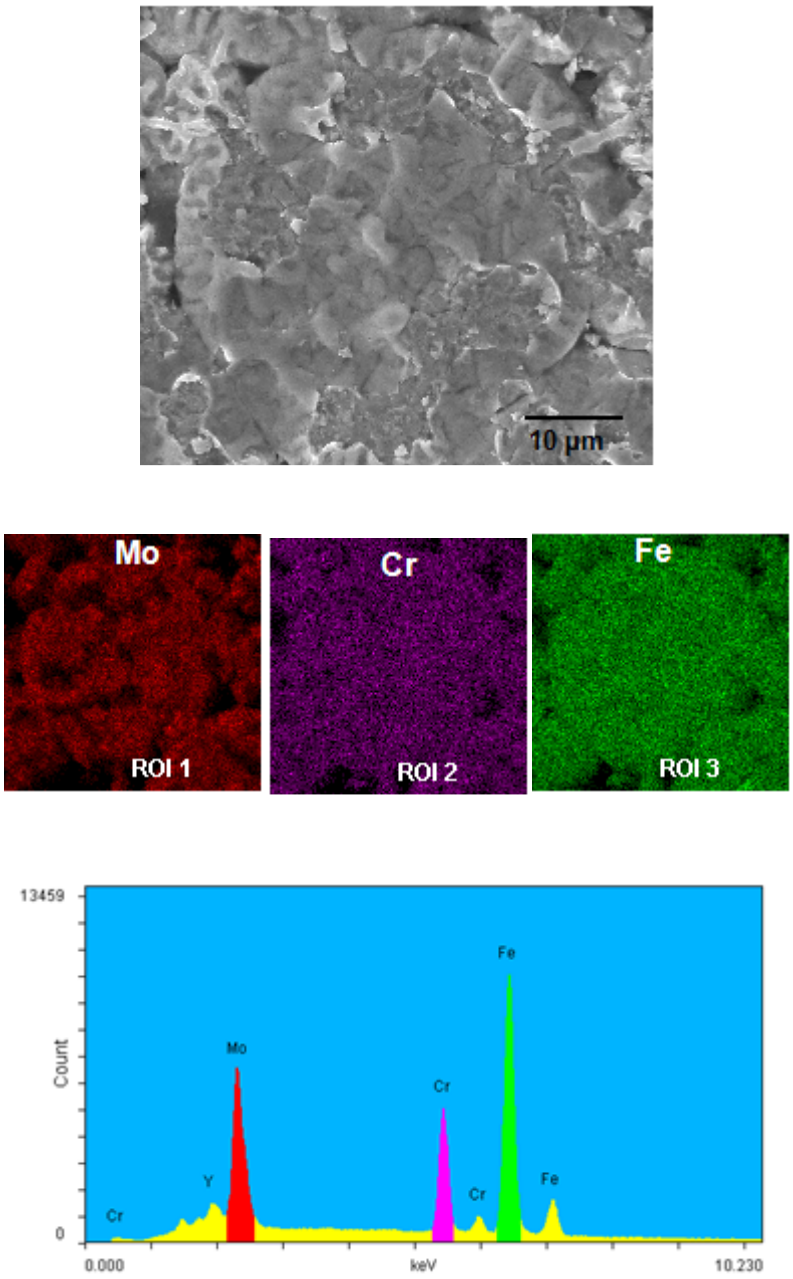

Fig. 5.30 EDS elemental dot mapping of the bulk metallic glass specimen without networks on individual particle.

Fig. 5.28 shows the concentration of Fe, Mo, and Cr in higher quantities due to the brighter concentration of respective color. In Fig. 5.29 shows the mapping for the individual particle with networks for the elements Fe, Mo, and Cr, it was observed that the concentration of

Mo in the networks is significantly lower than that compared with fully amorphous as received sample, from more dark areas seen in the mapping for the element Mo (red color). Hence, it is concluded that there is depletion of Mo element in these networks with respect to surrounding matrix. Even some darker areas are seen in the Cr elemental mapping but not as much as compared to the Mo element. But concentration of Fe element remains same in all the areas as there is not any visible dark area in the networks or in surrounding matrix. The reason for the depletion of Mo in the darker areas is because of the formation of crystallites $(Fe,Cr)_{23}C_7$ which was observed in the XRD pattern.

In order to confirm the results shown above, EDS elemental dot mapping has been performed on the individual particle without networks which is observed after wiping the sample with cloth and is shown in Fig. 5.30. In the mapping for Mo element there were not as much darker areas like in the sample with networks which confirms that these networks are depleted with Molybdenum element due to formation of $(Fe,Cr)_{23}C_7$ in those networks. As EDS is performed on the area without networks, Mo is not depleted as much as in the sample with networks. But, still some darker areas are seen in the Mo element mapping because of very small concentration of networks. It validates that these networks which were formed were depleted of Mo element. In order to further validate the results obtained above Quantitative analysis of these three elements Fe, Mo, and Cr in terms of atomic percentage has to be investigated in the network region.

5.1.2.3 Quantitative analysis in terms of elemental composition for the area treated with laser:

An EDS line scan through the network was performed in order to understand the change in the elemental composition in the networks. Length of 9.03 µm (201 points) is considered for our analysis. Fig. 5.31 shows the line scan of length 9.03 µm on the uphill network with

surrounding matrix in the sample. Fig. 5.32 shows the atomic percentage of each element Fe, Mo, and Cr respectively in the line scan. Fig. 5.32 shows the higher percentage of Fe and Cr elements in the network length compared with the surrounding matrix whereas the percentage of Mo element in the network length is lower than with surrounding matrix. This lower percentage of Mo in the network is due to the enrichment of Mo in the surrounding matrix which was observed in Fig. 5.32 for line scan data of Mo and higher percentage of Fe and Cr elements in network area is due to depletion of Fe and Cr elements in the surrounding matrix observed in line scan data for Fe and Cr elements respectively. This analysis further confirms the formation of only $(Fe,Cr)_{23}C_7$ crystalline phase in the network area which is proven by the enrichment of only Fe, Cr elements in the network area and depletion of Mo in the network.

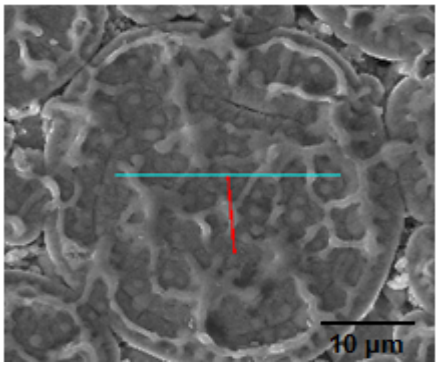

Fig. 5.31 EDS line scan showing the variation in atomic percentage of each element Fe, Cr, Mo.

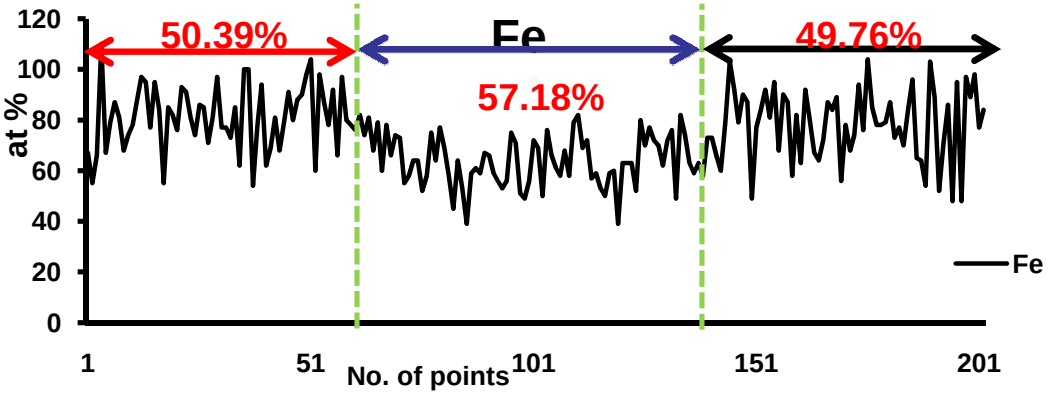

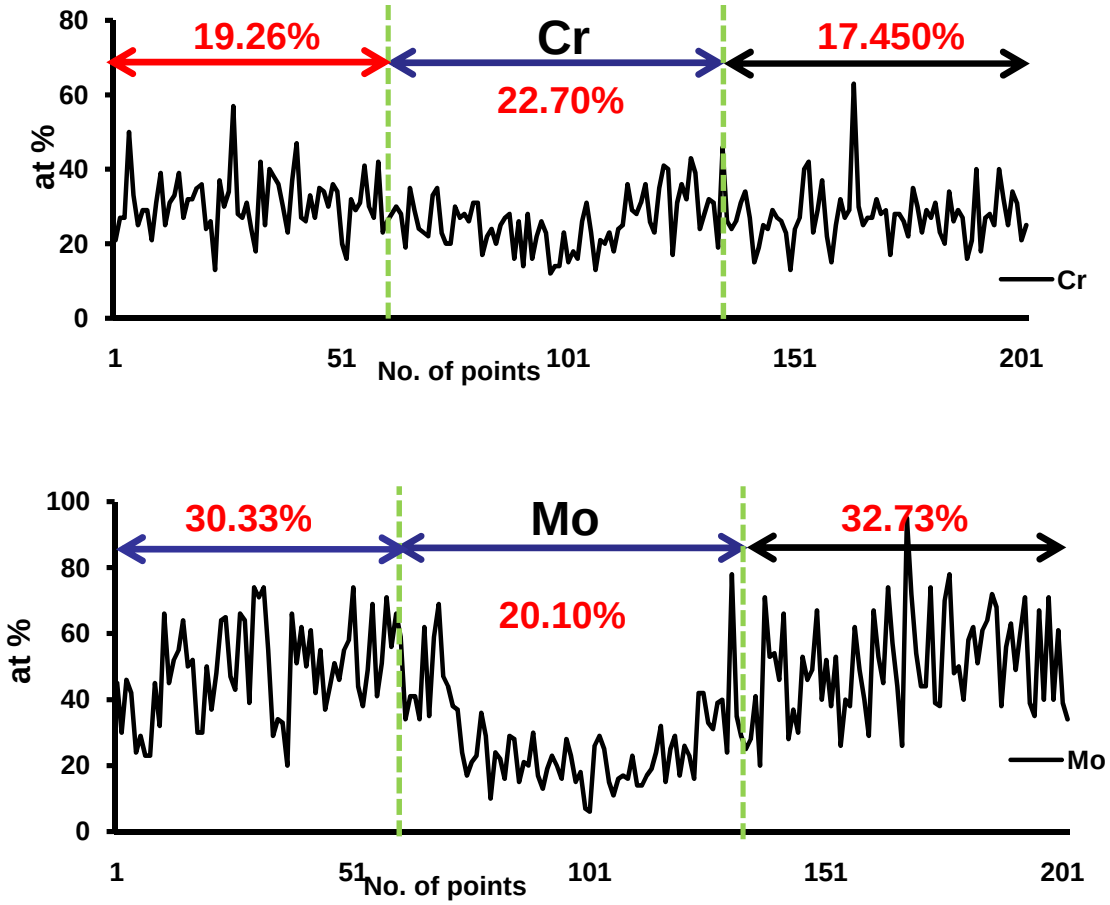

Fig. 5.32 Variation in relative atomic percentage of Fe, Cr, and Mo at the network and surrounding matrix.

5.2 Corrosion Behavior of Fe-Si-B Metallic Glass Ribbon:

Iron-based amorphous alloy ribbon of the composition $Fe_{85\text{-}95\%}Si_{5\text{-}10\%}B_{1\text{-}5\%}$ is used in this study for the investigation of its electrochemical behavior.

5.2.1 Microstructural Change and Elemental Composition:

Fig. 5.33(b) shows the higher magnification image of the corrosion tested ribbon. It was observed that there is significant change in microstructure of the material after corrosion testing. Micro-cracks were observed in the material after corrosion testing due to active reaction before

passivation which is principally attributed to the crystals, oxides, pores and microcracks distributed in the matrix. These structural defects usually become the initial corrosion sites prior to the uniform amorphous matrix, leading to the rapid increase of corrosion current density at the early stage of anodic polarization, until the equilibrium of active dissolution and passivation established which is shown in Tafel plot.

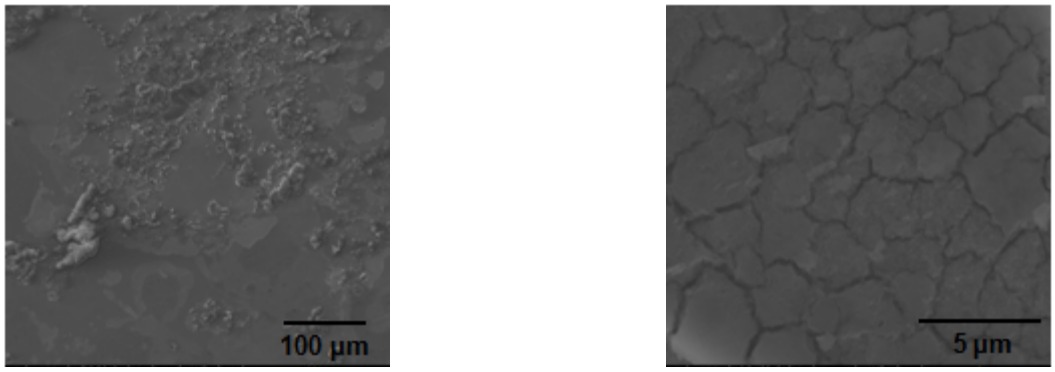

(a) (b)

Fig. 5.33 (a) Lower magnification SEM image of the corrosion tested ribbon, and (b) higher magnification SEM image of the corrosion tested ribbon.

Fig. 5.34 and Fig. 5.35 shows the EDS analysis on the microstructure of the ribbon before and after corrosion testing. The change in the chemical composition of the Fe and Si after corrosion testing may be due to surface oxidation of the ribbon after corrosion testing. Significant reduction in the silicon atomic percentage (from 10% to 2%) was observed in the ribbon after corrosion testing which may be attributed to the formation of silicates during surface oxidation after corrosion testing.

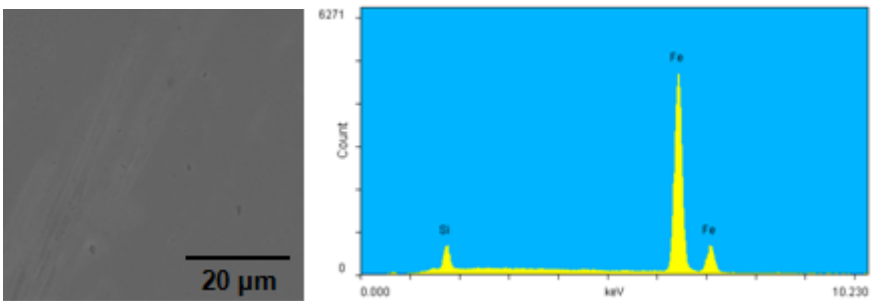

Elements:	WT%	AT%	K_A	K_F	K_Z	Intensity	P/bkg
SiK	5.38	10.16	0.432	1.001	1.108	24.488	3.3
FeK	94.62	89.84	0.999	1	0.993	294.351	26.2

Fig. 5.34 SEM and EDS of as-received metallic glass ribbon specimen.

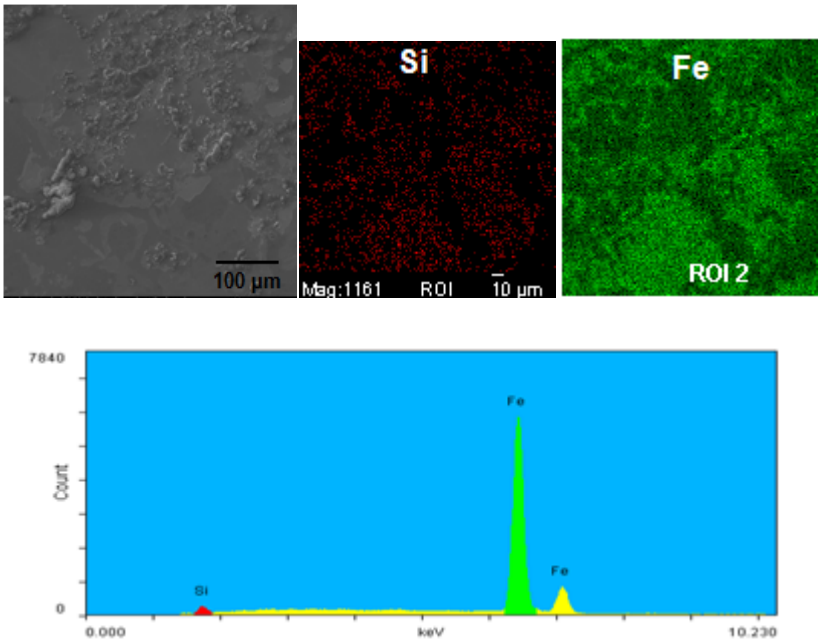

Elements:	WT%	AT%	K_A	K_F	K_Z	Intensity	P/bkg
SiK	1.47	2.88	0.421	1.001	1.113	8.53	1.9
FeK	98.53	97.12	1	1	0.998	402.48	25.5

Fig. 5.35 SEM and EDS of corrosion tested metallic glass ribbon specimen.

5.2.2 Phase Analysis:

Fig. 5.36 shows the XRD pattern of the as received ribbons and ribbons heat treated at 200 ^{o}C, 400 ^{o}C, before and after corrosion testing respectively. The amorphous broad halo is observed for the corrosion tested ribbon in the parameters mentioned in Chapter 5. Even the same amorphous broad halo is observed for heat treated ribbons at 200 ^{o}C, 400 ^{o}C respectively before and after corrosion testing.

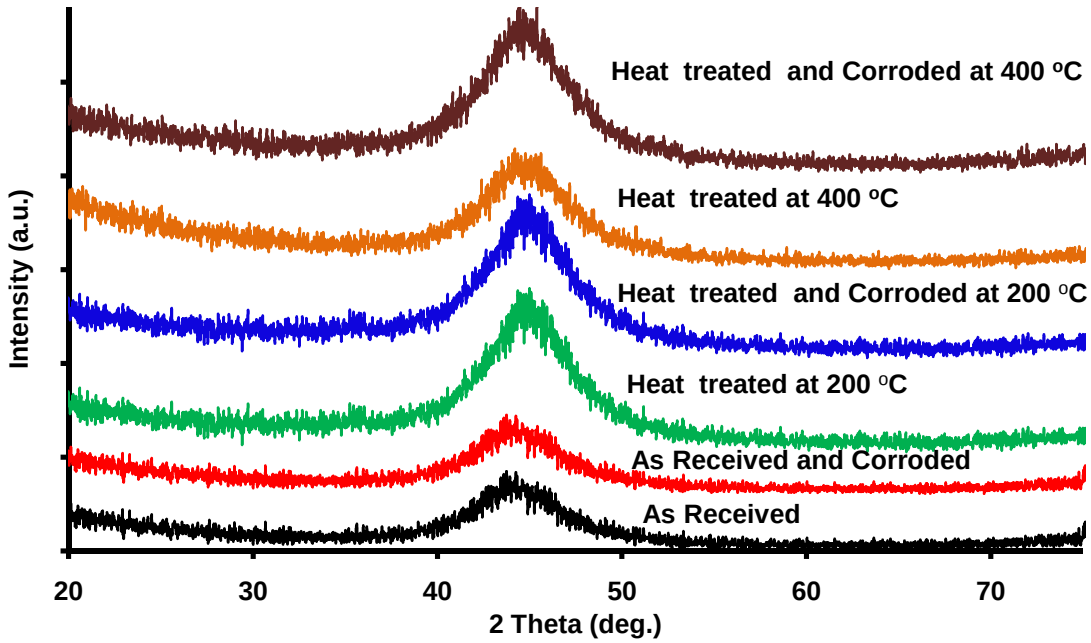

Fig. 5.36 XRD patterns of the heat treated and corrosion tested ribbon at the various temperatures.

Fig. 5.37 shows the XRD patterns for the ribbons heat treated at 600 ^{o}C and 800 ^{o}C before corrosion testing and after corrosion testing. For the ribbons heat treated at 600 ^{o}C sharp crystalline peaks of Fe_2B and Fe_3Si are observed from phase analysis software. Similar crystalline peaks with increased intensity were observed from the same ribbons which are heat treated at 600 ^{o}C and analyzed after corrosion testing. It shows that the crystallinity of the heat treated ribbons

increases after corrosion testing. For the ribbons heat treated at 800 ^{o}C similar crystalline peaks were observed. Even the crystallinity of the material increases after corrosion testing which is observed from the sharp peaks of increased intensity for corroded and heat treated ribbons at 800 ^{o}C.

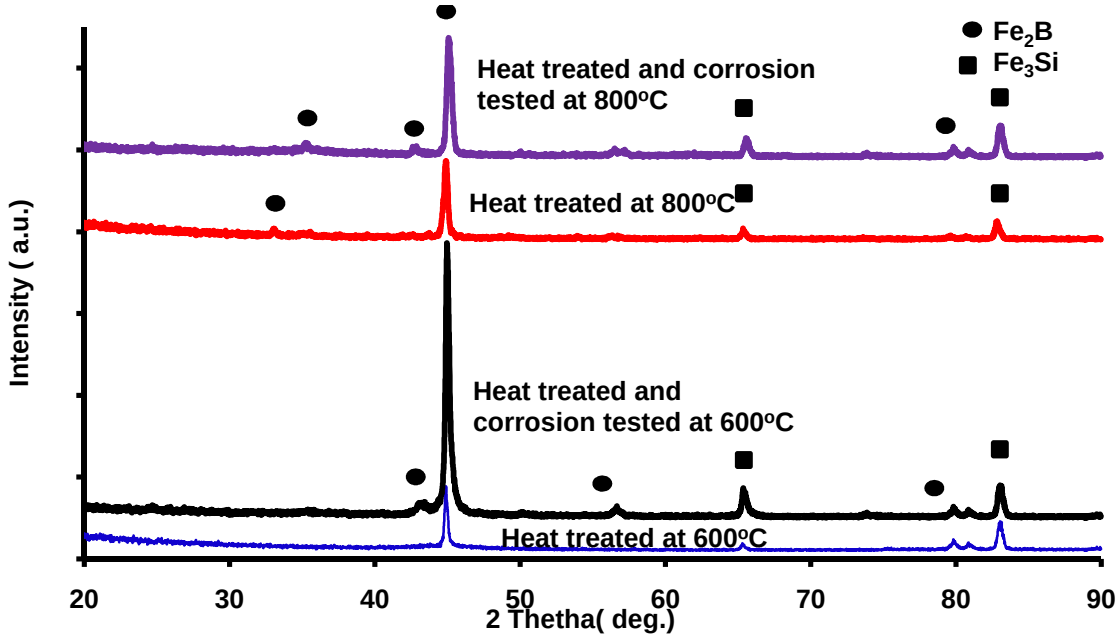

Fig. 5.37 XRD patterns of the heat treated and corrosion tested ribbon at the various temperatures.

5.2.3 Potentiodynamic Tafel plot for as received and heat treated Ribbons

Fig. 5.38 shows the Tafel plot of the as received amorphous alloy ribbon and amorphous alloy ribbon heat treated at different temperatures of 200 ^{o}C, 400 ^{o}C, 600 ^{o}C, and 800 ^{o}C respectively in 3.5% NaCl. Parameters such as corrosion potential, corrosion current and corrosion rate as observed from the Tafel plot are shown in Table 5.1. It was observed that the corrosion resistance of the samples increases as the annealing temperature increased. The obtained results also indicate that the increase in the annealing temperature shifts the corrosion

potential anodically. For the as received, heat treated at 200 ^{o}C and 400 ^{o}C ribbons the corrosion potential is lower and the ribbons tend to passivate before entering into active region. For the as received ribbons and ribbons heat treated at 200 ^{o}C and 400 ^{o}C similar passive regions in the potential range of -550 mV to -650 mV was observed. For the ribbons heat treated at 600 ^{o}C and 800 ^{o}C corrosion proceeds before entering into passive region. It directly proceeds into active region at higher corrosion potential. Thus, the corrosion rate of the heat treated ribbons at higher temperatures of 600 ^{o}C and 800 ^{o}C increases as it able to withstand higher corrosion potentials with lower current density. The increase in corrosion rate at increased annealed temperatures might be because of nanocrystallization and the structural relaxation [72] which is in correlation with the XRD and SEM results shown above.

Table 5.1: Variation in corrosion rate, corrosion current and corrosion potential for different heat treatment temperatures.

Material	**Corrosion potential(mV)**	**Corrosion Current (µA)**	**Corrosion rate(mm py)**
As received ribbon	**-775.77**	**-2.266**	**0.0207**
Ribbon heat treated at 200 ^{o}C	**-686.993**	**-92.627**	**0.0805**
Ribbon heat treated at 400 ^{o}C	**-744.45**	**-6.368**	**0.0581**
Ribbon heat treated at 600 ^{o}C	**-600.701**	**-4.007**	**0.0037**
Ribbon heat treated at 800 ^{o}C	**-556.797**	**-0.905**	**0.0008**

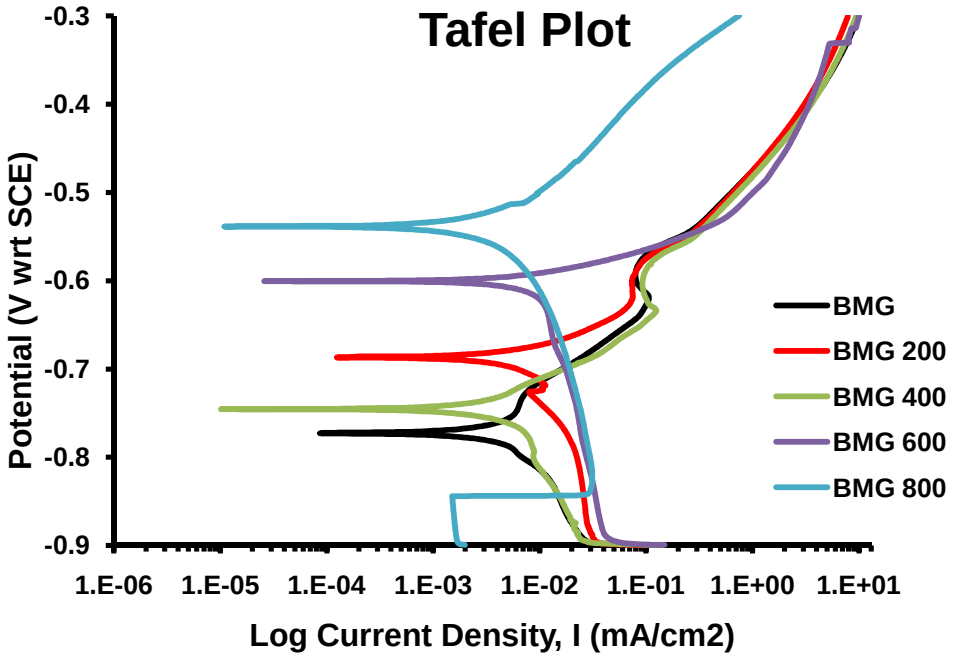

Fig. 5.38 Tafel plot during the corrosion test for Fe-B-Si alloy (BMG) ribbon for as received, heat treated at 200 ^{o}C, 400 ^{o}C, 600 ^{o}C, and 800 ^{o}C for 5 min.

5.3 Wear Testing on Fe-B-Si Metallic Glass Ribbons:

Fig. 5.39 shows the variation of the coefficient of friction with distance for the loads of 2 N, 4 N, 6 N, and 8 N respectively. Series of experiments are performed on the ribbons for durations of 2 min, 4 min, 6 min, 8 min, and 10 min with the loads of 2 N, 4 N, 6 N, and 8 N respectively and the variation of coefficient of friction is plotted in Fig. 5.39. In Fig. 5.39, at first the coefficient of friction remains constant as the load which is applied on the ribbon takes time to start applying the load on ribbon due to surface roughness and various factors. It was observed at the load of 2 N and 4 N all the ribbons tested showed similar behavior in coefficient of friction whereas for loads at 6 N and 8 N ribbons exhibited abnormal behavior due to the influence of substrate as these loads are too high for the these thin ribbons of 40 µm thickness.

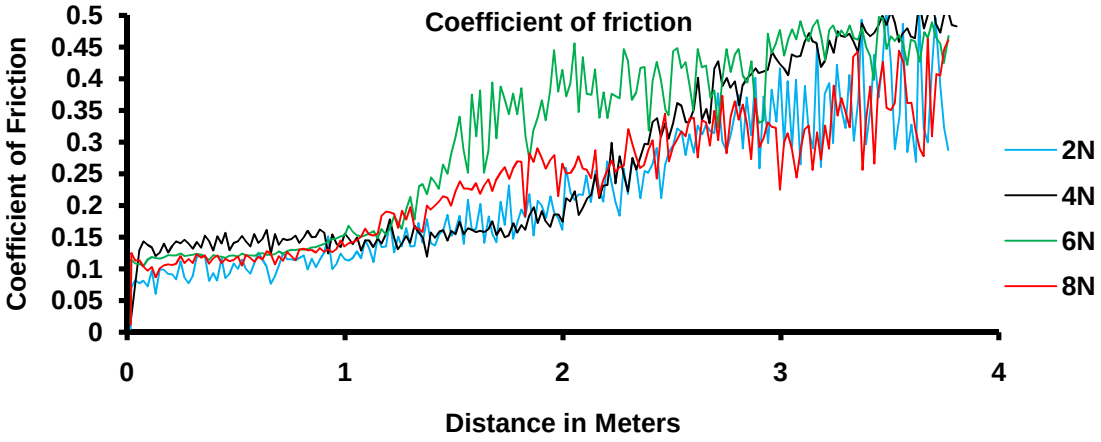

(a) 2 min of operation

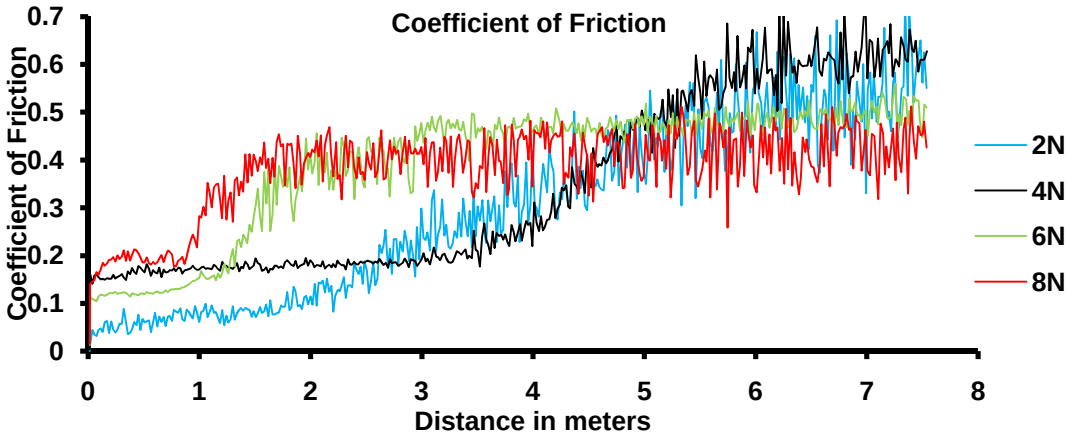

(b) 4 min of operation

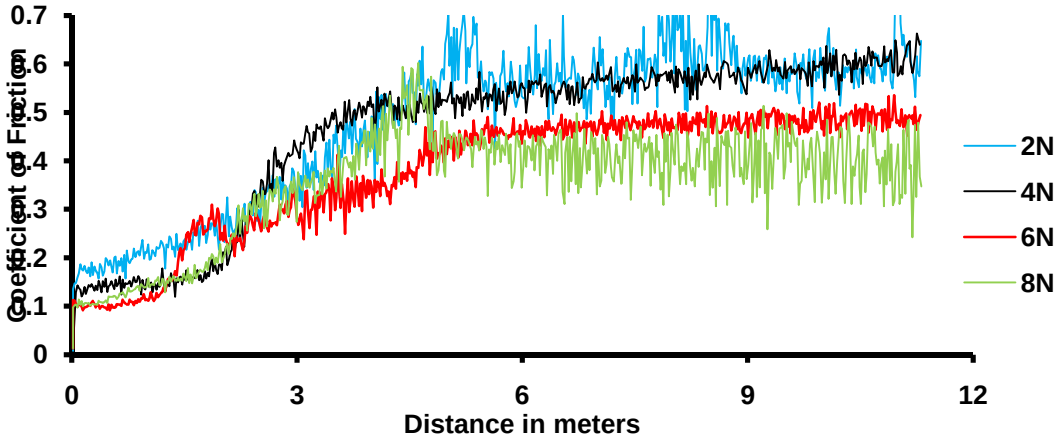

(c) 6 min of operation

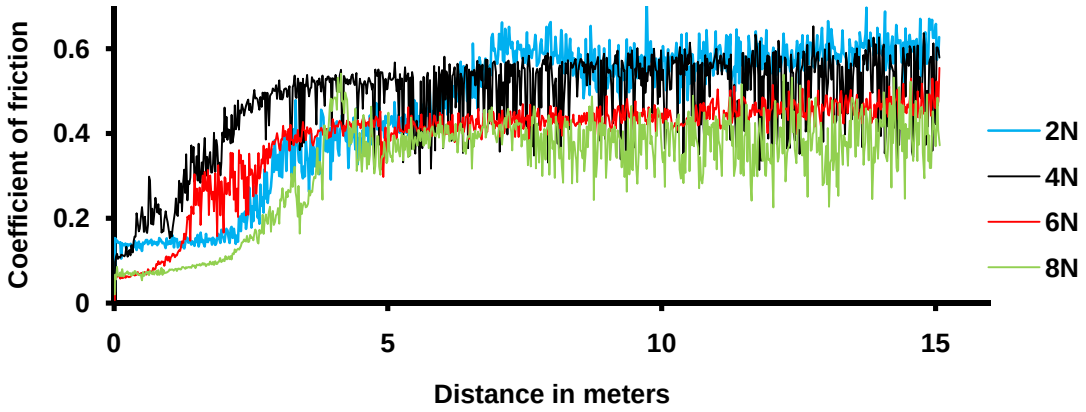

(d) 8 min of operation

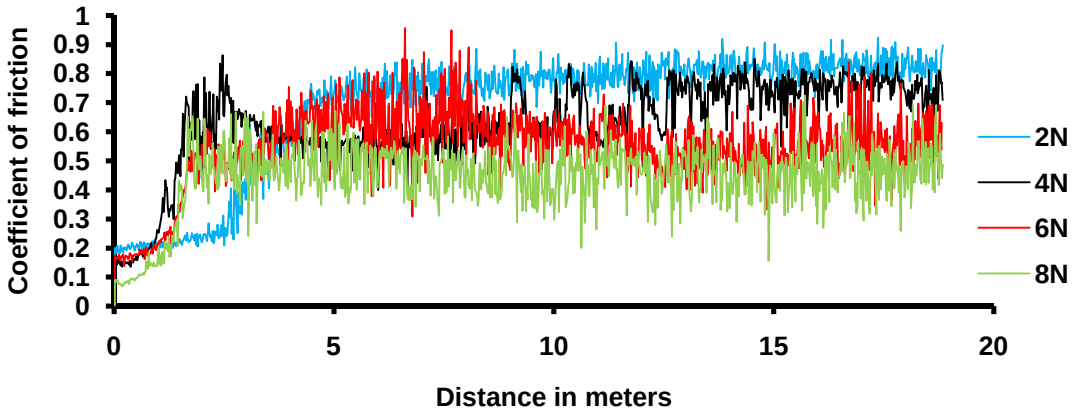

(e) 10 min of Operation

Fig. 5.39 Variation of coefficient of friction with distance at given respective loads.

Average coefficient of friction from these all these experiments were taken and plotted in the Fig. 5.40 showing the change in coefficient of friction for different minutes of operation at each loads of 2 N, 4 N, 6 N and 8 N. It was observed that the average coefficient of friction increase with increasing duration and it remains constant for 6 min and 8 min of operation. At 10 min of operation it again decreases due to influence of substrate.

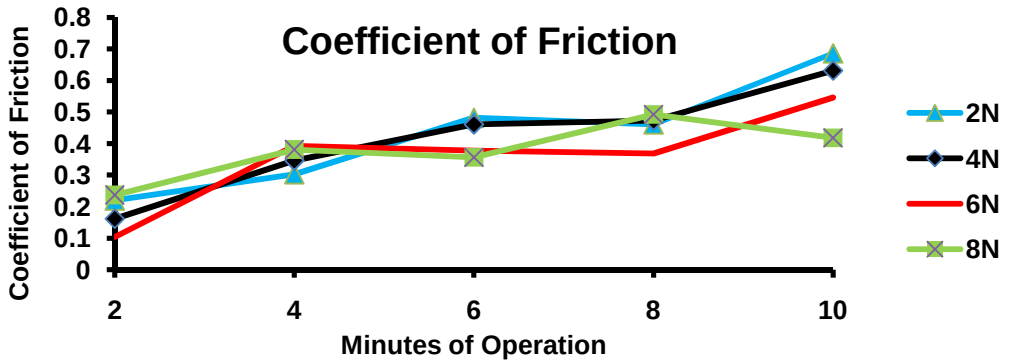

Fig. 5.40 Variation of average coefficient of friction with duration of operation at all the loads.

Fig 5.41 shows the variation in the surface roughness parameters R_a, R_z and R_{max} with minutes of operation for the loads of 2 N, 4 N, 6 N, 8 N and 10 N respectively. It was observed clearly that the R_a is lower at 2 N and 4 N loads at all the minutes of operation and at 6 N and 8 N loads, R_a is significantly higher than the previous loads. Variation in R_z and R_{max} showed the similar behavior of 2 N and 4 N load where the roughness is lower than the 6 N and 8 N load for all the minutes of operation.

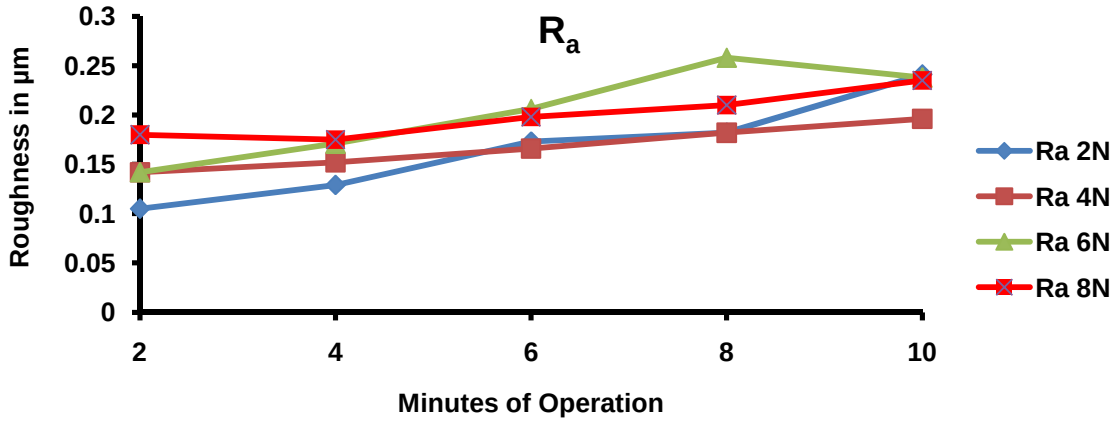

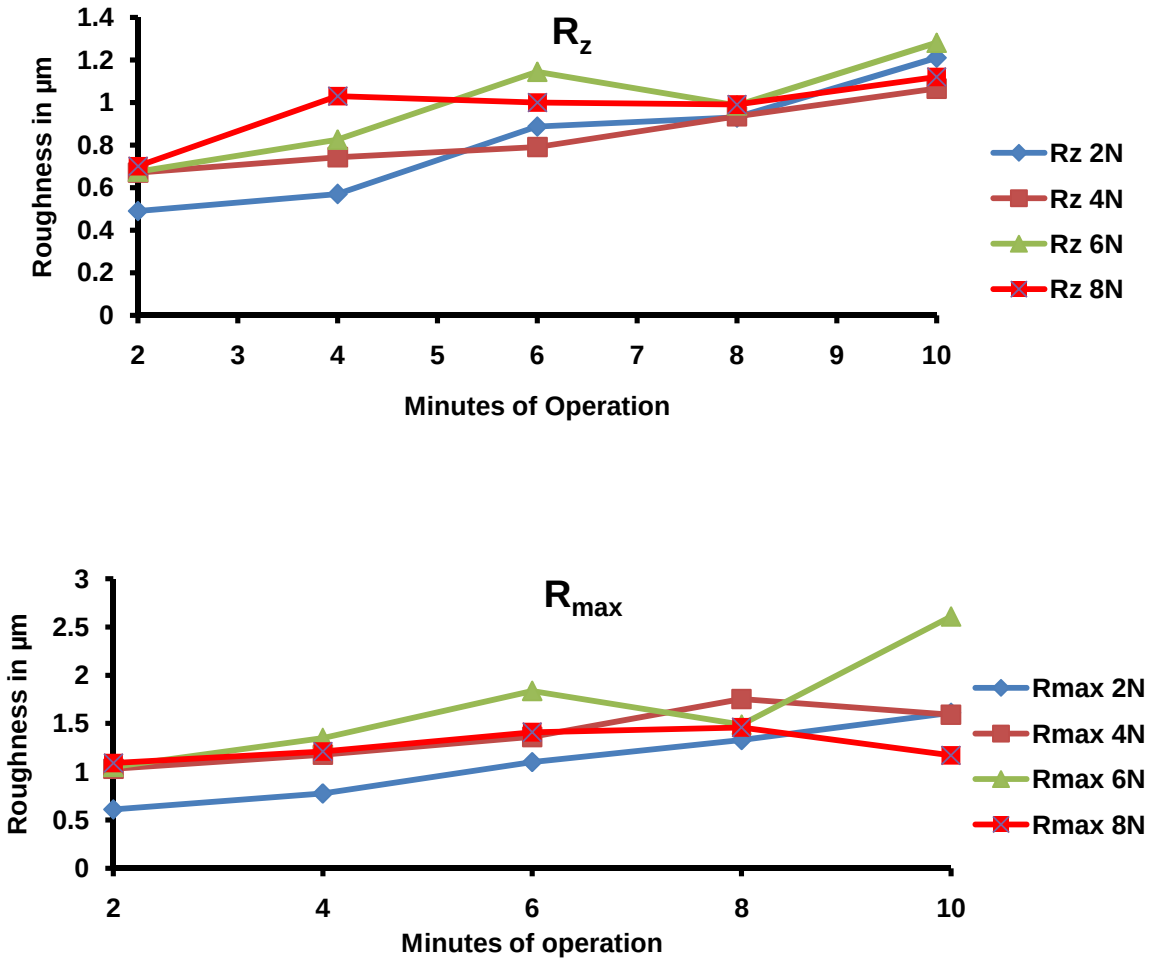

Fig. 5.41 Variation of R_a, R_z, and R_{max} with load and duration of operation at all the Loads during the test.

CHAPTER 6

CONCLUSIONS

- Excimer laser micromachining of the 40 µm thick $Fe_{85\text{-}95\%}Si_{5\text{-}10\%}B_{1\text{-}5\%}$ metallic glass ribbon caused crystallization at 300 mJ pulse energy, 5000 pulses and redeposition of the molten material was observed with the initiation of network structures.
- Excimer laser micromachining of the 3.86 mm thick $Fe_{48}Cr_{15}Mo_{14}Y_2C_{15}B_6$ bulk metallic glass caused crystallization at 400 mJ pulse energy, 2500 pulses and significant change in elemental composition was observed in the networks created on the craters and depletion Mo element was observed in the networks.
- Corrosion resistance of the $Fe_{85\text{-}95\%}Si_{5\text{-}10\%}B_{1\text{-}5\%}$ metallic glass ribbon increases with increase in the annealing temperature above the crystallization temperature due to nanocrystallization.
- Wear testing of the $Fe_{85\text{-}95\%}Si_{5\text{-}10\%}B_{1\text{-}5\%}$ metallic glass ribbon showed steadier low coefficient of friction in the range of μ=0.3-0.5 for the various minutes of operation due to lower surface roughness and higher micro hardness of ribbon at 2 N and 4 N of normal load

REFERENCES

1. W. Klement, R. H. Willens, P. Duwez. Non-crystalline structure in solidified gold-silicon alloys. *Nature*, 187 (4740), 869-870, 1960.
2. A. Peker, W. L. Johnson. A highly processable metallic-glass - $Zr_{41.2}Ti_{13.8}Cu_{12.5}Ni_{10.0}Be_{22.5}$. *Applied Physics Letters*, 63 (17), 2342-44, 1993.
3. A. Inoue, K. Ohtera, K. Kita, T. Masumoto. New amorphous Mg–Ce–Ni alloys with high-strength and good ductility. *Jpn. J. Appl. Phys. Part 2*, 27 (12), L2248–L2251, 1988.
4. A. Inoue, T. Zhang, T. Masumoto. Al–La–Ni amorphous-alloys with a wide supercooled liquid region. *Mater. Trans. JIM*, 30 (12), 965–972, 1989.
5. A. Inoue, T. Zhang, T. Masumoto. Zr–Al–Ni amorphous-alloys with high glass transition temperature and significant supercooled liquid region. *Mater. Trans. JIM*, 31 (3), 177–183, 1990.
6. L. Shen, H. Koshiba, T. Mizushima, A. Inoue. Bulk amorphous Fe–Ga–P–B–C alloys with a large supercooled liquid region. *Mater. Trans. JIM*, 41 (7), 873–876, 2000.
7. A. Inoue, Y. Shinohara, J. S. Gook. Thermal and magnetic properties of bulk fe based glassy alloys prepared by copper mold casting. *Mater. Trans. JIM*, 36(12), 1427–1433,1995.

8. A. Inoue, X. M. Wang, W. Zhang. Developments and applications of bulk metallic glasses. *Reviews on Advanced Materials Science*, 18 (1), 1-9, 2008.
9. M. Miller, P. K. Liaw. Bulk metallic glasses-overview. *Springer*, 2007.
10. M. Telford. The case for bulk metallic glass. *Materials Today*, 7, 36-43, 2004.
11. B. S. Murthy and S. Ranganathan, *Int.mater.rev.*, 43,1998
12. F. Spaepen, A microscopic mechanism for steady state in homogeneous flow in metallic glasses. *Acta Metall.*, 25, 407, 1977.
13. H. W. Jin, R. Ayer, J. Y. Koo, R. Raghavan, U. Ramamurty. Reciprocating wear mechanisms in a zr-based bulk metallic glass. *Journal of Materials Research*, 22 (2), 264-73, 2007.
14. C. A. Schuh, T. C. Hufnagel, U. Ramamurty. Overview No.144 - mechanical behavior of amorphous alloys. *Acta Materialia*, 55 (12), 4067-109, 2007.
15. A. Inoue. Stabilization of metallic supercooled liquid and bulk amorphous alloys. *Acta Materialia*, 48 (1), 279-306, 2000.
16. W. H. Wang, C. Dong, C. H. Shek. Bulk metallic glasses. *Materials Science and Engineering: R: Reports*, 44 (2-3), 45-89, 2004.
17. A. Einstein. Zur quantentheorie der strahlung physikalische gesellschaft zurich mitteilungen nr. 16(18) (1916) 47-62; an English translation appears in B. L. V Waerden, Ed., Sources of quantum mechanics. Amsterdam, 1967.
18. A. L. Schawlow, C. H. Townes. Infrared and optical masers, *Physical Review*, 112, 1940, 1958.
19. C. Winburn. What every engineer should know about lasers. *Marcel Dekker*, 1986.

20. T. H. Maiman. The laser odyssey, *Laser Press*, California, 2000.

21. http://www.worldoflasers.com/laserhistory.htm

22. P. W. Milonni, Joseph H. Eberly. Laser physics. *John Wiley and Sons* (2009), ISBN : 9780470387719

23. N.B. Dahotre, S.P. Harimkar. Laser fabrication and machining of materials. *Springer*, New York, 2007.

24. K. L. Choo. Micromachining using an excimer (248 nm) laser. Diss. Oklahoma State University, 2005. Dissertations & Theses @ Oklahoma State University - Stillwater, ProQuest. Web. 10 Nov. 2010.

25. G. Bellows, J. Kohls. Drilling without drills. *American Machinist*, 173-188, 1982.

26. G. Chryssolouris. Laser machining-theory and practice, *Mechanical Engineering Series Springer- Verlag*, 1991.

27. http://www.cmxr.com

28. W. M. Steen. Laser materials processing. *Springer*, London, 1991.

29. G. P. Zhang, Y. Liu, B. Zhang. Effect of annealing close to T_g on notch fracture toughness of Pd-based thin-film metallic glass for MEMS applications. *Scripta Materialia*, 54 (5), 897-901, 2006.

30. T. Fukushige, S. Hata, A. Shimokohbe. A MEMS conical spring actuator array. *Journal of Microelectromechanical Systems*, 14 (2), 243-53, 2005.

31. M. Bakkal, A. J. Shih, R. O. Scattergood. Chip formation, cutting forces, and tool wear in turning of Zr-based bulk metallic glass. *International Journal of Machine Tools & Manufacture*, 44 (9), 915-25, 2004.

32. M. Bakkal, C. T. Liu, T. R. Watkins, R. O. Scattergood, A. J. Shih. Oxidation and crystallization of Zr-based bulk metallic glass due to machining. *Intermetallics* 12 (2), 195-204, 2004.
33. M. Bakkal, A. J. Shih, R. O. Scattergood, C. T. Liu. Machining of a Zr-Ti-Al-Cu-Ni metallic glass. *Scripta Materialia*, 50 (5), 83-88, 2004.
34. M. Bakkal, A. J. Shih, S. B. McSpadden, C.T. Liu, R. O. Scattergood. Light emission, chip morphology, and burr formation in drilling the bulk metallic glass. *International Journal of Machine Tools & Manufacture*, 45 (7-8), 741-52, 2005.
35. M. Bakkal, A. J. Shih, S. B. McSpadden, R. O. Scattergood. Thrust force, torque, and tool wear in drilling the bulk metallic glass. *International Journal of Machine Tools & Manufacture*, 45 (7-8), 863-72, 2005.
36. M. Bakkal. Electron microscopy of bulk metallic glass machining chips. *Journal of Non-Crystalline Solids*, 355 (45-47), 2220-23, 2009.
37. R. Butje, Excimer laser based machining of amorphous metals, *Proceeding of SPIE-the international society for optical engineering*, 1023, 187, 1989.
38. M. Sorescu, E. T. Knobbe, Induced anisotropy and phase transformation in metallic glasses by pulsed excimer laser irradiation, *Physical review B*, 49(5), 3253-3265, 1994.
39. M. Sorescu, E. T. Knobbe, T. Barb, D. Sorescu, I. Bibicu. Comparison of electron-beam and pulsed-laser irradiation effects in $Fe_{80}B_{20}$. *Hyperfine Interactions*, 92 (1-4), 1347-53, 1994.

40. M. Sorescu, E. T. Knobbe, D. Barb. Excimer-laser processing of amorphous and nanocrystalline $Fe_{73.5}Cu_1Nb_3Si_{22.5-X}B_x$ (X=6 and 9). *Journal of Physics and Chemistry of Solids*, 56 (1), 79-87, 1995.
41. M. Sorescu, E. T. Knobbe, D. Barb. Evolution of phases and microstructure in $Fe_{81}B_{13.5}Si_{3.5}C_2$ metallic-glass during electron-beam and pulsed-laser irradiation. *Physical Review B*, 51 (2), 840-50, 1995.
42. A. Sypien, G. J. Kusiski, E. C. Nelson. TEM studies of the FeSiB amorphous alloy nanocrystallized by means of Nd:YAG-pulsed laser heating. *Materials Chemistry and Physics*, 81 (2-3), 390-92, 2003.
43. I. Quintana, T. Dobrev, A. Aranzabe, G. Lalev, S. Dimov. Investigation of amorphous and crystalline ni alloys response to machining with micro-second and pico-second lasers. *Applied Surface Science*, 255 (13-14), 6641-46, 2009.
44. D. Bauerle. Laser processing and chemistry. 3rd edn, *Springer*, Berlin. Heidelberg, 2000.
45. X. Liu, D. Du, G. Mourou. Laser ablation and micromachining with ultrashort laser pulses. *IEEE J. Quantum Electron.*, 33 (1706), 1716, 1997.
46. H. Dachraoui, W. Husinsky, G. Betz. Ultra-short laser ablation of metals and semiconductors: evidence of ultra-fast coulomb explosion. *Applied Physics A: Materials Science & Processing*, 83 (2), 333-36, 2006.
47. P. T. Mannion, J. Magee, E. Coyne, G. M. O'Connor, T. J. Glynn. The effect of damage accumulation behavior on ablation thresholds and damage morphology in ultrafast laser micro-machining of common metals in air. *Applied Surface Science*,233 (1-4), 275-87, 2004.

48. M. Lenzner, J. Krüger, S. Sartania, Z. Cheng, Ch. Spielmann, G. Mourou, W. Kautek, F. Krausz. Femtosecond optical breakdown in dielectrics. *Physical Review Letters*, 80 (18), 4076, 1998.
49. X. L. Wang, P. Lu, N. D. Y. Li, C. Liao, Y. Chang, G. Yang, Q. Zheng. Morphology and oxidation of Zr-based amorphous alloy ablated by femtosecond laser pulses. *Applied Physics a-Materials Science & Processing*, 89 (2), 547-52, 2007.
50. X. L. Wang, P. Lu, N. Dai, Y. Li, C. Liao, Q. Zheng, L. Liu. noncrystalline micromachining of amorphous alloys using femtosecond laser pulses. *Materials Letters*, 61 (21), 4290-93, 2007.
51. H. Wang, C. Liang, X. Chen, L. Wang, Y. Yang, J. Yang, S. Zhu, C. Li. Effects of femtosecond laser ablation on the surface morphology and microstructure of a bulk TiCuPdZr glass alloy. *Rare Metals*, 28 (3), 272-76, 2009.
52. W. Jia, Z. Peng, Z. Wang, X. Ni, C. Wang. The effect of femtosecond laser micromachining on the surface characteristics and subsurface microstructure of amorphous FeCuNbSiB alloy. *Applied Surface Science*, 253 (3), 1299-303, 2006.
53. W. Jia, D. Zhang, X. Li, L. Chai, Z. Zang, C. Wang. Heat effects of amorphous fecunbsib alloy ablated with femtosecond laser. *Thin Solid Films*, 516 (8), 2260-63, 2008.
54. K. Asami, K. Hashimoto, T. Masumoto, S. Shimodaira. Esca study of the passive film on an extremely corrosion-resistant amorphous iron alloy. *Corrosion Science*, 16 (12), 909-14, 1976.

55. K. Asami, K. Hashimoto, S. Shimodaira. An xps study of the passivity of a series of iron--chromium alloys in sulphuric acid. *Corrosion Science*, 18 (2): 151-60, 1978.
56. K. Hashimoto, T. Masumoto. Extremely high corrosion resistance of chromium-containing amorphous iron alloys. *Materials Science and Engineering*, 23 (2-3), 285-88.
57. K. Hashimoto, K. Osada, T. Masumoto, S. Shimodaira. Characteristics of passivity of extremely corrosion-resistant amorphous iron alloys. *Corrosion Science*, 16 (2), 71-76, 1976.
58. M. Naka, K. Hashimoto, T. Masumoto. Effect of metalloidal elements on corrosion resistance of amorphous iron-chromium alloys. *Journal of Non-Crystalline Solids*, 28 (3), 403-13, 1978.
59. C. M. Hanham, Y. Waseda, K. T. Aust. Corrosion behaviour of amorphous iron-base alloys. *Materials Science and Engineering*, 45 (1), 71-76, 1980.
60. G. Rife, P. C. Chan, K. T. Aust, Y. Waseda. Corrosion of iron-, nickel- and cobalt-base metallic glasses containing boron and silicon metalloids. *Materials Science and Engineering*, 48 (1), 73-79, 1981.
61. M. Magrini, P. Matteazzi, A. Frignani. Structural characterization and electrochemical behaviour of Fe-Ni-Mo-B amorphous alloys. *Materials Chemistry and Physics*, 13 (1), 71-83, 1985.
62. I. Chattoraj, A. K. Bhattamishra, A. Mitra. The effect of corrosion on the magnetic properties of rapidly solidified Fe-Si-B amorphous fibres. *Scripta Metallurgica et Materialia*, 26 (7), 1013-17, 1992.

63. I. Chattoraj, A. K. Bhattamishra, A. Mitra. The effect of near-crystallization temperature annealing on the electrochemical behavior of amorphous $Fe_{77.5}B_{15}Si_{7.5}$ fibres in borate buffer. *Scripta Metallurgica et Materialia*, 29 (5) , 611-16, 1993.
64. I. Chattoraj, A.K. Bhattamishra, A. Mitra. Polarization and resistivity measurements of post-crystallization changes in amorphous Fe-B-Si alloys. *Corrosion*, 49 (9), 707-13, 1993.
65. M. G. Alvarez, S. M. Vazquez, J. Moya, H. Sirkin. Anodic behaviour of $Fe_{73.5}Si_{13.5-X}Al_xB_9Nb_3Cu_1$ (X = 0-2) amorphous, nanostructured and crystalline alloys. *Scripta Materialia*, 44 (3), 507-12, 2001.
66. Y. Yoshizawa, S. Oguma, K. Yamauchi. New Fe-based soft magnetic-alloys composed of ultrafine grain-structure. *Journal of Applied Physics*, 64 (10), 6044-46, 1988.
67. V. Cremaschi, I. Avram, T. Pérez and H. Sirkin. Electrochemical studies of amorphous, nanocrystalline, and crystalline FeSiB based alloys. *Scripta Materialia*, 46 (1), 95-100, 2002.
68. F. F. Marzo, A. Altube, A. R. Pierna. A comparative study, by eis and tafel experiments, of the electrochemical behavior of FINEMET alloys modified with chromium. *Electrochimica Acta*, 47 (13-14), 2265-69, 2002.
69. A. Altube, A. R. Pierna. Thermal and electrochemical properties of cobalt containing FINEMET type alloys. *Electrochimica Acta*, 49 (2), 303-11, 2004.
70. F. F. Marzo, A. R. Pierna, J. Barranco, G. Vara, A. Perez, T. Gómez-Acebo. Optimization of the microstructure and corrosion resistance of FINEMET type

alloys in koh solutions. *Journal of Non-Crystalline Solids*, 353 (8-10), 875-78, 2007.

71. G. Vara, A.R. Pierna, J.A. García, J.A. Jimenez and M. Delama. Influence of nickel content on the electrochemical behavior of FINEMET type amorphous and nanocrystalline alloys." *Journal of Non-Crystalline Solids* 353 8-10 (2007): 1008-10.
72. H. A. Shivaee, A. N. Golikand, H. R. M. Hosseini, M. Asgari. Influence of annealing on the electrochemical behavior of FINEMET amorphous and nanocrystalline alloy. *Journal of Materials Science*, 45 (2), 546-51, 2010.
73. R. Klinger, H. G. Feller. Sliding friction and wear-resistance of the metallic-glass $Fe_{40}Ni_{40}B_{20}$. *Wear*, 86 (2), 287-97, 1983.
74. D. H. Lee, J. E. Evetts. Sliding friction and structural relaxation of metallic glasses. *Acta Metallurgica*, 32 (7), 1035-43, 1984.
75. Y. Nishi, T. Kai, K. Kitago. Wear-resistance of Fe-Co-Si-B alloy glasses. *Wear*, 126 (2), 191-96, 1988.
76. Kishore, U. Sudarsan, N. Chandran, K. Chattopadhyay. On the wear mechanism of iron and nickel based transition-metal metalloid metallic glasses. *Acta Metallurgica*, 35 (7), 1463-73, 1987.
77. N. I. Noskova, L. G. Korshunov, A. P. Potapov. Nanocrystallization of amorphous alloys induced by thermal force impact in different media, in *Collected Scientific Papers "Structure and Properties of Nanocrystalline Materials"* (Ural. Otd. Ross. Akad. Nauk, Ekaterinburg, 1999) [in Russian].

78. B. Prakash, K. Hiratsuka. Sliding wear behaviour of some Fe-, Co- and Ni-based metallic glasses during rubbing against bearing steel. *Tribology Letters*, 8 (2-3), 153-60, 2000.

79. B. Prakash. Abrasive wear behaviour of Fe, Co and Ni based metallic glasses. *Wear*, 258 (1-4), 217-24, 2005.

80. L. G. Korshunov, N. L. Chernenko. Structural transformations and wear resistance of abrasive-affected amorphous Fe- and Co-based alloys. *Physics of Metals and Metallography*, 106 (6), 616-23, 2008.

81. L. G. Korshunov, N. L. Chernenko, Y. N. Goikhenberg. Structural transformations and tribological properties of amorphous alloys upon wear at room and cryogenic temperatures. *Physics of Metals and Metallography*, 108 (3), 310-20, 2009.

82. L. G. Korshunov, V. A. Shabashov, A. V. Litvinov, N. L. Chernenko. Structural transformations of amorphous iron-based alloys upon abrasive and thermal treatments. *Physics of Metals and Metallography*, 109 (5), 514-23, 2010.

83. K. L. Choo, Y. Ogawa, G. Kanbargi, V. Otra, L. M. Raff, R. Komanduri. Micromachining of silicon by short-pulse laser ablation in air and under water. *Materials Science and Engineering a-Structural Materials Properties Microstructure and Processing*, 372 (1-2), 145-62, 2004.

84. http://www.metglas.com/downloads/msds/msds2605sa1.pdf

85. Lambda physik user manual for compex laser series.

86. The UNIDEX 500 motion controller and windows software operation & technical manual, version 1.2, Aerotech, Inc.

87. MicroLAS beam delivery system for alignment of optics.

88. The ATS 100 series position stages instruction manual, version 1.0, Aerotech Inc.

89. T. M. Yue, Y. P. Su, H. O. Yang. Laser cladding of $Zr_{65}Al_{7.5}Ni_{10}Cu_{17.5}$ amorphous alloy on magnesium. *Materials Letters*, 61 (1), 209-12, 2007.

90. A. Basu, A. N. Samant, S. Harimkar, J. D. Majumdar, I. Manna, N. B. Dahotre. Laser surface coating of Fe-Cr-Mo-Y-B-C bulk metallic glass composition on Aisi 4140 steel. *Surface & Coatings Technology*, 202 (12), 2623-31, 2008.

91. T. T. Wong, G. Y. Liang. Formation and crystallization of amorphous structure in the laser-cladding plasma-sprayed coating of Al-Si alloy. *Materials Characterization*, 38 (2), 85-89, 1997.

92. A. Zaluska, H. Matyja, Crystallization characteristics of amorphous Fe-Si-B alloys, *J. Mater. Sci.*, 18 , 2163, 1983.

93. H. M. Ha, J. H. Payer. Devitrification of Fe-based amorphous metal sam 1651: a structural and compositional study. *Metallurgical and Materials Transactions a-Physical Metallurgy and Materials Science* 40A, 11, 2519-29, 2009.

APPPENDICES

STANDARD OPERATING GUIDELINES

1. Preliminary Instructions for the user

(a) Only authorized personnel may operate the laser.

(b) Wear safety goggles when attempting to power-up the laser.

(c) Remove bracelets, rings, watch, or other reflective jewelry.

(d) The curtain must be closed in the room while the laser fires.

(e) Ensure the installation has been completed.

(f) Ensure a leak test has been performed.

(g) Check the beam path.

(h) Close all gas cylinder valves.

(i) Close all pressure regulators in the gas lines.

(j) Open gas cylinder valves

(k) Set pressure regulators to max. 4 bar (abs.).

(l) Observe the maintenance schedule.

2. Warm-up Period

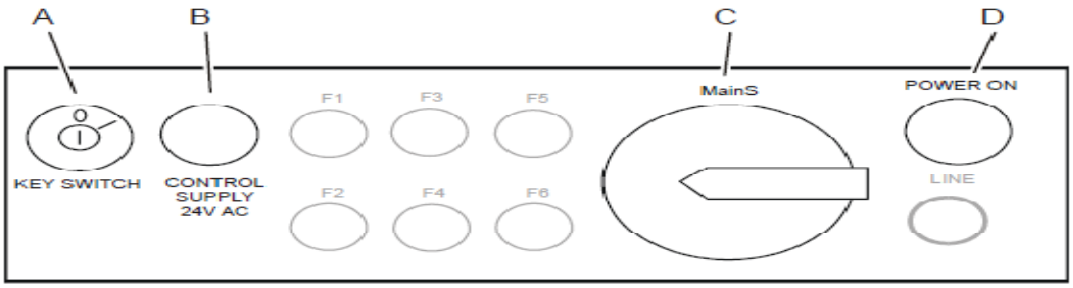

(a) Verify cooling water is flowing.

(b) Turn on the key switch “0” to “I to the laser. Only authorized users will have access to the key.

(c) Turn on MAINS power switch.

(d) Wait 8 minutes for the thyratron to warm up before attempting to fire the laser.

(e) The control supply lamp and the power on lamp (B and D) are now illuminated.

(f) Check settings on laser control panel for appropriateness.

The warm-up period can be used to perform maintenance actions:

– check parameter settings

– flush the lines

– perform a new gas fill

After warm-up, the laser is ready for laser operation

3. Check Current settings for the Gas pressure

(a) Push SEL and then push ENTER.

(b) In case need to change the value, type in the new value.

(c) Push ENTER to quit

If there is no need to change the above value, this step can be skipped over.

3. Evacuate Filling Line of Gases

(a) The two person should be present.

(b) Keep main valve of the gas cylinder closed.

(c) Set the pressure regulator to maximal pressure (turn clock wise).

(c) Execute the FLUSH LINE procedure to refresh (flushing) the gas in the fill lines.

(d) Repeat this procedure for the all connected gases at least 2 times.

4. Set filling line to Pressure required for operation

(a) Set pressure regulator to minimal pressure (Turn Counter Clockwise)

(b) Open main valve of the gas cylinder

(c) Close main valve of the Gas cylinder

(d) Set pressure regulator on gases according to our requirement.

5. Make a New Fill

(a) Before fill the new gas, the pressure on the control panel should be pumped down to 30 mbar.

(b) Executing NEW FILL will pump the laser tube to 30 mbar. If it cannot pump down to 30 mbar it means there may be some leaks in the somewhere. We can check the connector of Vacuum pump on the back panel of the Laser. After the pressure is down to 30 mbar, the vacuum pump stop working. Then continue the filling process. The filling sequence is Halogen, rare, buffer then inert gas.

Notice:

If one of the gas tap is closed, the pressure will not go up. Be sure that all the gases are not run out and the tap is opened. This procedure will take 10-15 minutes.

8. Control operating parameters

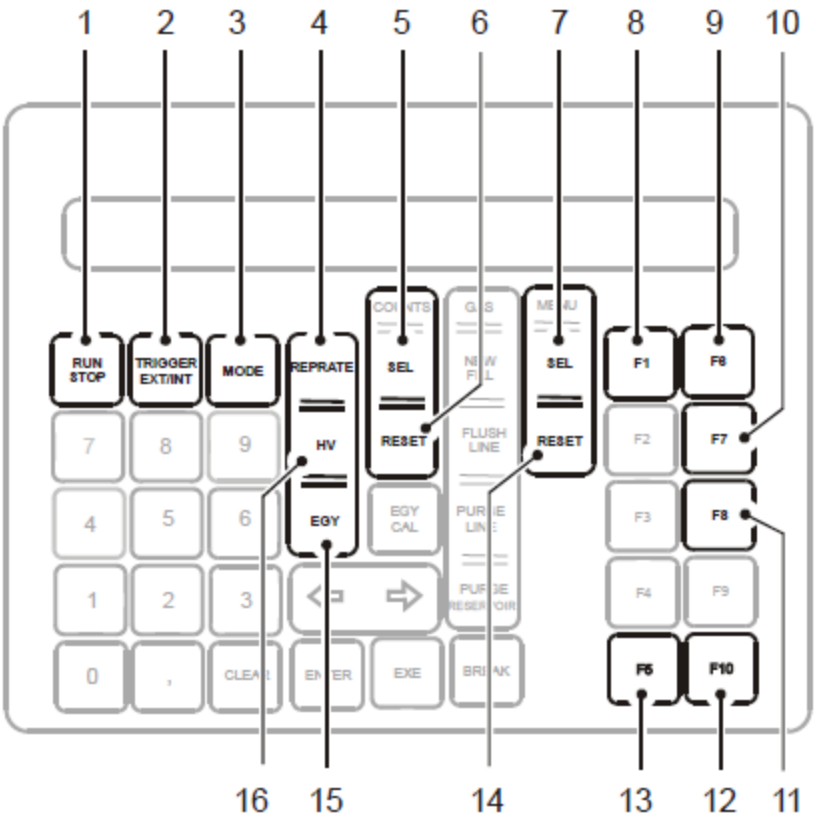

Overview of the handheld keypad

1 Start / stop laser operation

2 Trigger mode

3 Running mode

4 Repetition rate

5 Select counter

6 Reset user counter

7 Select gas menu

8 Help

9 Emergency Fill (manual fill with inert gas)

10 Gas Mode

11 Charge on demand

12 Temperature control

13 Reset gas menu

14 Set beam energy

15 Set HV constant

NOTE

A) The function keys <F2> and <F9> are for service only and therefore protected with a password.

B) To abort software related procedures without saving changes, press <BREAK>.

7. Check Parameter Settings

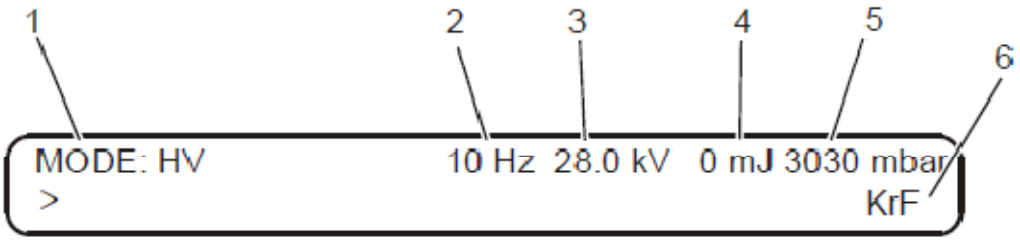

1 Running mode

2 Repetition rate

3 Charging Voltage

4 (if HV const. is selected) actual value measured by the Energy Monitor

- (otherwise) preset EGY const. value

5 Laser tube pressure --

6 Excimer gas (gas menu)

8. Firing the Laser

(a) Ensure the shutter is closed and the beam path is clear of obstructions. Check that the laser shielding is in place.

(b) Check the pulse frequency and high voltage settings.

(c) Open the shutter.

(d) Start the laser. If the laser does not start, check for INTERLOCK/REMOTE message, which indicates if the curtain or door is not closed properly.

7. Emergency Shutdown

(a) Turn off the MAINS switch or

(b) Turn off the key switch

8. Standard Shutdown

(a) Stop the laser.

(b) Close the shutter.

(c) Turn off the MAINS switch

(d) Turn off the key switch and return key to storage box.

(e) Check that gas tank valves are closed.

9. Cleaning and Aligning Optics

(a) With laser power off, open shutter and inspect optics.

(b) Remove and clean optics as specified by Lambda Physik instructions.

(c) Re-align optics following Lambda Physik instructions

10. Replacing the Halogen Filter

(a) Store new filters unopened in their original bag.

(b) Wear protective glasses and gloves.

11. Additional Information

The COMPex 205 operates at 248 nm (UV), 600 mJ/pulse, 10 Hz. The beam will be completely enclosed by acrylic shielding or an opaque curtain, each designed for use with 248 nm excimer laser radiation. The beam height will be approximately 8 feet off the door. The beam is steered vertically down to the chamber and then steered diagonally in through a laser window. Shielding or the chamber itself will block the main beam and all diffuse reflections.

VITA

Vamsi Karthik Kommineni

Candidate for the Degree of

Master of Science

Thesis: EFFECTS OF EXCIMER LASER ON THE SURFACE MORPHOLOGY AND MICROSTRUCTURE OF IRON-BASED METALLIC GLASSES, AND EVALUATION OF ITS TRIBOLOGICAL AND CORROSION PROPERTIES

Major Field: Mechanical and Aerospace Engineering

Biographical:

Personal Data: Born in Tirupati, AP on November 24, 1988

Education:

Received the Master of Science degree from Oklahoma State University, Stillwater, OK, USA, 2010 in Mechanical and Aerospace Engineering.

Received the B.Tech degree from Jawaharlal Nehru Technological University, Anantapur, AP, India, 2008 in Mechanical Engineering.

Experience:

Graduate Research Assistant in the School of Mechanical and Aerospace Engineering, Oklahoma State University, Stillwater, Oklahoma, Jan2009-Present and 6 months of experience as Engineering Intern in Satish Dhawan Space Center, Sriharikota, India

Professional Memberships: TMS, AIST, ASM, ACerS.

Name: Vamsi Karthik Kommineni Date of Degree: May, 2011

Institution: Oklahoma State University Location: Stillwater, Oklahoma

Title of Study: EFFECTS OF EXCIMER LASER ON THE SURFACE MORPHOLOGY AND MICROSTRUCTURE OF IRON-BASED METALLIC GLASSES, AND EVALUATION OF ITS TRIBOLOGICAL AND CORROSION PROPERTIES

Pages in Study: 108 Candidate for the Degree of Master of Science

Major Field: Mechanical and Aerospace Engineering

Scope and Method of Study:
Metallic Glasses are the new class of engineering materials having superior mechanical, tribological and corrosion properties when compared to conventional metals and alloys due to their disordered atomic structure. Fe-based metallic glasses belonging to this group of materials has potential applications in various industries due to its favorable properties. But, fabrication of these metallic glasses into micro, nano-scale components, and very fine intricate shapes with high dimensional accuracy cannot performed by traditional machining (lathe turning or drilling) methods. This motivated researchers to look for an alternative technique to process these materials with high dimensional accuracy. Excimer laser micromachining is a potential non-traditional machining technique where pulse length of 25 ns is used for micromachine material without any burrs, spatter etc. In this study, effect of excimer laser on the surface morphology and microstructure of these iron based metallic glasses was studied and evaluation of the corrosion resistance of the iron based metallic glass ribbon with heat treatment temperatures, wear behavior of the ribbon was conducted.

Findings and Conclusions:
Excimer laser induced craters were investigated by optical and scanning electron microscope (SEM) and laser interference microscope (MicroXam). The effects of pulse energy and number of pulses were studied in order to analyze the minimum pulse parameters required for the initiation of craters on the material surface. Morphological differences were observed in the crater surface compared with the surrounding area. Even change in the phase of material from amorphous structure to the crystalline structure was observed in these craters. The significance of this investigation is that ablation process in the excimer laser is not limited to direct solid-vapor transition, but also involves the substrate heating and change in microstructure due to thermal properties of the material. Increase in the corrosion resistance of the metallic glass ribbon was observed with the annealing temperature due to structural relaxation and variation of coefficient of friction in the range of 0.3-0.5 was observed for metallic glass ribbon during wear testing.

ADVISER'S APPROVAL: Dr. Sandip P. Harimkar